Chem Soc Rev

REVIEW ARTICLE

View Article Online
View Journal | View Issue

Cite this: *Chem. Soc. Rev.*, 2024, **53**, 8240

Nature-inspired adhesive systems

Ming Li †*[a] Anran Mao †[b] Qingwen Guan [c] and Eduardo Saiz *[a]

Many organisms in nature thrive in intricate habitats through their unique bio-adhesive surfaces, facilitating tasks such as capturing prey and reproduction. It's important to note that the remarkable adhesion properties found in these natural biological surfaces primarily arise from their distinct micro- and nanostructures and/or chemical compositions. To create artificial surfaces with superior adhesion capabilities, researchers delve deeper into the underlying mechanisms of these captivating adhesion phenomena to draw inspiration. This article provides a systematic overview of various biological surfaces with different adhesion mechanisms, focusing on surface micro- and nanostructures and/or chemistry, offering design principles for their artificial counterparts. Here, the basic interactions and adhesion models of natural biological surfaces are introduced first. This will be followed by an exploration of research advancements in natural and artificial adhesive surfaces including both dry adhesive surfaces and wet/underwater adhesive surfaces, along with relevant adhesion characterization techniques. Special attention is paid to stimulus-responsive smart artificial adhesive surfaces with tunable adhesive properties. The goal is to spotlight recent advancements, identify common themes, and explore fundamental distinctions to pinpoint the present challenges and prospects in this field.

Received 9th April 2024

DOI: 10.1039/d3cs00764b

rsc.li/chem-soc-rev

1. Introduction

Drawing inspiration from nature remains an ongoing practice in materials engineering.[1–6] Over billions of years of evolution and natural selection, organisms have evolved distinctive strategies to optimize their structures and functionalities. By leveraging surfaces spanning multiple length scales, ranging from micro to nano levels, and coupled with intricate chemical

[a] *Centre of Advanced Structural Ceramics, Department of Materials, Imperial College London, London, SW7 2AZ, UK. E-mail: m.li19@imperial.ac.uk, e.saiz@imperial.ac.uk*
[b] *Department of Fibre and Polymer Technology, KTH Royal Institute of Technology, Teknikringen 56, 100 44 Stockholm, Sweden*
[c] *School of Chemistry, University of Glasgow, Glasgow, G12 8QQ, UK*
† The two authors contribute equally to this work.

Ming Li

Ming Li was a member of the President Scholar Group (2019-2023) during pursuing his PhD degree in Department of Materials, Imperial College London, the UK, where he was supervised by Prof. Eduardo Saiz and Dr Florian Bouville. His research covers multiple areas related to materials chemistry, including the synthesis of biomimetic smart soft matter (supramolecular polymers and gels as well as self-assembled polymer nanostructures), and biomimetic smart interfaces (interfaces with multifunctional responses exhibiting special wetting and adhesion) that are applicable in many key technologies from energy generation to environmental clean-up.

Anran Mao

Anran Mao received her PhD degree in Chemical Engineering from Zhejiang University in 2022 under the supervision of Prof. Hao Bai. From 2021 to 2022, she was a visiting PhD student in Prof. Eduardo Saiz's group at Imperial College London, where she worked on 3D printing of bioinspired ceramics. Currently, she is a postdoctoral researcher at KTH Royal Institute of Technology, Sweden. Her research interests including understanding the relationships between mechanical properties and multi-scale structures of biological materials, as well as fabricating of bioinspired materials for applications such as lightweight and strong materials, drug delivery.

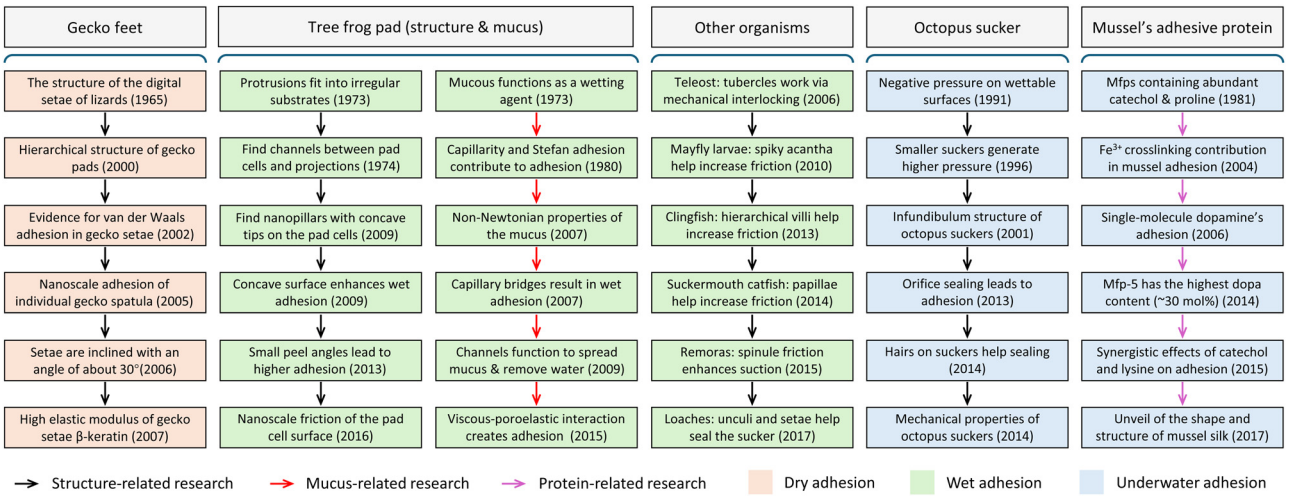

Fig. 1 Research progress of adhesion mechanisms of different creatures. Typical examples including dry adhesion (geckos), wet adhesion (tree frogs, other creatures), and underwater adhesion (octopus and mussels). Adapted with permission from ref. 6 Copyright 2020, Wiley-VCH.

compositions, various natural entities demonstrate intriguing adhesive properties tailored to specific environments.[4,6–13]

In-depth exploration of bio-adhesion phenomena holds the potential to expedite the advancement of artificial surfaces endowed with desirable adhesive capabilities (Fig. 1).[6] From the perspective of surface structure, geckos exhibit remarkable climbing abilities on rough vertical walls and even inverted ceilings, owing to the hierarchical distribution of setae structures on the soles of their feet.[14–16] Similarly, tree frogs navigate irregular surfaces, like wet leaves or tree trunks, by employing polygonal epithelial cells on their toe pads, aided by channels between cells to spread secreted mucus and enhance surface grip.[17,18] Additionally, octopuses utilize suction cups on their arms for marine locomotion and prey capture, featuring a dense array of hair structures that ensure suction cup sealing and create reliable pressure differentials.[19–21] Mayfly larvae, on the other hand, cling to pebbles in rapids due to the robust friction between their bristly gill plates and rough surfaces.[22] These distinctive functionalities stem from a variety of interfacial interactions between soft and intricate micro- and nanostructures evolved within organisms and their contact substrates, including friction,[23–25] van der Waals force,[26] capillary force,[27,28] and vacuum suction force.[8,29] From the perspective of chemical components, mussels possess the ability to create robust adhesive plaques through the secretion of adhesive proteins, effectively bonding to irregular surfaces in seawater.[30,31] The strong adhesion observed at the interface between the plaque and substrate primarily arises from six key mussel foot proteins (mfps), denoted as mfp-1 to mfp-6.[32–34] These proteins all contain significant amounts of components effective for adhesion, such as dopa, phenylalanine, tyrosine, and charged groups, although the proportions of each component vary. Notably, mfp-5 stands

Qingwen Guan

Qingwen Guan received her master degree from China University of Petroleum (Beijing) in 2019. Currently, she is pursuing her PhD degree under the supervision of Professor Dave Adams in the University of Glasgow, with the supporting from China Scholarship Council. Her research focus on soft matters, including low molecular weight gelator capable of self-assembling and their interfacial properties, as well as modulating interfacial interactions to alter the assembly behavior, mechanical properties, and phase transitions of multicomponent systems. She also delved into the internal mechanisms involved in developing controllable, reproducible, and versatile gel preparation methods.

Eduardo Saiz

Eduardo Saiz received his MsC from the Universidad de Cantabria (Spain) and his PhD from the Universidad Autonoma de Madrid in 1992. His PhD project was carried out at the Instituto de Cerámica y Vidrio–CSIC. There he worked in the development of ceramic superconducting thick films. His research interests include the development of new processing techniques for the fabrication of ceramic-based composites, in particular hierarchical composites with bioinspired architectures, the study of high temperature interfacial phenomena such as spreading, the fabrication of graphene-based structures and composites and the development of new materials to support bone tissue engineering.

out for its highest dopa content (~30 mol%), with dopa recognized as a crucial adhesive primer facilitating strong underwater adhesion at the plaque interface.[35] Apart from dopa, hydrophobic and charged residues contribute to underwater adhesion through the modulation of hydrophobic, cation–π, or electrostatic interactions.[36,37] It is important to highlight that while dopa offers impressive adhesion properties, it is prone to unwanted oxidation. To counteract this, mussels have evolved mfp-6, which contains a high concentration of thiol groups (2 mol%), effectively mitigating the redox chemistry of dopa and ensuring durable adhesion even in oxidative environments.[38]

Research into the fundamental adhesion mechanisms present in bio-adhesive surfaces has spurred advancements in artificial adhesives.[5,11,12,39–46] As a result, a multitude of artificial adhesives have emerged, including those leveraging van der Waals forces *via* cylindrical arrays,[47,48] suction-based arrays resembling suction cups,[8,49–52] capillary-based nanopillar arrays enveloped in thin layers of mucus,[17,53] adhesion protein-based adhesives,[54–56] and combinations thereof.[7,57] These biomimetic artificial adhesives hold promising applications across various domains such as biomedical engineering,[39,58–61] soft electronics,[62–65] and industrial fields including transfer printing,[66] precision manufacturing,[67,68] and climbing robots.[69,70] Notably, recent advancements have been made in the development of intelligent adhesives capable of switching their adhesion properties in extreme environments, particularly for applications in aerospace and the deep sea.[71,72]

In this work, we aim to examine the adhesion strategies observed in several prominent natural examples and explore the endeavors undertaken to replicate these in bioinspired adhesives. Additionally, this review will also delve into the manufacturing techniques and adhesion assessment methodologies involved. Special emphasis will be placed on the evolution of biomimetic artificial adhesives, and the responsive capabilities of smart adhesive systems. After that, the latest applications of these bio-inspired adhesives across diverse domains such as droplet manipulation, climbing robots, soft grippers, wearable electronics, and biomedical engineering are demonstrated. The objective is to identify commonalities and differences by reviewing recent advancements in the field, as well as to discuss current challenges and pinpoint future directions.

2. Adhesion theory

Interfacial adhesion stands as a core characteristic of solid surfaces, profoundly shaped by the chemical composition and intricate microscopic structure of material surfaces. Within this segment, a spectrum of surface interactions is explored, encompassing surface and field forces (*e.g.*, van der Waals forces, electrostatic forces, and magnetic forces), material bridging mechanisms (*e.g.*, capillary forces, diffusion, and mechanical interlocking), liquid surface tension, suction, and chemical bonds (Fig. 2).[73] Subsequently, the discourse will delve into distinctive surface adhesion models that are rooted in various adhesion systems, including solid–liquid, liquid–liquid, and solid–liquid–solid adhesion systems.

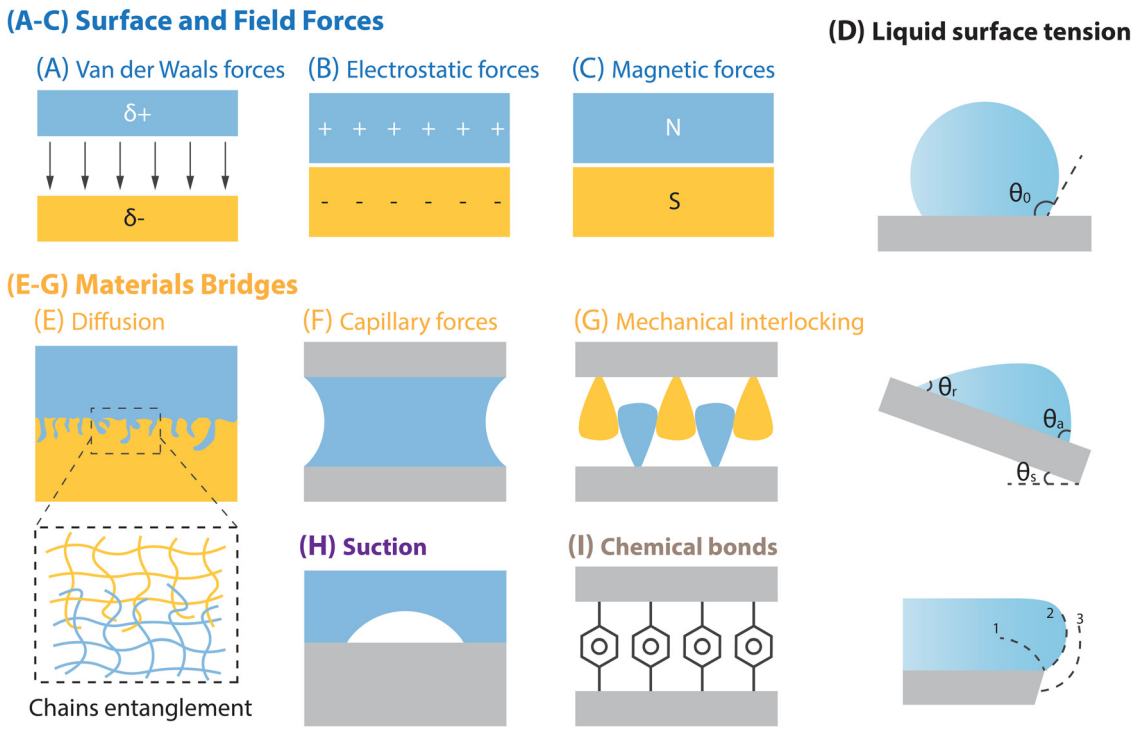

Fig. 2 Depiction of various categories and attributes of primary adhesive interactions. (A)–(C) Surface and field forces, including (A) van der Waals forces, (B) electrostatic forces and (C) magnetic forces. (D) Liquid surface tension, which helps liquids to adhere to solid surfaces in the form of drops. (E)–(G) Material bridging, encompassing (E) diffusion, (F) capillary forces and (G) mechanical interlock. (H) Suction forces. (I) Chemical bonds.

2.1. Various types of interfacial interactions

2.1.1. Surfaces and field forces. Surface forces and field forces denote the diverse array of forces operative at interfaces, exerting influence over object interactions and movement. Typical surface forces and field forces comprise van der Waals forces, electrostatic forces, magnetic forces, and surface tension.

2.1.1.1. van der Waals forces. van der Waals forces (Fig. 2A) are the attractive forces between molecules, akin to gravitational forces, with their scope generally encompassing the London dispersion force (induced dipole-induced dipole interaction), Keesom force (dipole–dipole interaction), and Debye force (dipole–induced dipole interaction).[74,75] Given the ubiquity of London interactions, van der Waals forces manifest in all contact systems, exhibiting a force range typically spanning from 0.2 to 40 nanometers.[75] A notable example of efficient reversible adhesion through van der Waals forces in nature is the gecko's foot pads.[14,16] However, adhesion based on van der Waals forces is often limited by environmental conditions. For instance, in humid or underwater environments, the adhesion can fail due to hydration.[76]

2.1.1.2. Electrostatic forces. The electrostatic force, at its core, is an external force generated when electric charges produce electromagnetic fields, resulting in mutual forces: a form of magnetic interaction. Unlike van der Waals forces, which are attractive, electrostatic interactions can be either attractive or repulsive, occurring between surfaces with opposite or identical charges (Fig. 2B).[77–79] However, electrostatic interactions can prevail even at significant distances of several micrometers, typically exerting much greater influence than van der Waals forces. This electrostatic interaction can be achieved through charge transfer caused by friction, recent research has demonstrated that electrostatic forces can be utilized to increase the strength of dry adhesion.[80] On the other hand, when an object with static electricity approaches another object that lacks static electricity, electrostatic induction causes the nearby side of the uncharged object to accumulate charges of opposite polarity to those on the charged object (while the far side accumulates an equal number of charges of the same polarity). This attraction between opposite charges results in the phenomenon known as "electrostatic adsorption".[81] However, this electrostatic adsorption capability causes the corresponding biomimetic dry adhesive to easily attract tiny dust particles from the environment, consequently reducing its adhesion performance.

2.1.1.3. Magnetic forces. The magnetic force is notably less potent compared to the electrostatic force between molecules, and its strength decreases inversely with the cube of the separation distance between magnetic dipoles (Fig. 2C).[75,82] Nevertheless, the significance of magnetic interaction escalates with the augmentation of the molecule or particle volume, rendering it pivotal in larger molecules or particles. Creating adhesives with magnetic adhesion involves incorporating ferromagnetic particles into polymer prepolymers. In such biomimetic adhesives, magnetic adsorption typically operates on the adhesive interface in two ways: (1) ferromagnetic particles are distributed throughout the adhesive body, and an external magnetic field is used to apply additional attraction or repulsion, thereby adjusting the adhesive strength. (2) Ferromagnetic particles are integrated into the micro-nano ciliary structure of the adhesive, and an external magnetic field is used to modify the distribution of contact cilia, which alters the contact between the adhesive and the surface, thereby adjusting adhesion. Although this type of adhesive can function in air, humid, and underwater environments, its main limitation is the necessity of an external magnetic field.

2.1.1.4. Surface tension. Surface tension refers to the interfacial energy present between surfaces that are physically and/or chemically dissimilar.[83] It can manifest at the interface between gases and solids, between two distinct solids, or between the liquid and vapor phases of the same fluid. In this work, our attention is directed towards liquid surface tension (liquid/vapor, liquid/solid and $liquid_1$/$liquid_2$ interfaces), a characteristic of a liquid's surface that grants it a distinct level of tension, providing resilience and stability against external disturbances.[84,85] While various attractions and repulsions occur within the liquid, molecules at the surface can only interact with those inside and at the periphery, causing surface molecules to contract inwardly. This tendency allows the liquid surface to resist external disturbances and form a relatively stable surface. The value of liquid surface tension depends on the nature of the substance that forms an interface with the liquid, and the magnitude depends on additional factors such as temperature. Generally, higher surface tension renders the liquid surface more resistant to destruction, resulting in more stable droplets or liquid interfaces. This property holds significant importance across numerous applications, including droplet formation on solid surfaces (*e.g.* the wet-cleaning characteristics of lotus leaf surfaces, the water-collecting abilities of spider silk and cactus thorns, and the floating capability of water spiders on the water's surface, *etc.*),[84] stabilization of bubbles/oil droplets in water, and interfacial liquid adsorption (Fig. 2D).[4,86]

2.1.2. Materials bridges. Material bridging pertains to the interface force generated by the material itself acting as a medium. This encompasses entanglements induced by molecular diffusion, capillary forces resulting from liquid media, and friction originating from the mechanical interlocking of microstructures.

2.1.2.1. Diffusion. Diffusion primarily manifests between two miscible polymers through the entanglement of chains, leading to a substantial enhancement in interfacial adhesion (Fig. 2E), which usually occurs in solid–solid adhesion interfaces. This phenomenon finds extensive application in various areas of research, including investigations into self-healing polymers and the improvement of interfacial toughness.[87–89] However, this adhesion mechanism is typically limited to specific adhesive and adherend combinations, making widespread adoption challenging.

2.1.2.2. Capillary forces. Capillary forces (Fig. 2F) emerge when liquid occupies the space between two surfaces, potentially bolstering adhesion significantly.[90,91] This phenomenon

could be found in solid–liquid–solid adhesion interfaces, a typical example of efficient, reversible adhesion *via* capillary forces in nature is found in the pads of tree frogs.[45] The rationale behind capillary forces stems from wetting and thermodynamic adsorption theories. Successful wetting signifies robust affinity and exceptional adhesion between the liquid and solid surfaces. This adhesive mechanism effectively addresses the issue of adhesion failure due to hydration encountered in gecko-inspired dry adhesion relying on van der Waals force. However, its maximum adhesive capacity cannot match that of dry adhesives based on gecko pads.

2.1.2.3. Mechanical interlocking. Mechanical interlocking denotes an extra force, friction, which resists the separation of two solids (Fig. 2G). This form of interlocking is versatile and can be utilized regardless of surface chemical characteristics and environmental circumstances, thus it can appear in solid–solid adhesion systems and solid–liquid–solid adhesion systems. Natural surface structures that facilitate interlocking include hook-like formations on specific plant fruits, head-to-body interlockers seen in dragonflies, and wing-to-body interlockers present in beetles.[92,93] This adhesion mechanism is versatile and applicable across various materials, facilitating broad promotion. However, it often necessitates specific characteristics such as shape, size, and microstructural features of both the adhesive and adherend surfaces.

2.1.3. Suction force. Suction forces (Fig. 2H) are determined by multiplying the surface area of the suction cup by the disparity in pressure between its interior and the surrounding environment. This force is considerable and can be harnessed to attain dependable adhesion to targeted surfaces. Numerous organisms utilize suction forces for adhering to substrates, illustrated by the suckers of octopuses and the oral suckers of climbing fish.[94,95] However, the effectiveness of this adhesion mechanism is constrained by the construction technology of the adhesive suction cup, which often involves complex adhesive structure fabrication. Moreover this method is typically more suitable for liquid environments since liquids are less compressible than air, resulting in more stable adhesion forces formed by pressure differences.

2.1.4. Chemical bonds. Chemical bonds (Fig. 2I) refer to the strong interactions between two or more adjacent atoms (or ions) within a molecule or crystal, *e.g.* covalent bonds (0.1–0.2 nm length), metallic bonds, and ionic bonds, each resulting from different mechanisms.[75,96] These bonds arise from the electrostatic attraction and repulsion between electrons and atomic nuclei. Although chemical bonds are typically very robust (approximately 200–400 kJ mol^{-1}), their formation requires specific physicochemical properties of the two interacting interfaces in the adherent system. Marine mussels are a prime example of adhesion through chemical bonds.[97] These mussels can rapidly attach to various surfaces in seawater by secreting six primary adhesive proteins (mfp-1 to mfp-6) that form byssal threads. These mussel foot proteins are rich in dopa, which enhances adhesion through oxidative covalent bonds. Initially, dopa is oxidized to dopaquinone, which then gradually forms covalent bonds with primary amines and thiols, resulting in highly effective attachment.[34] While chemical bonding is highly stable and dependable, it frequently lacks reversibility.

2.2. Interfacial adhesion models

To quantitatively characterize the adhesion behavior at the contact interface of an adhesion system, we delve into various adhesion models tailored to solid–liquid, solid–solid, and solid–liquid–solid adhesion systems (Fig. 3). This encompasses the Cassie model, transition model, and gecko model, which are relevant to solid–liquid adhesion systems. For solid–solid adhesion systems, we explore the Kendall model, JKR model, suction model, and mechanical interlocking & friction model. Additionally, for solid–liquid–solid adhesion systems, we introduce the capillary model, adhesive secretion model (chemical bonds), and underwater suction model. These models provide valuable insights into the mechanics of adhesion across different interface configurations.

2.2.1. Solid–liquid interfacial adhesion models. When discussing the adhesion behaviors for solid–liquid systems, it becomes essential to consider the wetting dynamics of the liquid on the solid surface. Upon depositing a droplet onto a smooth solid surface (Fig. 3A), it promptly reaches an equilibrium state, quantifiable by the intrinsic contact angle (θ) introduced by Thomas Young.[98] In this ideal scenario (the solid surface is flat, chemically uniform, homogeneous, and ideally rigid), it is evident that a smaller contact angle of the droplet on the solid surface correlates with a higher adhesion force.[84,85] However, real solid surfaces often exhibit roughness, resulting in various contact states between the liquid and the solid interface. These states include the fully wetted Wenzel state (Fig. 3B), the Cassie–Baxter state where the liquid only wets the top of the solid surface (Fig. 3C), and the transition state that partially realized microstructural wetting (Fig. 3D). In such cases, defining the adhesion of the liquid to the solid surface solely based on the contact angle becomes challenging. For instance, achieving lower adhesion with a smaller contact angle is possible, as observed in Nepenthes alata,[99] while higher adhesion with a larger contact angle is also feasible, as seen in Salvinia molesta.[100]

The adhesion between the droplet and the surface could be quantified by the contact angle hysteresis (CAH) caused by the roughness, uneven chemical composition, and contamination of the solid surface.[84] The upper limit of CAH is defined as the advancing contact angle (θ_{Adv}), while the lower limit of CAH is defined as the receding contact angle (θ_{Rec}). In other words, the advancing angle is the contact angle formed when a liquid spreads over a solid surface, causing the solid–liquid interface to supersede the solid–gas interface. Conversely, the receding angle is the contact angle formed when the liquid withdraws from the solid surface, with the solid–gas interface replacing the solid–liquid interface. Normally, the value of θ_{Adv} is consistently higher than θ_{Rec}, and their difference (θ_{Adv}–θ_{Rec}) represents the contact angle hysteresis, which determines the ease of droplet rolling off (detaching from) an inclined solid surface. A larger hysteresis indicates a lower likelihood of droplets moving on the surface. The slide/sliding angle (α) denotes the minimum tilt angle needed for a droplet with

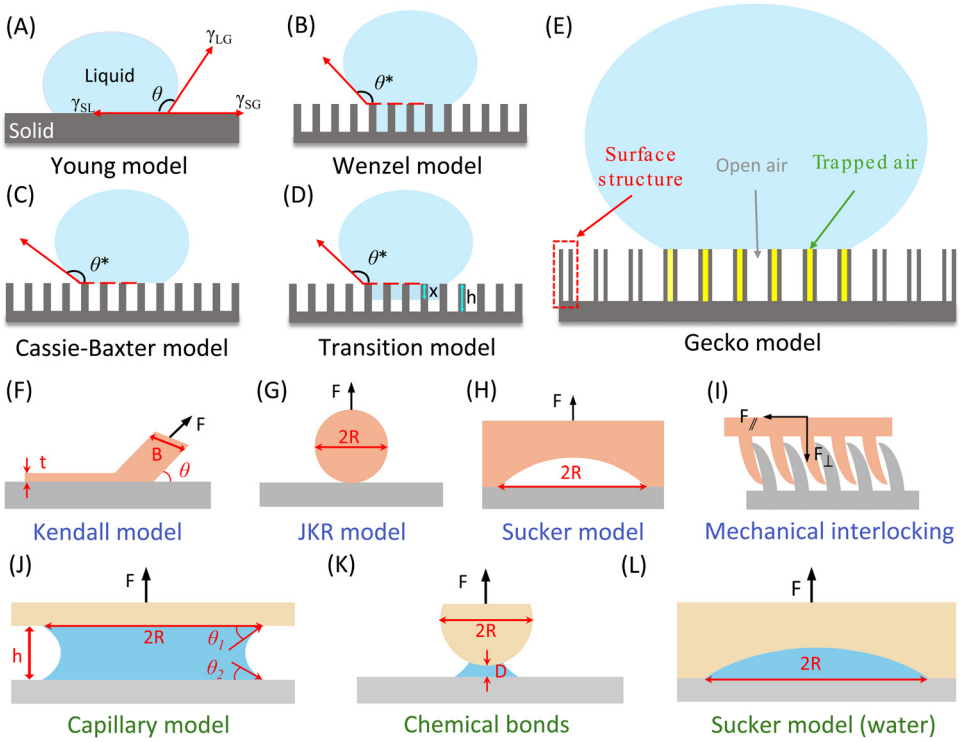

Fig. 3 Interfacial adhesion models for different adhesion systems. (A)–(E) Interfacial adhesion models for the solid–liquid system. (A) Schematic diagram depicting a droplet's deposition onto a smooth surface, where θ represents the intrinsic contact angle. (B)–(D) Schematic of the droplet state on a rough surface, (B) Wenzel state, (C) Cassie–Baxter state, (D) transition state, θ^* represents the apparent contact angle. (E) "Gecko" wetting model in air, with a surface structure of internal hollow nanopillars. (F)–(I) Interfacial adhesion models for the solid–solid system. (F) Kendall adhesion model. (G) Johnson–Kendall–Roberts adhesion model. (H) Sucker adhesion model. (I) Mechanical interlocking & friction adhesion model. (J)–(L) Interfacial adhesion models for the solid–liquid–solid system. (J) Capillarity and Stefan adhesion model. (K) Adhesive secretion model. (L) Sucker adhesion model.

specific volume to move on a solid surface, providing an intuitive reflection of CAH (on superhydrophobic structures, as the droplet state can be more vividly described as rolling, it is also known as the rolling angle). Furmidge's equation describes the relationship between the sliding angle and the advancing and receding contact angles as follows:[101]

$$mg\sin\alpha = \gamma_{LG}W(\cos\theta_{Rec} - \cos\theta_{Adv}) \quad (1)$$

where, m is the droplet mass, g is the gravity acceleration, γ_{LG} is the liquid–gas interfacial tension, and W is the contact surface diameter of a liquid droplet on a solid surface. Consequently, we can know that a lower contact angle hysteresis (low adhesion) results in a correspondingly reduced rolling angle.

Here, we will introduce three contact models that can cause high adhesion behavior of droplets on superhydrophobic solid surfaces from a structural perspective, namely Wenzel model, the transition (Wenzel–Cassie) model, and the "gecko" model (Fig. 3E). In the Wenzel state (Fig. 3B), droplets adhere tightly to the surface, leading to a significant contact angle hysteresis (a strong adhesive force, the "red petal" state is considered a special case of the Wenzel state).[102] When it comes to the Cassie state (Fig. 3C), the droplet is not in entirely contact with the whole surface, air is present between the droplet and the bottom of the groove on the solid surface, allowing easy droplet moving, resulting in a small contact angle hysteresis (a weak adhesive force, the "Lotus" effect is seen as a special case of the Cassie state). The sliding angle, in this context, can only reflect the contact angle hysteresis (adhesion behavior) of the Cassie state, not the Wenzel state where droplets are pinned (high adhesion) to the surface. However, even on surfaces exhibiting the Cassie state, the presence of individual micro or nanostructures can lead to high contact angle hysteresis, resembling a pinning state in the related area. Consequently, the sliding angle can only represent the contact angle hysteresis (adhesion behavior) for the entire system, failing to account for these pinned structures.[103,104] Moreover, when a droplet makes contact with an actual sample, the entire system is often under a metastable state transition state, (Fig. 3D) where both the Wenzel state and Cassie–Baxter states coexist.[105] Under this situation, some parts of the surface are wetted by the liquid, while other parts are filled with air within the structure.[106–115] In the case of such surfaces, the droplet experiences an energy barrier that hinders the transition between the Cassie–Baxter and Wenzel states. When the super-hydrophobic state shifts from the Cassie–Baxter state to the Wenzel state, the droplets will infiltrate the microstructure of the solid surface, leading to an increased adhesion between the liquid and the surface.[116–118] Recently, some enhanced models have been proposed by researchers to explore the coexistence and transition between the Wenzel state and the Cassie–Baxter state. These novel models offer innovative approaches to designing and forecasting functional surfaces with specific adhesion properties.[105,114,119–129] For instance, Patankar[119]

Table 1 Research for transition between Wenzel state and Cassie–Baxter state

People	Main contrition	Ref.
Lafuma & Quere	Confirmed irreversible shifts from air to the Wenzel regimes in superhydrophobic states	105
Hoffmann *et al.*	The transitions between the Wenzel state and Cassie–Baxter state are presented based on various roughness parameters	131
Marmur *et al.*	The transitions were analyzed by placing the Wenzel and Cassie–Baxter equations in a suitable mathematical thermodynamic perspective	132 and 133
Zeng *et al.*	Demonstrated that both states can coexist on a nano pillared surface through the utilization of molecular dynamic simulations	122

observed that roughness enables a droplet to have multiple metastable equilibrium positions, and it can transition between these positions if the corresponding energy barriers are surmounted. The Cassie configuration represents the lowest energy state in the open state, whereas the Wenzel configuration corresponds to the lowest energy state in the wet hydrophobic state.[130] Both the Cassie and Wenzel configurations are local energy minimum states, and the droplet's adhesion behavior depends on which of these states has the lower energy. If $\theta_C^* > \theta_W^*$, the droplet forming the open state will have higher energy than the Wenzel state.[105] According to the energy barrier principle, a transition may occur between the Cassie and Wenzel configurations. Table 1 summarizes research related to the transition state.

To create a superhydrophobic surface with sufficiently high liquid adhesion for lossless liquid transport, Jin *et al.* employed hydrophobic PS as the raw material and utilized the porous alumina template method to synthesize a polystyrene (PS) nanotube layer comprising around 6×10^6 aligned nanotubes per square millimeter, resembling the bristles on a gecko's feet.[134] This superhydrophobic high adhesion induced by the gecko-inspired superhydrophobic PS nanotube layer is commonly referred to as the "gecko" state (Fig. 3E). Distinct from Cassie state (low adhesion), although there is also an air layer between the droplet and the bottom of the surface groove for this wetting state, it shows exceptionally high adhesion to the droplet.[134] In the Cassie state, the external atmosphere is connected to the air pockets within the surface grooves, also defined as "open state". While in the "gecko" state, there are two different types of gas pockets can be observed within the PS nanotubes: a completely closed-air pocket in the nanotubes and an open-air pocket in the surface grooves connected to the atmosphere.[134] In this configuration, the presence of trapped air within the open-air pocket contributes to a higher contact angle, while the capillary force within the closed-air pocket results in exceptionally high adhesion.

2.2.2. Solid–solid interfacial adhesion models. Solid–solid interfacial adhesion is prevalent in our daily lives, representing one of the most common adhesive systems. To elucidate the adhesion dynamics at their contact interfaces, the Kendall model, JKR model, suction model (which would be introduced in the Solid–liquid–solid interfacial adhesion models section), and mechanical interlocking & friction model are frequently employed.

2.2.2.1. Kendall model. The Kendall model, serving as a fundamental adhesion model, is frequently employed to describe the peeling process of a thin adherent film. Given the resemblance between the peeling mechanisms observed in natural organisms and those of tape, researchers have been inspired to simplify adhesive pads as single strips of tape. As illustrated in Fig. 3F, when a tape with a width of B is peeled off from an adherend surface with a fixed peeling angle (θ), the corresponding peeling force conforms to the Kendall equation:[135]

$$F = \frac{B\gamma}{1 - \sin\theta} \tag{2}$$

where, γ is the adhesion energy per unit area of the tape, which is proportional to the tape's peeling force, F, exerted on the tape. As the peeling angle is capable of fluctuating across a broad spectrum, the peeling force can transition from a substantial magnitude to a minimal one. This variability in peeling force elucidates why numerous natural organisms, such as geckos,[136] tree frogs,[137] and others, can modulate adhesion by maintaining a small pulling angle for substrate adherence and employing a larger peeling angle for detachment.

2.2.2.2. Johnson–Kendall–Roberts model. The conventional Hertz contact model elucidates the contact dynamics between two elastic spheres subjected to an external force. However, due to the omission of interfacial attraction, the Hertz model inadequately characterizes and predicts the adhesion force at contact interfaces. The JKR model enhances the Hertz model by incorporating surface attraction into the interaction between two spheres, addressing the force needed to separate an elastic sphere with radius R from a plane. When dealing with an adhesion surface featuring micro- and nanoscale contact structures, the adhesion is typically treated as a spherical contact situation (Fig. 3G). In such cases, the adhesion force can be determined using the JKR equation:[138]

$$F = \frac{-3\pi R\gamma}{2} \tag{3}$$

where, R is the radius of the sphere and γ is the interfacial adhesion energy per unit area. In 2003, Arzt *et al.* made further refinements to the JKR model by considering the improved adhesion resulting from the subdivision of contact elements into finer sub-contacts. The corresponding equation is provided below:[15]

$$F = -\frac{3}{4}\pi D^2 \tau \sqrt{N_A} \tag{4}$$

where, τ is the adhesion energy per unit area, D is the dimensional parameter of the total apparent contact diameter, and N_A represents the areal density of the contact elements. It can be known that the

adhesion force F will increase as the areal density of the contact elements increases.

Based on the JKR model's principle, the interfacial adhesion strength (σ_{ad}) of a biological adhesive system is the ratio of adhesion force (F) to adhesion area (S).[138] Therefore, σ_{ad} can be expressed as $\sigma_{ad} = \frac{F}{S} = \frac{F}{\pi R^2} = \frac{-3\gamma}{2R}$. It can be known from this equation that for an adhesive featuring micro-nano adhesion structures, its interfacial adhesion strength decreases as the size of its terminal adhesion structure increases. This formula effectively explains why the adhesive unit structures on the sole of an animal become smaller as the animal's weight increases. This is because a smaller size of the adhesion structure corresponds to a larger value of σ_{ad}. This concept is termed as contact splitting, which effectively elucidates the relationship between the size of biological adhesion unit structures and their mass. It is worth noting that in the JKR model, a paradox arises due to the deformation height (z), which is defined as $z = r^2/2R$,[138] where r represents the contact interface radius. If we adhere to this definition of deformation height, the result predicted by the JKR model is that as the size of the contacting objects diminishes, the corresponding interface bonding strength will increase infinitely.[11] The prediction appears untenable, since the bond strength of the adhesive structure should not surpass the van der Waals theoretical limit.[139] In an effort to rectify the shortcomings of the JKR model, Gao *et al.* proposed a modification wherein the deformation height is represented by $z = R - \sqrt{R^2 - r^2}$. As a result, the revised JKR model can be formulated as:[139]

$$\frac{F}{\pi R^2 \sigma_0} = \begin{cases} 2\eta - \eta^2, & \eta < 1 \\ 1, & \eta \geq 1 \end{cases} \quad (5)$$

where, σ_0 represents the theoretical strength of the van der Waals interaction, while η is defined as $\Delta\gamma/(R\sigma_0)$, with $\Delta\gamma$ representing the van der Waals interaction energy. Consequently, the adhesion strength is constrained by the theoretical strength of the van der Waals interaction. Additionally, it is important to acknowledge that the JKR model primarily applies to the description of elastic solid–solid contact at the micro- and nanoscale under dry conditions.

2.2.2.3. Mechanical interlocking & friction model. Biological surfaces can also enhance adhesion by utilizing mechanical interlocking and friction between their micro-nano structures and the irregular surface of the substrate (Fig. 3I). As a result of the variations in micro-nano structures on biological surfaces and the intricate nature of interlocking effects, there is no single unified mechanical interlocking adhesion model. For instance, Jeong *et al.*[140] proposed a relevant theory centered around a particular adhesive microhook adhesion system that involves mechanical interlocking. The equations for normal ($F_\perp$) and shear ($F_\parallel$) interlocking adhesion forces resulting from the interaction between two substrates with microhooks are provided below:

$$F_\perp = nF_{ext} = n\left(F_{b,t} + \frac{1}{3}F_{ad} + f_1 + f_2\right) \quad (6)$$

$$F_\parallel = nF_{ext}\cos\theta_{ext} = n\left[F_x\cos\left(\frac{\pi}{2} - \theta_p\right) + F_y\cos\theta_p\right] \quad (7)$$

where n and θ_p are the number and inclination angle of microhooks, respectively, θ_{ext} is the angle of external force from a horizontal surface. f_1 and f_2 are the friction force of the interlocked microhooks (different structures), F_{ext} is the external force acting on the single microhook, F_x and F_y are the external forces along the x and y directions, $F_{b,t}$ is the bending force at the end of the microhook, and F_{ad} is the adhesion force between the surface and the substrate.

2.2.3. Solid–liquid–solid interfacial adhesion models. Apart from the adhesion that happens in the air, a significant portion of adhesion occurs in underwater environments, observed in organisms like mussels, barnacles, octopuses, and others. Furthermore, certain organisms such as tree frogs, snails and beetles will secrete mucus from their soles, even though they primarily move inland. Consequently, the corresponding adhesion system transitions from a solid–solid to a solid–liquid–solid configuration. Adhesion models for such adhesion systems primarily comprise the capillarity and Stefan adhesion model, chemical adhesive secretion model, and sucker model.

2.2.3.1. Capillarity and Stefan adhesion model. Within intricate natural settings, liquids often exist between contact interfaces, rendering the JKR model inapplicable. Hence, it becomes imperative to establish an adhesion contact model suitable for humid environments. When an external force is exerted on an interface where two surfaces are separated by a drop of liquid between them, the droplet would spread to form a liquid film between the two surfaces due to the action of surface tension and Laplace pressure, endeavoring to prevent the gap between the two solid surfaces from widening.[45] The force exerted by the liquid film to prevent the separation of the solid surfaces is known as capillary force (Fig. 3J), denoted as F_C. The Young-Laplace pressure P for a cylindrical fluid confined between two flat surfaces can be expressed as follows:[141]

$$P = -\gamma\left(\frac{1}{R} + \frac{1}{r}\right) \quad (8)$$

where R is the liquid's radius of curvature, r denotes the liquid bridge radius, γ represents the mucus surface tension. According to the geometric relationship, the curvature radius R could be expressed as $R = \frac{h}{\cos\theta_1 + \cos\theta_2}$.[142] Therefore, the capillary force F_C can be expressed as:[143,144]

$$\begin{aligned} F_C &= \pi r^2 P = \pi r^2\left[-\gamma\left(\frac{1}{R} + \frac{1}{r}\right)\right] \\ &= \pi r^2\left[-\gamma\left(\frac{\cos\theta_1 + \cos\theta_2}{h} + \frac{1}{r}\right)\right] \\ &= -\pi r^2\gamma\frac{\cos\theta_1 + \cos\theta_2}{h} - \pi r\gamma \end{aligned} \quad (9)$$

where h is the height of the mucus film, θ_1 and θ_2 are the contact angles of mucus and pad/substrate, respectively. According to this equation, we know that the capillary force could experience a substantial rise with the presence of an

extremely thin liquid bridge, elucidating why tree frogs require exceedingly thin liquid bridges on their toe pads, achieved by expelling excess liquid through specialized channels.[11]

2.2.3.2. Chemical adhesive secretion model. In underwater environments, the applicability of the capillarity and Stefan adhesion model diminishes, as organisms predominantly depend on suction or the secretion of adhesion proteins to attain underwater adhesion. When employing such liquid secretions in underwater conditions, the circumstances surrounding the contact interface between the substrate and adhesive play a crucial role in determining the molecular contact characteristics. For instance, the pressure at which the liquid secretion is applied can influence the kinetics of interstitial water drainage. With fluid present at the interface during low separation, a hydrodynamic force may emerge (Fig. 3K). This force can be quantified using Reynold's equation:[145]

$$F = \frac{6\pi R^2 \eta \nu}{D} \tag{10}$$

where, R denotes the adhesive drop's radius, η represents the viscosity of the adhesive drop, and D signifies the closest distance between the adherend surface and the adhesive drop. Under the influence of hydrodynamic forces, the liquid secreted will displace the initial liquid between the adhesive and the adhered substance, initiating preliminary adhesion *via* physical forces like hydrogen bonding, supramolecular interaction, coordination, and complexation.[5,41] With prolonged action time, the secreted adhesive liquid will forge robust adhesion between the adhesive and the adherend through ensuing chemical reactions.

2.2.3.3. Sucker model. The sucker adhesion model was originally utilized to describe the underwater adhesion surfaces of octopus and other fish species, which have structures similar to octopus suckers, albeit much smaller in size. These aquatic organisms usually utilize suction force to achieve underwater adhesion, which mainly comes from the pressure difference between the inside and outside of the sucker. But this adhesion model can also be applied in air environments. However, due to the sealing effect limitation, the adhesion it can provide in the air is much less than that in water. As shown in Fig. 3H and L, the corresponding suction formula for one sucker is as follows:[146,147]

$$F = (P_0 - P_C)\cdot\pi R^2 k \tag{11}$$

where, P_C is the sucker cavity's pressure; P_0 is the environmental pressure; R is the contact surface radius; and k is the suction cup's yield rate (a parameter used to determine the actual contact area of the suction cup). When the suction cup adheres to the substrate, it deforms to some extent, causing the actual contact area to be smaller than the suction cup's original area. Therefore, we use k to reflect the corresponding yield rate of suction cup here, and $k\pi R^2$ is the actual contact area between the suction cup and the substrate. It can be seen from eqn (11) that the suction force of the suction cup is positively correlated with the corresponding actual contact area. Additionally, with a constant suction cup structure and size, the pressure difference and the yield of the sucker become the key factors influencing the suction force. Consequently, the sealing function of suckers holds paramount significance. And the adhesion strength that relevant organisms can achieve is the sum of the adhesion forces generated by all suckers they used for bonding.

In summary, after decades of development, researchers have established a comprehensive interfacial adhesion system encompassing solid–liquid, solid–solid, and solid–liquid–solid adhesion systems. For the solid–liquid adhesion system, scientists primarily manipulate surface wettability to switch between the Cassie and Wenzel wetting models, thereby controlling droplet adhesion behavior. A wetting state closer to the Wenzel model results in greater droplet adhesion force, while a state closer to the Cassie model results in lower adhesion force. Thus, when designing wetting surfaces, the target wetting state can be tailored to achieve the desired adhesion behavior. In the solid–liquid–solid adhesion system, the main adhesion models include the capillary and Stefan model, suction cup model, and adhesive secretion model. Each model is highly specific to particular structures or compositions. For example, the capillary model is typically used for biomimetic adhesives imitating the wet adhesion of tree frogs, the suction cup model for adhesives mimicking the suction adhesion of octopus suckers, and the adhesive secretion model for adhesives that start as a liquid and solidify over time. Compared to these two adhesion systems, the solid–solid adhesion system is relatively complex due to the variety of interactions that can occur. For instance, when the entire biomimetic adhesive (such as mussel-inspired hydrogel tape) contacts the adherend, the Kendall adhesion model is most appropriate for characterizing adhesion strength. For biomimetic adhesives with numerous micro-nano structures (such as gecko-inspired adhesives), the primary adhesion occurs at these micro-nano structures, necessitating the use of the JKR model for accurate characterization. Additionally, if the adhesive involves biomimetic structures that provide mechanical interlocking and friction, models accounting for these factors must be considered.

3. Interfacial adhesion characterization

Generally, the interfacial adhesion between solid materials (including both solid–sloid adhesion system and solid–liquid–sloid adhesion system) would be assessed based on adhesive strength and adhesive toughness. The former quantifies the maximum force per unit area, while the latter indicates the amount of energy per unit area needed to initiate separation. For liquid–solid adhesion system, the contact angle hysteresis is usually used for reflecting interfacial adhesion in practice. As researchers have conducted in-depth studies in the field of adhesion over the years, a series of new methods for measuring adhesion between different materials have been reported, which are suitable for different interfacial adhesion systems.[6,39,44] Even for the same adhesion system, the variability could arise from differences in detachment mechanisms influencing by geometry. For example, the debonding of an

adhesive differs from peeling, which in turn differs from the failure of a sealing adhesive under burst pressure. This section will explore several common techniques for analyzing interfacial adhesion, encompassing schematic geometry, force–distance curves, and typical usage scenarios.

3.1. Solid–liquid adhesion characterization

Various techniques have been developed for assessing the adhesion between liquid droplets and solid substrates, including measurements of advancing and receding angles (θ_{Adv} & θ_{Rec}), sliding angle (SA),[148,149] and even directly use the high-sensitivity microelectromechanical balance to test the adhesion for specific situations. These methods are employed to quantify either contact angle hysteresis (a parameter that could reflect interfacial adhesion strength) or adhesion force. For most situations, we use the contact angle hysteresis parameter to feedback the adhesion between solid and liquid. The specific value of contact angle hysteresis ($\theta_{Adv} - \theta_{Rec}$) can be determined by gradually adding or removing liquid from droplets on the solid surface through the liquid injector.[150] Typical measurement procedures involve controlling droplet volume using a liquid injector while capturing continuous images. As the droplet volume is increased or decreased, the corresponding advancing or receding angle is measured (Fig. 4A).

If droplets exhibit movement on a solid surface when it is tilted, the sliding angle (SA) can also serve as an indicator of the adhesion performance between the droplet and the solid surface. The SA, denoted as α, represents the critical angle formed by the inclined surface and the horizontal plane when the droplet initiates sliding or rolling on the inclined surface. To assess the sliding angle, a liquid droplet is placed on a solid inclined surface until it reaches a critical state before sliding, and the angle α formed by the incline of the solid surface denotes the SA, which could also reflect the adhesion strength between solid and liquid droplet (Fig. 4B).

For the situation that a droplet can be entirely detached from a surface, a high-sensitivity microelectromechanical balance with a resolution of μN could be directly employed to characterize the interfacial adhesion between the solid surface and liquid droplet.[151–153]

Since copper has a high surface tension, droplets tend to adhere to it, making it suitable for testing. Therefore, droplets are attached to a copper ring for measurement (Fig. 4C and D). The typical adhesion test curve for liquid droplets using this device is shown in Fig. 4D. Initially, the substrate is gradually moved closer to the droplet at a constant speed until they make contact (the blue force–distance curve in Fig. 4D). If the effect of pre-loading force on liquid-substrate adhesion is not being studied, the substrate stops moving at this point. If the pre-loading force effect needs to be considered, the substrate continues to move towards the droplet until the target pre-loading force is achieved. The substrate then moves back towards its original position at a constant speed (the red force–distance curve in Fig. 4D). If adhesion exists between the droplet and the substrate, the droplet deforms as the substrate moves away. This deformation continues until the droplet detaches from the substrate. The change in force before and after detachment indicates the adhesion force between them.[154] Finally, the substrate returns to its original position.

3.2. Solid–solid/solid–liquid–solid adhesion characterization

Both the solid–solid adhesion system and the solid–liquid–solid adhesion system primarily gauge adhesion at the solid–solid interface. While environmental factors or specific adhesion

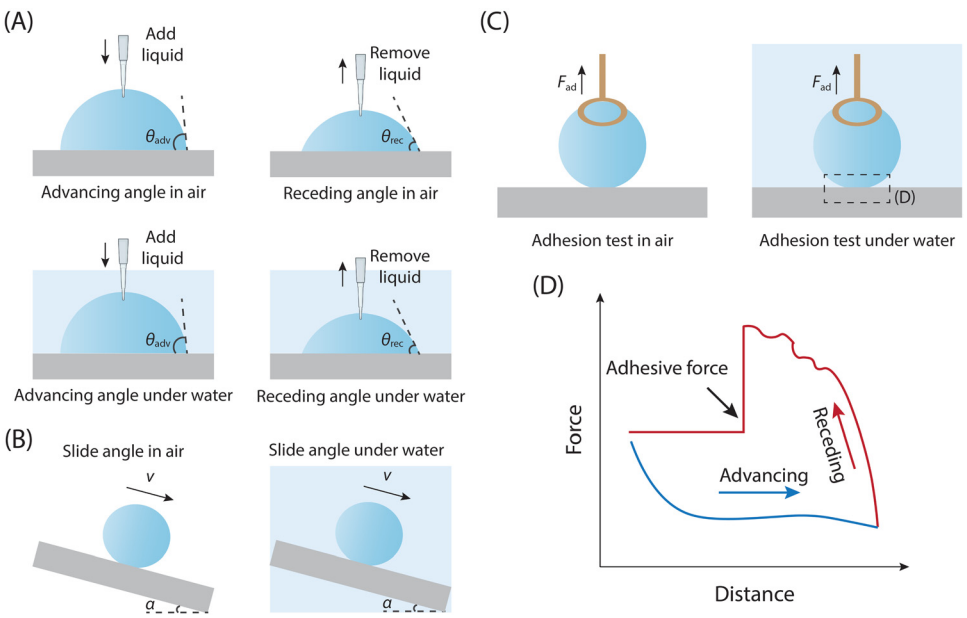

Fig. 4 Illustration of commonly used interfacial adhesion test methods for solid–liquid adhesion (including both in air and underwater environment). (A) Droplet advancing & receding angle (θ_{Adv} & θ_{Rec}) test. (B) Droplet sliding angle test. (C) Droplet adhesive force test. (D) Typical force–distance curve for droplet adhesive force test.

types may introduce a liquid film within this interface, it doesn't affect the fundamental reflection of adhesion forces between distinct solid interfaces. For example, the liquid film could serve as an environmental medium and does not directly act on the adhesion between solid–solid interfaces. However, it may impact the interaction between these interfaces, thus altering the corresponding adhesion force. For instance, hydration can invalidate certain physical interactions like van der Waals forces, supramolecular interactions and hydrogen bonds within the solid–solid interface.[40,155,156] Therefore, what is measured at this time should be the adhesion force of the two solids. Conversely, the liquid film may also act as a significant contributor to the adhesion of solid–solid interfaces, acting as a material bridge, as seen in the wet adhesion of tree frog's feet and snails.[11,157] Under this situation, the liquid film could be attributed to a specific adhesion facilitating mechanism between solid–solid interfaces. As a result, even in solid–liquid–solid adhesion systems, we maintain that the measured force predominantly reflects the adhesion between solid–solid interfaces. The testing methods employed to evaluate solid–solid and solid–liquid–solid adhesion vary primarily based on two factors: (i) the testing purpose, and (ii) the specific adhesion property for testing, including adhesion strength and toughness. Consequently, we categorize the methods for assessing adhesion properties between different solids into the following groups: those for measuring adhesion strength, those for measuring adhesion toughness, those for investigating the influence of contact behavior on adhesion properties (indentation tests), and other special interfacial adhesion test methods (Fig. 5 and Table 2). Pretreatments for different adhesion tests in air and water environments are shown in Fig. 5A and B.

3.2.1. Adhesion strength. The tensile pull-off test represents a common technique employed to assess adhesive bonding strength (Fig. 5C). This testing method involves two adherends that are directly adhered to an adhesive. These surfaces are then pulled apart perpendicular to their interface. The applied tensile force is monitored as displacement occurs until reaching a maximum pull-off force, leading to separation. Normalizing this pull-off force against the contact area provides the strength in pressure units. Although energy can be calculated from the area under a force-displacement curve, the tensile test primarily focuses on obtaining the pull-off force, which serves as an indicator of adhesive strength.[158] It's worth noting that while the experimental setup for this test is relatively simple, achieving accurate results typically necessitates precise alignment of the specimen and careful application of force to prevent the

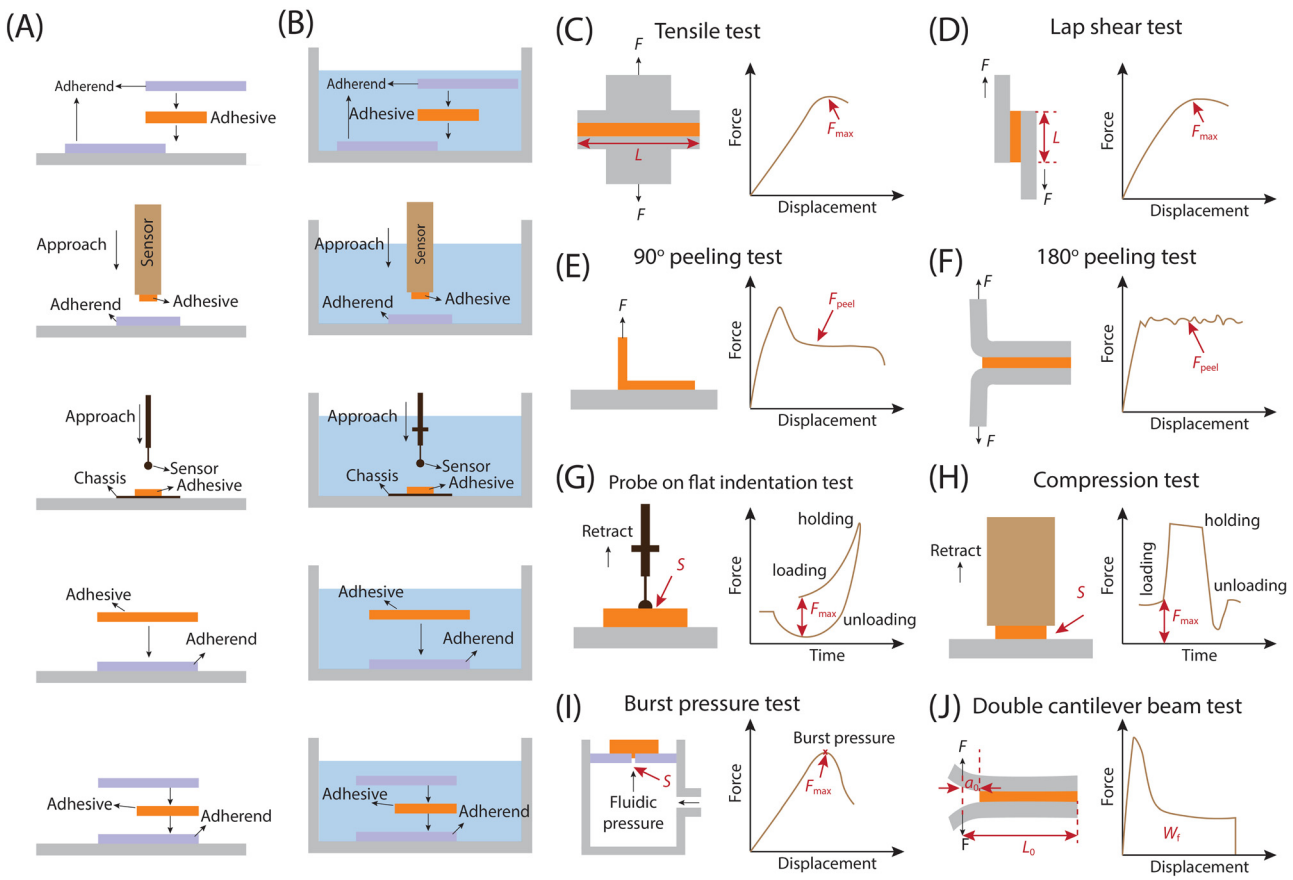

Fig. 5 Illustration of commonly used interfacial adhesion test methods for solid–solid/solid–liquid-solid adhesion(including both in air and underwater environment). (A) and (B) Pretreatments for different adhesion tests, (A) in air, (B) underwater. (C) Tensile test. (D) Lap shear test (E) 90° peeling test (F) 180° peeling test. (G) Probe on flat test. (H) Flat punch test. (I) Burst pressure test. (J) Double cantilever beam (DCB) test.

Table 2 Typical adhesive testing methods encompass geometry, target parameters, calculation formulas and features

Testing methods	Geometry	Target parameters	Calculation formulas	Features	Ref.
Tensile test	Width: W Length: L (adhesive)	Tensile strength (N m^{-2})	$\frac{F_{max}}{WL}$	Normal direction adhesion strength assessment	158
Lap shear test	Width: W Length: L (adhesive)	Shear strength (N m^{-2})	$\frac{F_{max}}{WL}$	Shear direction adhesion strength assessment	159 and 160
90° peeling test	Width: W (adhesive)	Interfacial toughness (J m^{-2})	$\frac{F_{peel}}{W}$	Evaluation of adhesion energy and average peel force at 90° peel angle and certain peel speed	44
180° peeling test	Width: W (adhesive)	Interfacial toughness (J m^{-2})	$\frac{2F_{peel}}{W}$	Evaluation of adhesion energy and average peel force at 180° peel angle and certain peel speed	161 and 162
Probe on flat test	Contact area between spherical probe and adhesive (S)	Spherical adhesion strength (N m^{-2})	$\frac{F_{max}}{S}$	Load-hold-unload contact adhesion analysis of spherical surfaces (the contact area will change)	163
Flat punch test	Contact area between flat probe and adhesive (S)	Planar adhesion strength (N m^{-2})	$\frac{F_{max}}{S}$	Load-hold-unload contact adhesion analysis of planar surfaces (the contact area not change)	164
Burst pressure test	The gap area of the adherend surface (S)	Burst pressure (Pa)	$\frac{F_{max}}{S}$	Analysis of the minimum pressure required to cause rupture or bursting of the adherend surface sealed by adhesive	165
Double cantilever beam test	Adherend width: B Distance from loading point to the end of the adherend: L_0 initial crack length from loading point to bond line: a_0 Effective area of ruptured ligament: $[B(L_0 - a_0)]$	Critical fracture energy (G_{IC}, N mm^{-1})	$\frac{W_f}{[B(L_0 - a_0)]}$	Evaluation of adhesive bond damage and fracture under different loading conditions	166 and 167

introduction of additional stresses, such as bending and peeling stresses, and to ensure the uniform distribution of stress across the specimen.

In addition, adhesives frequently encounter shear stress in practical applications, for instance, topical adhesives may experience shear stress when the underlying substrate is stretched. As a result, the lap shear adhesion test was developed, which involves joining two surfaces by overlapping a defined area (Fig. 5D). Unlike the tensile test, the joint in shear test is subjected to pulling forces parallel to the adhesive interface, and the maximum force used for separation occurs when the adhesive interface separates. This force is used to determine the shear adhesion strength, which is calculated by dividing the force by the corresponding adhesive area.[159,160] The lap shear test evaluates the adhesive's resistance to stress within a plane by subjecting two adherents bonded by the adhesive to shear forces. While this test is commonly employed to reliably assess adhesive properties, it's important to consider that geometric factors such as adhesive thickness and length can significantly influence the measurement outcomes.[39,168]

In summary, both tensile and lap shear adhesion tests offer complementary insights into adhesion strength under different conditions and geometries.

3.2.2. Adhesion toughness (peeling test). The peeling test serves as a widely employed method for assessing adhesive toughness, quantified by the average peel force normalized by the width (Fig. 5E and F).[44] This test is particularly suitable for soft adhesives, especially in scenarios where the adhesive could be peeled off from a substrate. Although the preparation process is similar to that of a shear test (adhesive's geometric features), the primary focus of this test is to evaluate the adhesive toughness of the tape by peeling it from the adherend surface.[169,170] During this process, one end of the adhesive is continuously pulled apart at a fixed angle (θ) to the adhered surface, and this pulling action is typically conducted at a consistent speed. The choice of θ angle—often set at either 90° (Fig. 5E) or 180°—varies based on preferences and the adhesive's flexibility. Another variation is the T-peel test (Fig. 5F), where both adherends are simultaneously pulled apart from one end, simulating individual 90° peeling actions. This setup proves beneficial when dealing with thin and flexible adherends.[161,162] A standard force–distance curve obtained from this test usually depicts a phase where the force stabilizes, signifying the onset of a steady-state peeling process (F_{peel}).[171] For the energy needed for crack propagation (interfacial toughness) in 180° and T peeling test, it is determined by twice the plateau force and then dividing by the adhesive breadth (measured in J m^{-2} or N m^{-1}). Additionally, it's important to recognize that the interfacial adhesion evaluation of an adhesive is influenced by mechanical and viscoelastic nature of both the adhesive and substrate, which means that the test results are closely related to the separation speed during testing. Generally, a stiffer backing may be utilized along with the adhesive to minimize sample stretching during peeling. This is crucial because the peeling process entails the bending of the backing materials and deformation of the adhesives, rendering them highly sensitive to the mechanical and viscoelastic properties of the adhesives.[162]

3.2.3. Indentation testing. The indentation method is particularly well-suited for investigating materials that exhibit heterogeneity at the surface (*i.e.*, comprising multiple surface chemistries) or within material. More precisely, a specific-shaped probe is employed to apply pressure to the substrate until a predetermined displacement and/or force is achieved.

Following a predetermined retention period (the holding time varies from as brief as zero to several hours depending on the experiment's objectives), the probe begins to retract until it is completely free of the substrate. By analyzing both force-*versus*-distance and force-*versus*-time curves generated during the loading-holding-unloading processes, various insights can be gleaned. For instance, the loading phase can yield information on the mechanical properties of the adhesive, such as the elastic modulus.[172] The disparity between loading and unloading phases can shed light on the hysteresis of the system, wherein time-dependent physical or chemical interactions may result in distinct unloading behavior. Notably, the pull-off force, akin to the highest adhesion force experienced during detachment in tensile and lap shear adhesion tests, is a key parameter to consider.

In the indentation test, researchers typically opt to vary the shape of the probe (which can be either curved or flat, Fig. 5G and H) while keeping the substrate shape consistent (flat). During this testing procedure, the adhesive may be affixed to the probe surface to examine how its morphology (flat or curved) affects the adhered surface. Alternatively, the adhesive may be attached to the surface of the pressed substrate to assess its adhesion performance on surfaces with varying curvatures.[44] When employing the indentation test with a flat punch for plane adhesion, a key advantage is the constant and measurable contact area between the probe and the substrate. This feature proves highly beneficial when evaluating underwater adhesion of adhesives, as the contact area remains consistent throughout the test, alleviating the need for real-time monitoring of the contact area under complex operating conditions.[164] In addition, both sides of the test setup consist of flat sheets, simplifying the fabrication process.[173] This testing configuration proves advantageous when the adhesive, intended for testing as a probe, is challenging to shape into a curved surface. To achieve accurate measurement, precise alignment of the probe and substrate planes is required.[174] Notably, elevated stresses occur at the edges of the contact between the punch and adhesive, leading to increased strain and additional viscoelastic effects within this area.[174,175]

The indentation geometry involving a probe-on-flat configuration allows for the adjustment of the contact area by varying the compressive load. In numerous investigations, a glass or silicone (polydimethylsiloxane, PDMS) probe is employed to indent the surface under study.[163] Importantly, the adhesive itself can be shaped into the probe and utilized to indent other materials, offering insights into the adhesive interactions with various surfaces. Employing the adhesive as a probe proves especially beneficial for examining adhesion to materials challenging to shape into alternative forms, such as tissue.[164] The resultant indentation data can be analyzed within the context of contact mechanics.

3.2.4. Other special interfacial adhesion test methods. While the methods mentioned above are valuable for adhesive comparison and aid in selecting the most suitable adhesive for a specific application, they often fail to comprehensively represent the wide range of adherent properties and usage environments. Consequently, employing other test models may be necessary to simulate specific scenarios or conditions for conducting better adhesive evaluations.

3.2.4.1. Burst pressure. A critical mechanical characteristic for many adhesive applications is the burst pressure, denoting the minimum pressure needed to cause tissue rupture or bursting when sealed with adhesives (Fig. 5I). This property gains significance, especially in scenarios where adhesives are utilized to prevent air leakage or bleeding in vital tissues like the lungs and heart.[165] For assessing burst pressure, fluids like air and water are introduced into an enclosed tissue structure to apply pressure, and the maximum pressure attained prior to tissue rupture is regarded as the burst pressure. While this method aids in comparing different adhesives and selecting the most suitable one for practical applications, it does not assess the adhesive's suitability for use in actual *in vivo* environments. Hence, further assessment of the corresponding adhesion performance by simulating the functional status of the ruptured tissue is necessary. For instance, adhesives designed for repairing damaged stomach tissue may undergo repeated mechanical deformation and corrosion from gastric acid, necessitating cyclic mechanical testing and acid corrosion resistance assessing to evaluate their susceptibility to failure in such environments.

3.2.4.2. Double cantilever beam (DCB). Assessing bond strength accurately is crucial when applying adhesive-bonded joints to load-bearing structures. One widely utilized technique for this purpose is the double cantilever beam (DCB) test, commonly employed to evaluate the fracture energy of bonded materials (Fig. 5J).[166] The critical fracture energy G_{IC} is determined by assessing the energy change associated with crack propagation using linear elastic fracture mechanics (LEFM).[176] Typically, when employing DCB to assess adhesive fracture energy, a softer, thin, flat metal DCB substrate is preferred as the adherend to enhance accuracy. This choice is made because an extremely hard (thick) metal substrate would hinder continuous crack growth in the soft adhesive.[177] The procedure involves inserting a tip wedge into the adhesion gap and then applying a load at its end to advance the wedge forward at a constant rate (typically 1 to 5 mm min^{-1}) until delamination crack growth increments measure 3 to 5 mm. The maximum load point on the load-displacement curve recorded continuously during the test indicates the adhesion strength. Moreover, techniques like modified beam theory (MBT), compliance calibration method (CC), and modified compliance calibration method (MCC) can be employed to further calculate the interlaminar fracture toughness of the adhesive. It is important to note that significant deformations of the adherend may lead to energy dissipation due to plastic deformation, potentially resulting in an overestimation of the fracture energy. To mitigate this issue, spring steel is often chosen as the adherend.[176]

4. Typical adhesion failure modes and design principles for tough adhesion

Adhesion failure is a complex phenomenon influenced by various factors, including polymer chemistry, surface topology, and mechanical forces.[39] Within a specific bonding interface, multiple elements come into play, such as the chemical properties of the bonding surface, the cohesion of the adhesive polymer, and the physical characteristics of the adhesive and

its interaction with the underlying substrate. Consequently, after successful anchoring of an adhesive to the adherend, subsequent failure may occur due to weak bonding between the substrate and the adhesive (interfacial failure), fracture of the adhesive material itself (cohesive failure), or a combination of both. Additionally, external factors, such as the nature of the adhered items, can also contribute to the failure process (Fig. 6).

4.1. Typical adhesion failure modes

The interfacial toughness for representative soft adhesives, including hydrogels and elastomers, has been assessed using a variety of experimental techniques. These methods encompass the lap shear, along with 90- and 180-degree peel tests as detailed in Section 3.[179] For instance, in the 90° peeling test, an adhesive tape with dimensions of thickness T, width W, and length L (where $L \gg W \gg T$), is adhered to a adherend, and introducing a detaching notch along the length direction of the interface (Fig. 6A). Subsequently, the detached part of the adhesive is peeled off the substrate while being pulled vertically away from it. As the peeling process stabilizes, the measured force reaches a plateau ($F_{plateau}$), and the interfacial toughness is calculated by dividing the plateau force $F_{plateau}$ by the width of the adhesive sheet W, expressed as $\Gamma_{inter} = F_{plateau}/W$.

If an adhesive is attached to the substrate through a sparse arrangement of weak physical cross-links, like hydrogen bonds and electrostatic interactions, the interfacial toughness might be lower, potentially leading to adhesive failure (Fig. 6B). Conversely, in cases where an adhesive with a conventional polymer network[37] forms strong bonds with the substrate, such as *via* covalent bonds, the interfacial toughness matches the adhesive's fracture toughness or intrinsic fracture energy Γ_0. This equivalence occurs because the adhesive's fracture toughness sets a maximum limit for the interfacial toughness, possibly resulting in cohesive failure (Fig. 6C).[178] Additionally, certain adhesives, like viscous hydrogels, which form solely through physical interactions without chemical cross-linking, may experience debonding due to a combination of adhesive failure and cohesive failure (Fig. 6D). Naturally, if the cohesion of the adherend is weaker than both the interfacial adhesion and the cohesive strength of the adhesive, the adherend may rupture when peeling force is applied (Fig. 6E).

4.2. Design principle for adhesives with tough adhesion

As mentioned above, when an adhesive bonds to an adherend surface *via* a weak and sparse physical cross-linking network, cracks tend to propagate easily along the adhesive-adherend interface, which will lead to diminished interfacial toughness

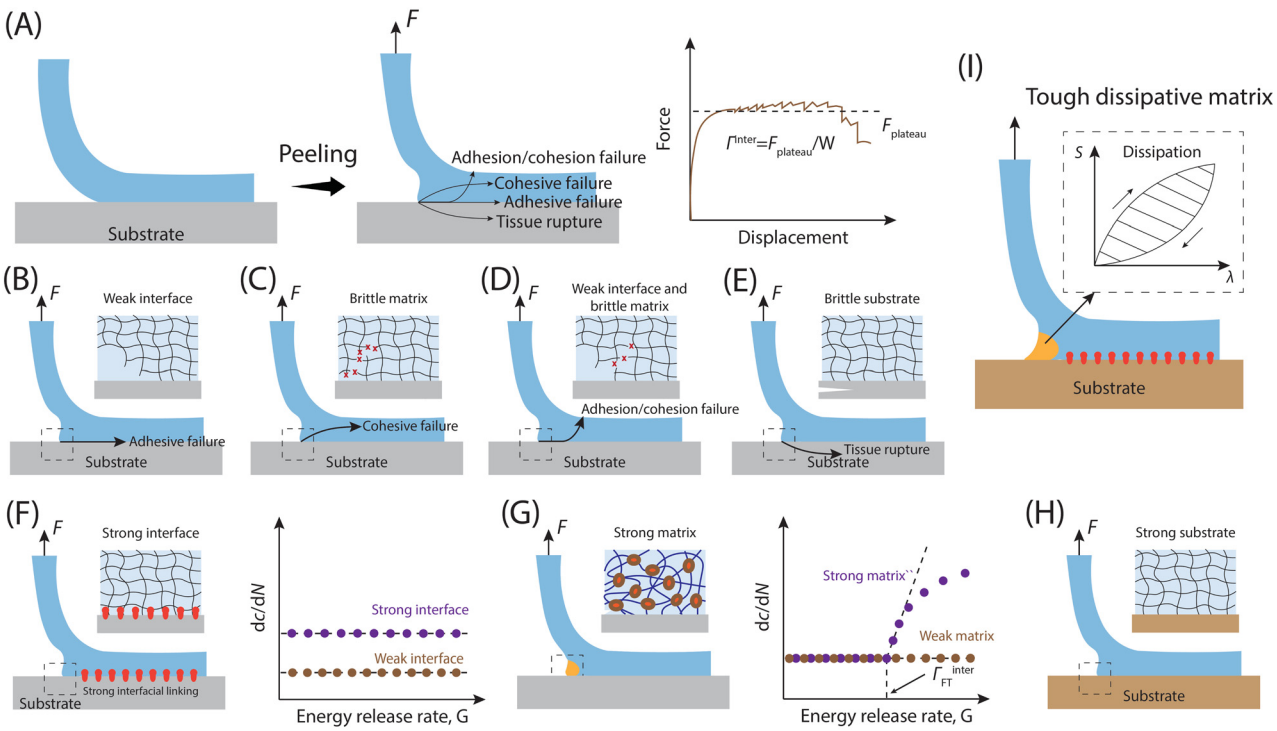

Fig. 6 Representative bonding failure modes of the adherent–adhesive interfaces. (A) The concept of interface toughness and the related testing process (90° peeling) for measuring interfacial toughness. F is the peeling force, $F_{plateau}$ represents the force during stable peeling stage, and W is the width of the sample. The corresponding interfacial toughness could be expressed as $\Gamma_{inter} = F_{plateau}/W$ based on the values of $F_{plateau}$ and W measured during the peeling process. (B)–(E) Different interfacial adhesion failure modes. (B) Adhesive failure. (C) Cohesive failure. (D) The combination of adhesive failure and cohesion failure. (E) Adherend rupture. (F)–(H) Strategies to address different modes of interface adhesion failure. (F) Creating strong interfacial bonds to prevent adhesive failure. (H) Improving the fracture toughness of adhesive matrices to avoid cohesive failure. (I) Utilizing robust substrates (adherends) to prevent substrate rupture. (I) Combining resilient dissipative adhesives, robust interfacial bonds and strong substrate results in durable interfacial adhesion. The factors contributing to the overall interfacial toughness, including strong interfacial bonds and mechanical dissipation within the process zone, are denoted as Γ_0^{inter} and Γ_D^{inter}, respectively. The total interfacial toughness of the tough adhesion is $\Gamma^{inter} = \Gamma_0^{inter} + \Gamma_D^{inter}$.[178]

(Fig. 6B). As a result, the effective design of resilient adhesive bonds requires the establishment of robust interfacial connections between the adhesive and the adhered substrates (Fig. 6F). This is achievable through means such as covalent bonds,[171,178,180,181] robust physical cross-links,[31,182,183] intermediary connector polymers,[13,184–186] and mechanical interlocking mechanisms.[187] Furthermore, considering that interfacial cracks may veer into the adhesive and lead to cohesive failure (Fig. 6C), it becomes imperative in adhesive design to enhance the fracture toughness of the adhesive matrices (Fig. 6G).[178] The strong cohesion of the adherend and its non-breakability also play an important role in constructing strong adhesion interface (Fig. 6H). In essence, the fundamental principle guiding the creation of adhesive systems with enhanced interfacial toughness involves the fusion of resilient adhesive matrices with robust interfacial connections.[178] When subjected to attempts to detach the adhesive from the substrate, the sturdy interfacial linkages serve to arrest the progression of interfacial cracks, thereby allowing the adhesive to form a region of substantial mechanical dissipation, known as the process zone (Fig. 6I). Mathematically, the overall interfacial toughness can be represented as: $\Gamma^{\text{inter}} = \Gamma_0^{\text{inter}} + \Gamma_D^{\text{inter}}$, where Γ^{inter} denotes the total interfacial toughness, Γ_0^{inter} signifies the intrinsic interfacial toughness stemming from robust interfacial linkages, and Γ_D^{inter} represents the contribution of mechanical dissipation within the process zone to the overall interfacial toughness.[171,178] To attain durable adhesion of synthetic adhesives across a wide array of substrate materials, encompassing metals, ceramics, glass, silicone, elastomers, hydrogels, and biological tissues.[37]

5. Biological adhesive interfaces

Exploring nature to uncover the mechanisms governing surface adhesion in biological organisms represents the most effective approach for designing and fabricating adhesive materials. Fig. 7 showcases selected examples of biological surfaces with distinctive adhesion properties, including superhydrophobic surfaces with high adhesion to liquid droplets, dry adhesion surfaces, wet adhesion surfaces and underwater adhesion surfaces. Notably, all these examples exhibit multiscale structures. Biomimetic investigations have revealed that the synergy between these unique multiscale structures and inherent material properties contributes to the observed adhesion and multifunctionality.[46,188]

5.1. Superwetting droplet adhesive surfaces

Micro- and nanostructures could not only help enhance surface's hydrophobicity but also play a pivotal role in surface adhesion. For instance, research has demonstrated that the water contact angle (WCA) on red rose petals is approximately 152°, however, water droplets would adhere to the petal surface even when inverted.[102] This unique combination of superhydrophobicity and high adhesion is referred to as the "rose petal effect."[204–207] The surface of rose petals is composed of dense micron-scale papillae arrays, which is considered the reason for the super-hydrophobic property. At the tips of the papillae are many nanoscale folding structures, also known as nano creases (Fig. 7A).[102,208] These nano creases are the key factor leading to the high adhesion properties of rose petals. Similarly, peanut leaves exhibit a comparable structure (Fig. 7A), resulting in a blend of super-hydrophobicity and high adhesion.[189,209]

Different from the above examples, Salvinia Molesta boasts a super-hydrophobic adhesive surface owing to the unique chemical composition of its microstructure. As illustrated in Fig. 7A, this surface features distinct pillar arrays, each measuring 2 mm in height and crowned with hairs, reminiscent of an eggbeater.[100,210] These millimeter-scale columnar structures are coated with a layer of plant wax, rendering them hydrophobic. Interestingly, this plant wax is present only on the surface of the columns, while the hairy structures at the top, resembling eggbeaters, are not covered with wax and thus exhibit hydrophilic properties.[211,212] Due to the combined effect of these two structures with differing wetting properties, the leaves of Salvinia can exhibit both super-hydrophobicity (due to the hydrophobic columnar structure) and high adhesion (due to the hydrophilic "eggbeater" top structures) to water droplets. Researchers refer to this phenomenon as the "Salvinia paradox."[100,213–215] The main reason why these surfaces show high adhesion to droplets is that the nanostructure on the top of the surface is chemically compatible with the droplets, enabling the Wenzel wetting model. Therefore, when it comes to the corresponding superliquid-repellent high-adhesion surface, we can achieve it by designing a combination of microstructures that are lyophobic and nanostructures that are lyophilic. The former can make the surface super-repellent to droplets, while the latter can provide strong adhesion for droplets.

5.2. Dry adhesives

In contrast to traditional pressure-sensitive tapes, biological dry adhesive pads offer robust yet reversible adhesion, coupled with exceptional durability and self-cleaning properties. Found in various creatures such as insects (Brachyponera), spiders, and lizards (geckos), these biological dry adhesive systems share similar hierarchical fibrillar structures (Fig. 7B). Typically, as the weight of an animal increases, the size of the contact units at the ends of the adhesive structures on its paws decreases.[216] This is because smaller adhesive units allow for a higher packing density of these contact units within a given area, thereby enhancing the overall adhesion force to support the animal's greater weight. Among these creatures, the gecko stands out as the "king of climbers", owing to its remarkable climbing ability facilitated by the micro- and nanoscale hierarchical adhesion structures on the sole of the foot.[14,139] The largest part in the hierarchy of adhesive structures is the millimeter-sized lamellae (1–2 mm in length, Fig. 7B), which are composed of numerous setae and are distributed across the gecko's foot. Therse millimeter-sized lamellae are easily compressible to establish contact with rough, bumpy surfaces. Typically, 15–20 lamellae cover the entire area of a single toe and are visible to the naked eye. The second level of hierarchy consists of setae, tiny hairy structures serving as the fundamental adhesive units. Setae are arrayed on the outer surface of

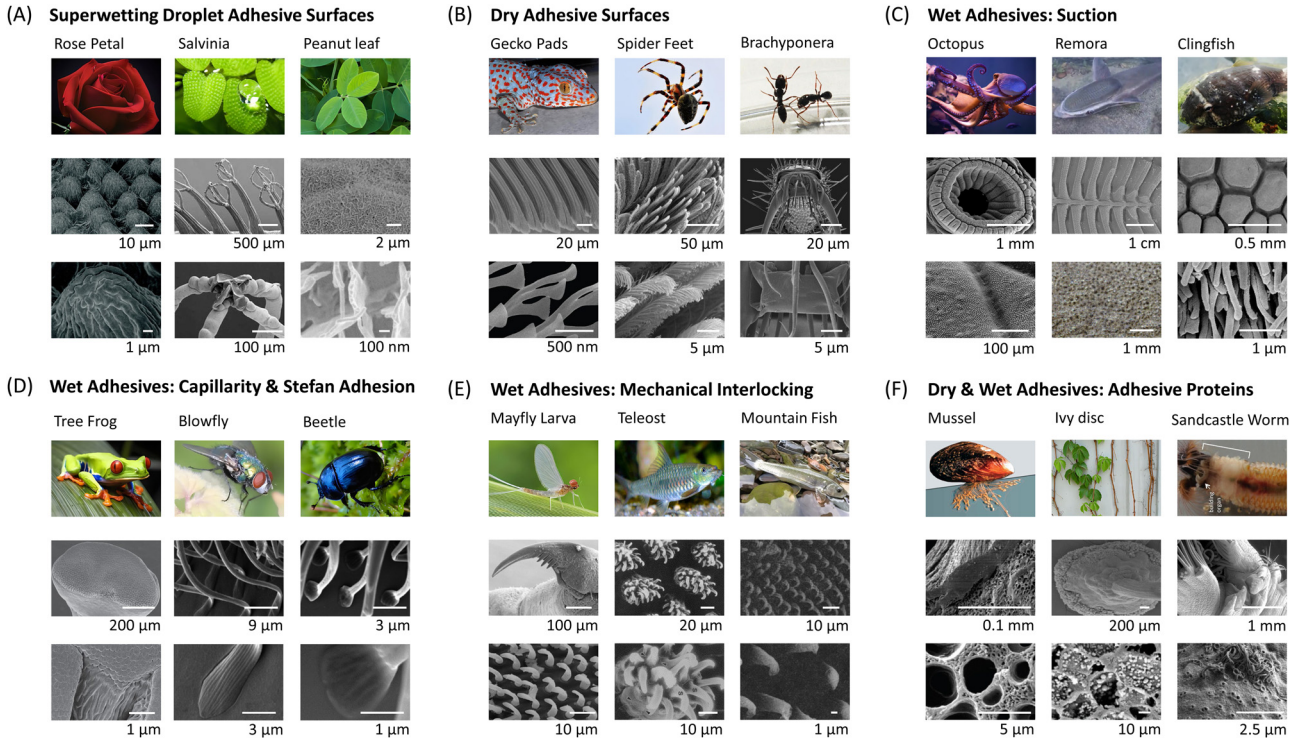

Fig. 7 Examples of biological surfaces showcasing exceptional adhesion properties and their intricate multiscale structures. (A) Superwetting droplet adhesive surfaces, including red rose petal,[102] Salvinia[100] and peanut leaf.[189] The micrographs of a red rose petal are reproduced with permission from ref. 102 Copyright 2008, American Chemical Society. The micrographs of a Salvinia molesta are reproduced with permission from ref. 100 Copyright 2010, Wiley-VCH. The micrographs of a peanut leaf are reproduced with permission from ref. 189 Copyright 2014, Wiley-VCH. (B) Dry adhesive surfaces, including gecko pad,[190] spider feet[191] and Brachyponera[192] (a kind of ant). The micrographs of a gecko pad are reproduced with permission from ref. 190 Copyright 2014, Annual Reviews Inc. The micrographs of spider feet are reproduced with permission from ref. 191 Copyright 2009, Taylor and Francis Ltd. The micrographs of an ant leg are reproduced with permission from ref. 192 Copyright 2017, King Saud University. (C) Wet adhesive surfaces based on suction, including octopus,[193] remora fish[194] and clingfish.[195] The micrographs of an octopus sucker are reproduced with permission from ref. 193 Copyright 2002, Oxford University Press. The micrographs of a remora fish are reproduced with permission from ref. 194 Copyright 2020, The Royal Society. The micrographs of a clingfish are reproduced with permission from ref. 195 Copyright 2013, The Royal Society. (D) Wet adhesive surfaces based on capillarity and Stefan adhesion, including tree frog,[196] blowfly[197] and beetle.[197] The micrographs of a tree frog pad are reproduced with permission from ref. 196 Copyright 2015, The Royal Society. The micrographs of the blowfly leg and beetle leg are reproduced with permission from ref. 197 Copyright 2013, Royal Society of Chemistry. (E) Wet adhesive surfaces based on mechanical interlocking and friction, including mayfly larva,[198] teleost,[199] and mountain fish.[200] The micrographs of a mayfly larva leg are reproduced with permission from ref. 198 Copyright 2010, Company of Biologists Ltd. The micrographs of the teleost jaw sheaths are reproduced with permission from ref. 199 Copyright 2006, Elsevier Ltd. The micrographs of the mountain fish's appendages are reproduced with permission from ref. 200 Copyright 2003, Indian Academy of Sciences. (F) Dry & wet adhesive surfaces based on adhesive proteins, including mussel,[201] ivy disc,[202] and sandcastle worm.[203] The micrographs of mussel byssus are reproduced with permission from ref. 201 Copyright 2011, Annual Reviews Inc. The micrographs of an ivy disc are reproduced with permission from ref. 202 Copyright 2020, Wiley-VCH. The micrographs of sandcastle worm building organ are reproduced with permission from ref. 203 Copyright 2017, Elsevier Ltd.

lamellae, which taper distally and measure 0.3–0.6 mm in width at the mesoscale. The setae are primarily composed of α- and β-keratin proteins and exhibiting a relatively uniform diameter (5–10 μm) and length (30–130 μm) distribution, usually extending outward at an angle of 30°. Each seta branches out at the tip, dividing into 100–1000 spatula.[40,217] The spatula is the smallest unit in the hierarchical adhesion structure of the gecko's foot and is the component that directly contacts the surface of the adherend. Similar to setae, the dimensions of the spatula are relatively uniform, with a thickness of approximately 10 nm, a length of about 500 nm, and a width of 200–300 nm. This uniformity allows them to be evenly distributed on a bristle without causing gradient differences. This meticulously structured hierarchy significantly amplifies the contact area between the gecko's pads and the surface, thus ensuring robust dry adhesion. The adhesive structures found on the feet of spiders and Brachyponera ants share a hierarchical organization akin to that of gecko feet, albeit with a notable distinction: the terminal attachment elements boast a significantly greater radius in both spiders and Brachyponera ants compared to geckos. The primary reason this type of biological surfaces achieves strong dry adhesion is the presence of numerous hierarchical bristle structures on the soles of their feet, which significantly increase the contact area with the adhered surface, thereby enhancing adhesion capability. Inspired by this phenomenon, we can design similar hierarchical micro-nano pillar structures on biomimetic artificial adhesive surfaces to increase the actual contact area between the adhesive and the adhered surface, thus improving adhesion performance.

5.3. Wet adhesives

Based on variations in biological wet adhesion mechanisms concerning surface structure and chemical composition, there are different types of wet-adhesive surfaces: wet adhesion based on suction, wet adhesion based on capillary force & Stefan adhesion, wet adhesion based on mechanical interlocking & friction, and wet adhesion based on adhesive proteins. It is important to recognize that in the intricate biological environment, multiple adhesion mechanisms often collaborate to achieve wet adhesion. For instance, in many fishes, underwater adhesion is achieved by combining the suction of adhesion discs with the friction provided by micro-nano structures on their surfaces. Consequently, investigating biological wet-adhesive surfaces and comprehending their inherent adhesion mechanisms can serve as valuable guidance for the design of artificial biomimetic wet-adhesive surfaces.

5.3.1. Wet adhesives surfaces based on suction. In aquatic environments such as oceans and rivers, numerous aquatic organisms can adhere to rocks or other surfaces by employing structures that create negative pressure (Fig. 7C). For instance, octopuses could effectively climb rocks and capture prey in the sea by utilizing suction generated through the suction cups on their tentacles.[193] The dense, hair-like arrangement of bristles covering the protruding surface of these suction cups enhances the sealing between the cups and the substrate, ensuring a dependable suction force.[19–21] Remoras are capable of adhering to the skin of other fishes by utilizing the adhesive disc located on the top of their head, enabling them to hitch a ride in the sea. This adhesion is facilitated by a set of parallel lamellae with spines present in the adhesive disk, which effectively heightens the friction between the adhesive disk and the substrate, consequently enhancing the suction force.[218–220] The surface of the adhesion disc in Clingfish is adorned with papillae, and these papillae are also densely interspersed with graded villi, which serve to enhance the sealing between the adhesion disc and the irregular surface through friction, thereby ensuring a sustained suction effect.[195,221,222] The suckermouth catfish possesses a sucker mouth with papillae covered in spines, where the mastoid structure creates negative pressure, and the spines aid in enhancing friction on the adherent substrate, thus improving the sealing capability.[223–226] This attribute grants them the capability to attach to aquarium walls using their suckermouths, while also enabling them to scrape off food from the surfaces. Like suckermouth catfish, the golden algae eater achieves adhesion to aquatic plants and rocks through its sucker mouth, and this sealing is accomplished by the presence of micron-sized papillae on the sucker mouth. The loach, on the other hand, relies on the lips on its ventral side, as well as its pectoral and pelvic fins, to generate the suction force for adhesion.[227] Their lips have polygonal spines, and their pectoral and pelvic fins possess needle-like spines, which together seal the edges of the sucker. Despite the evident morphological variations among these biological wet-adhesion structures that generate suction, they all share adhesive elements capable of producing negative pressure and micro-nano structures that facilitate effective sealing. Therefore, when designing biomimetic artificial adhesives based on suction cup structures, we must also consider the structure (ciliary structure) used to maintain the sealing performance of the suction cup.

5.3.2. Wet adhesives surfaces based on capillarity and Stefan adhesion. In nature, there are also numerous organisms possessing adhesive pads that are covered with mucus, facilitating wet adhesion through the formation of liquid bridges and the utilization of capillary force and Stefan action (Fig. 7D).[228–231] For instance, tree frogs exhibit the ability to crawl on both trees and wet surfaces, which is attributed to the presence of polygonal epidermal protrusions on their toe pads, accompanied by nanopillars with concave ends. This hierarchical structure of tree frogs effectively adapts to various irregular surfaces of substrates, and the channels in their feet promote the spreading of mucus and the expulsion of water, enhancing the adhesive properties on the adherent surface.[18,232–234] In addition to tree frogs, certain insects also utilize adhesive pads and secretions to achieve wet adhesion. Typical examples include blowflies and beetles, which possess hair-like structures on their feet. Although they have hierarchical fibrillar structures similar to geckos, beetles and flies increase adhesion by secreting liquids at the contacting interface, rather than the dry adhesion produced by geckos. A significant indicator is observed when blowflies and beetles move away, as they leave behind footprints marked with secretions on the contact surface. Their adhesion is facilitated by the surface tension of these secretions present on their feet.[235] This type of wet adhesive surface offers valuable design inspiration for developing biomimetic artificial adhesives suitable for humid environments. For example, gecko-like artificial adhesives often struggle to maintain effective adhesion in such conditions. However, by mimicking the polygonal structure of a tree frog's foot, we can utilize the channels between these structures to drain excess water from the contact interface. Additionally, the water film retained in these channels can provide extra capillary adhesion, enhancing the biomimetic artificial adhesive's performance.

5.3.3. Wet adhesives surfaces based on mechanical interlocking and friction. Certain organisms, like mayfly larvae, teleost, and mountain fish, achieve wet adhesion by enhancing the mechanical interlocking and friction effects of their surfaces with irregular substrates (Fig. 7E). Mayfly larvae, for instance, can achieve stable and efficient underwater adhesion through various adhesion structures, including claws on the front legs, bristle pads on the gill flaps, and spines on the abdomen. These adaptations enable them to thrive in still water or even turbulent rapids.[198,236,237] Gorb *et al.* made an intriguing discovery in 2014, biofilms on mayfly larva increase friction between the larvae and smooth substrates, but decrease friction on rough substrates.[22] This finding indicates that the friction-enhancing effect of the mayfly larval biofilm differs from the mechanism of friction increase caused by micro-nano structures. The underwater adhesion of teleost is closely linked to the presence of hooked nodules on their mandibular sheaths, enabling mechanical interlocking with substrates.[199] A similar mechanism is also observed in mountain fish, where long hooks on their appendages mechanically interlock with irregular surfaces.[200] This adhesion phenomenon offers new inspiration for the development of biomimetic artificial adhesives. Previously,

researchers have focused on optimizing the structure and size (such as in gecko-like dry adhesives) to enhance adhesion performance. However, biological surfaces frequently employ multiple adhesion mechanisms. Incorporating mechanical interlocking and friction-enhancing microstructures can be applied to various other biomimetic adhesive surfaces (*e.g.*, gecko-inspired, tree frog-inspired, octopus-inspired). This adhesion mechanism is versatile and not restricted by environmental conditions or application scenarios, making it an effective supplementary adhesion strategy.

5.4. Adhesives surfaces based on adhesive proteins

Certain organisms employ secreted adhesion proteins to achieve enduring adhesion, facilitated by various chemical interactions like complexation, hydrogen bonding and chemical bonding with the adhered surface (Fig. 7F). For instance, sandcastle worms utilize their secreted adhesion proteins containing polyelectrolyte components to bind sand grains together, forming shells in water.[203,238] Caddisfly larvae employ their secreted filamentous proteins to bind glass beads together underwater.[239] Similarly, in the realm of plants, ivy is particularly noteworthy for its exceptional adhesion capabilities, allowing it to cling to diverse building walls. Ivy's adhesive pads primarily adhere to the substrate through chemical bonds formed by the secretion liquid from epidermal cells, which is composed by tannin substances and various acidic viscoelastic polysaccharides.[202] The mature adhesive pads (capable of secreting viscous fluid) exhibit remarkable adhesion strength, capable of supporting the weight of stems, leaves, branches, and tendrils for ivy, which surpass their weight by 260 times.[240] Among the organisms that achieve stable adhesion by secreting adhesive proteins, mussels have garnered significant attention in the study of their unique underwater adhesion mechanism. Mussels possess the ability to produce a considerable number of adhesion plaques using their own secreted adhesion proteins, which are crucial for achieving long-lasting adhesion to underwater rocks.[241–244] Upon analyzing the chemical composition of these proteins, researchers observed significant quantities of hydroxyproline and dopamine, which contain catechol functional groups.[30,245,246] These catechol functional groups can be effectively anchored onto diverse surfaces through complexation and hydrogen bonding, making them widely utilized for surface modification of materials (Fig. 1).[30,31,247–251] The discovery of the mussel chemical adhesion mechanism (dopamine adhesion group) effectively addresses the limitations of existing biomimetic artificial adhesives that rely solely on structural adhesion. Previously, structural biomimetic adhesives achieved adhesion through various physical interactions. The mussel chemical adhesion mechanism, however, introduces the potential for adhesion based on chemical bonds, enabling underwater adhesion without the need for suction cup structures.

6. General biomimetic principles and manufacturing technology for artificial adhesives

A wide spectrum of living organisms, ranging from microscopic bacteria and fungi to larger marine algae, invertebrates, insects, frogs, and even terrestrial vertebrates like geckos, utilize specialized adhesive mechanisms and secretions for temporary or permanent surface attachment (the representative examples have been illustrated in Section 5). These biological adhesives exhibit diverse structures and functionalities, often operating in ways distinct from traditional synthetic adhesives. The diversity and exceptional performance of these biological adhesives suggest promising avenues for the development of artificial adhesives that deviate significantly from current standards. In this section, we will introduce the general biomimetic principles behind artificial adhesives inspired by nature and outline the primary methods employed in the fabrication of these biomimetic adhesives.

6.1. General approaches for constructing biomimetic materials

The effective translation of biomimetic concepts from natural examples to practical engineering materials involves a structured process, delineated into four essential steps, as illustrated in Fig. 8. Each of these steps must be meticulously addressed to achieve a successful transfer of technology. It is worth noting that this process is not exclusive to biomimetic adhesives (Fig. 8A and B); rather, it can be extended to various other biomimetic materials as well, as the fundamental concept remains unchanged.

Identifying a high-performance natural prototype. At this stage, different target organisms that exhibit the desired structures and/or functions serve as the selection range to determine the best prototype. This biological prototype could provide us with appropriate raw materials and the corresponding structural design required for the subsequent biomimetic process. Particular attention should be given to the structure–property–function relationship, especially in cases where biomaterials serve multiple functions, as this enables the identification of the most suitable biomimetic prototypes.

Extracting essential mechanisms, structures, and design principles. During this phase, our focus lies on grasping the underlying principles and concepts of natural models and systems, rather than merely duplicating their structures in artificial materials. It is crucial to identify and comprehend the inherent connection between the properties of natural materials and their appealing traits. By distilling these insights from natural models, we can effectively incorporate them into engineering designs. Nevertheless, this process can prove arduous and challenging, mainly due to the multi-scale complexity and layered structures often found in natural materials.

Designing biomimetic structures. In this phase, the primary objective is to integrate the inherent principles and concepts from natural prototypes/systems into the design of engineering materials. This involves carefully choosing suitable raw materials, determining synthesis methods for biomimetic structures, and optimizing the corresponding bioinspired design principles and synthesis pathways, often leveraging computer modeling techniques to aid in the process.

Manufacturing biomimetic materials. Building upon the progress made in the initial three stages, this stage involves the actual fabrication of artificial biomimetic materials.

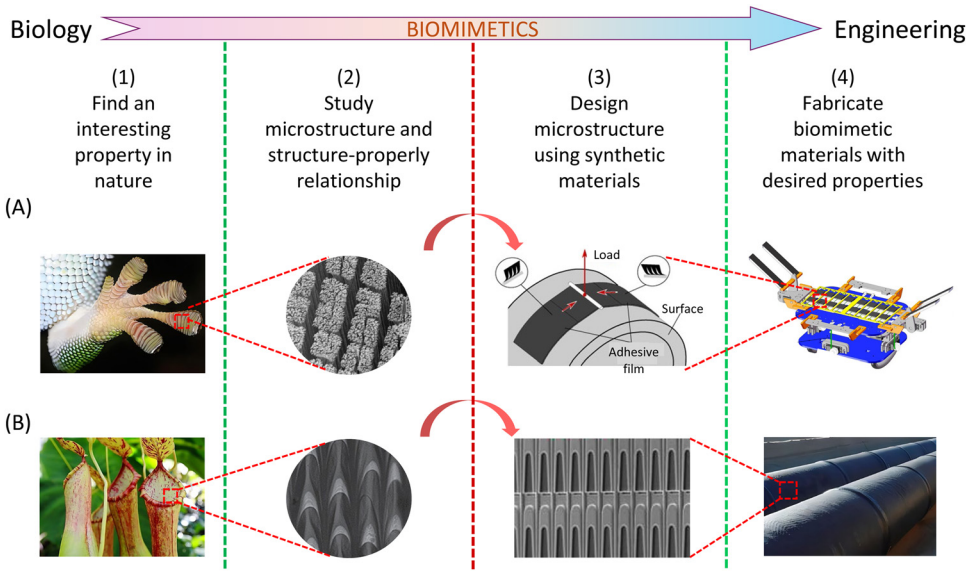

Fig. 8 From intriguing findings in nature examples to the development of advanced engineering materials and devices. (A) Transitioning from studying the gecko feet to creating space junk grippers. The pictures are reproduced with permission from ref. 190 Copyright 2014, Annual Reviews Inc., and ref. 252 Copyright 2017, AAAS. (B) Utilizing insights from Nepenthes alata to design continuous directional water transport tubes. The pictures are reproduced with permission from ref. 99 Copyright 2016, Nature Publishing Group.

However, when using raw materials with chemical compositions similar to biological prototypes for the synthesis of artificial biomimetic materials, challenges are often encountered in achieving properties comparable to their natural counterparts. This is due to technical constraints during the preparation process, making it difficult to precisely replicate the intricate natural structures. Despite this, the researchers managed to produce interesting products with properties similar to those of natural biological prototypes.

6.2. Typical manufacturing technology for constructing biomimetic adhesives

Adhesion on biological surfaces can be categorized primarily into structural adhesion, which relies on surface micro-nano structures, and chemical component adhesion, based on biological adhesion proteins. To be more specific, the micro-nano structure primarily enhances adhesion by increasing the contact area between the biological surface and the substrate, as seen in the dry adhesion of gecko feet; or by providing additional forces, like the extra friction from Mayfly Larva hooks. Chemical component adhesion involves adhesive proteins, such as dopamine molecules, which achieve strong adhesion to various surfaces through hydrogen bonds, supramolecular effects, and dynamic chemical bonds, *etc.* While most biological surfaces rely on a primary adhesion mechanism, artificial bio-inspired adhesives can effectively combine the strengths of both structural and chemical adhesion, resulting in advanced adhesives that benefit from the synergistic effects of these two mechanisms. In this part, we summarize the corresponding biomimetic surface construction technologies based on these two adhesion mechanisms respectively.

6.2.1. Manufacturing technologies for building micro- and nanostructures. Structural adhesion involves constructing the necessary micro-nano topography on the adhesive surface using advanced manufacturing techniques such as 3D printing, lithography (photolithography, imprint lithography, and colloidal lithography), electrochemistry, microfluidics, soft replication, etching, chemical vapor deposition (CVD), *etc.* (Fig. 9). Table 3 summarizes the working features of these technologies, along with the morphology of micro-nano structures suitable for construction, such as pillars with various tips (*e.g.*, flat, mushroom, polygon, sucker, spine, spatula tips, *etc.*), and other complex 3D structures.

6.2.2. Technologies for introducing functional groups with adhesion properties. The chemical components adhesion involves incorporating catechol and its derivatives (including dopamine, dopa, norepinephrine, gallic acid, and tannic acid) into the polymer chain through self-polymerization, copolymerization or post-modification to achieve the desired adhesion properties (Fig. 10).

Drawing inspiration from the adhesive proteins found in mussels, researchers have explored the use of dopamine in the creation of a novel adhesive material known as polydopamine (PDA). The PDA adhesive has garnered increasing interest due to its simplicity and versatility.[31,41] However, despite its wide-ranging applicability, the exact polymerization mechanism of PDA remains a subject of debate, primarily due to the complexity of the redox processes and reaction intermediates involved during polymerization. This discussion aims to briefly outline the formation mechanisms and structures of PDA, as depicted in Fig. 10A. The generation of PDA typically commences with the oxidation of dopamine in alkaline solutions in the presence of dissolved oxygen. This initial oxidation leads to the transformation of the catechol groups of dopamine into quinone. Subsequently, dopaquinone undergoes intramolecular cyclization, reversible oxidation, intramolecular rearrangement, and

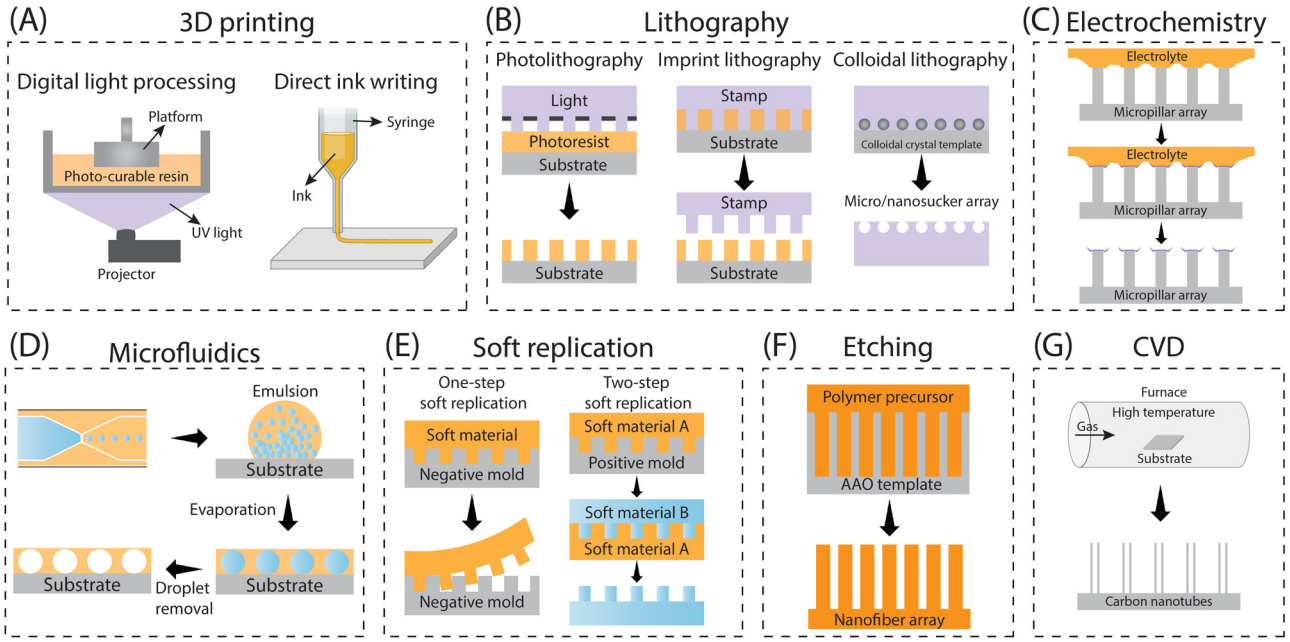

Fig. 9 Schematics of typical fabrication methods for artificial adhesives' micro- and nanostructures. (A) 3D printing. (B) Lithography, including photolithography, imprint lithography and colloidal lithography. (C) Electrochemistry. (D) Microfluidics. (E) Soft replication, including one-step soft replication and two-step soft replication. (F) Etching. (G) Chemical vapor deposition (CVD).

further interactions such as charge transfer, hydrogen bonding, and π–π interactions, ultimately resulting in the formation of the proposed PDA structures.[282–287] Additionally, it has been observed that dopamine can undergo oxidative self-polymerization under acidic conditions, employing similar mechanisms to those observed in alkaline environments.[288,289] The mechanism, influencing factors, and process of dopamine self-polymerization have been extensively discussed in the literature, and interested readers can find detailed explanations elsewhere.[5,31,44,290–292] The self-polymerization of dopamine holds particular relevance for the functionalization of various polymers, as it allows for the unification of all component surfaces through a convenient one-step process. Moreover, PDA adhesives have the capability to undergo further reactions with amine and thiolate groups *via* Michael addition reactions, leading to the formation of multifunctional surfaces. Apart from dopamine, its derivatives including dopa, norepinephrine, gallic acid, and tannic acid are also utilized for modifying polymers through self-polymerization techniques.[181,292–299]

Apart from the self-polymerization process, dopamine, and its derivatives can also be incorporated into various polymers through covalent bonds. Various methods are available for modifying polymers to include catechol or gallol groups since natural polymers typically contain numerous reactive functional groups such as $–NH_2$, –COOH, and –OH. Common modification approaches encompass 1-ethyl-3-(3-dimethylaminopropyl)carbodiimide/*N*-hydroxysuccinimide (EDC/NHS) coupling chemistry, Schiff-base chemistry, and the free radical-induced grafting method using the ascorbic acid/H_2O_2 redox system, *etc.* (Fig. 10B–D).

The coupling chemistry involving 1-ethyl-3-(3-dimethylaminopropyl)carbodiimide (EDC) and *N*-hydroxysuccinimide (NHS) stands out as one of the most commonly utilized methods for biomacromolecule functionalization (Fig. 10B). This method facilitates the efficient formation of amide linkages between $–NH_2$ and –COOH groups under acidic conditions.[181,300,301] EDC serves as a water-soluble activation agent for –COOH groups, generating the *O*-acylisourea intermediate, albeit its stability in aqueous solutions is relatively weak. However, the inclusion of NHS or *N*-hydroxysulfosuccinimide (sulfo-NHS) stabilizes the *O*-acylisourea by converting it into an ester (more stable), which could help to enhance the conversion efficiency of the target reaction. The majority of natural polymers feature abundant amino and carboxyl groups. Consequently, dopamine and related chemicals can readily attach to natural polymers (hyaluronic acid, alginate, cellulose, *etc.*) *via* EDC/NHS coupling chemistry to produce catechol- or gallol-polymer conjugates.[260,302–306]

Schiff-base chemistry provides another effective approach for the synthesis of catechol- or gallol-functionalized polymers (Fig. 10C). This method entails the reaction of amino and aldehyde groups under mild conditions, resulting in the formation of a C=N double bond.[307,308] Importantly, the oxidation of polymers using $NaIO_4$ can yield dialdehyde polymers capable of reacting with dopamine and its amino derivatives *via* Schiff-base chemistry to produce catechol- or gallol-functionalized polymers. For example, the dialdehyde groups generated from oxidized natural polymers (carboxymethylcellulose, hyaluronic acid and dextran) would undergo Schiff-base chemistry with the amino units of dopamine, leading to the formation of dopamine-polymer conjugates.[309,310]

The free radical-induced grafting approach, utilizing the ascorbic acid/H_2O_2 redox system, is also utilized for the synthesis of catechol- or gallol-polymer conjugates.[311] This method

Table 3 Typical fabrication methods for artificial adhesives' micro- and nanostructures

Methods	Working features	Feasible structures	Accuracy	Ref.
3D printing	Effectively and precisely control the geometrical parameters of printed structures	All types of structures discussed above (flat, mushroom, polygon, sucker, spine, spatula tips), regardless of a single layer or multiple layers, as well as other complex 3D structures (eggbeater)	Depending on the 3D printer used (*e.g.* Micro-arch S230A can achieve a precision with 2 microns)	7, 8, 13, 210 and 253–262
Photolithography	Precisely tailoring symmetric geometrical parameters of micro-structures such as diameter, height, pitch and thickness, but completely failing to sculpture asymmetric parameters involving tilting angle	Straight pillars with shaped tips of flat, sucker, polygon	Can achieve the construction of nanoscale structures (usually hundreds of nanometers)	57 and 263–265
Imprint lithography	Able to construct microstructures with a certain taper	Straight pillars with taper	Nanoscale structures, overlay accuracy up to 2.4 nm/3.2 nm	266
Colloidal lithography	Construct structures that are controlled by the spherical shapes of the particles in colloids	Spherical cavity structure	Nanoscale structures, usually higher than 100 nm	267–269
Electrochemistry	Solid/liquid/gas tri-phase interfaces as templates	Used to construct secondary structures on micron pillars whose shape depends on the three-phase contact interface	Nanowires higher than 50 nm	270 and 271
Microfluidics	With the aid of a capillary microfluidic device, a well-dispersed emulsion containing closely packed sacrificial droplets was created and subsequently applied onto a flat surface. Following the evaporation and elimination of the sacrificial droplets, a surface with concave cavities was effectively engineered	Spherical cavity structure	Nano pores with a diameter of around 200 nm	156 and 272–274
Template replication	Two methods are available for soft replication, depending on the template type: one involves utilizing a negative structured template for direct replication (1 step), while the other entails using a positive structured template (desired structure) for replication (2 steps)	Symmetric, asymmetric and anisotropic pillars with flat, mushroom, polygon, sucker, spine, spatula tips, *etc.*	Nanoscale structures, usually higher than 400 nm	258 and 275–278
Etching	Anodic aluminum oxide (AAO) with nanopores as templates	Straight pillars with flat tips	Nanoscale structures, usually higher than 500 nm	279 and 280
Chemical vapor deposition	Could only build carbon nanotube-based adhesives.	Straight carbon nanotube pillars	Carbon nanotubes with a diameter of several nanometers	281

represents a simple, cost-effective, and environmentally friendly strategy for producing such conjugates. Traditionally, it was believed that the hydroxyl radical ($^{\bullet}OH$) played a crucial role in this process.[312] However, recent electron paramagnetic resonance measurements have revealed that it is actually the ascorbate radical ($As^{\bullet-}$) that drives the free radical-induced grafting, rather than $^{\bullet}OH$.[313] A typical mechanism of this approach is illustrated in Fig. 10D, depicting the preparation of caffeic acid-chitosan conjugate. Ascorbic acid, a water-soluble compound containing two ionizable -OH groups, can give rise to ascorbate monoanion (AsH^{-}), which further ionizes into ascorbate dianion (As^{2-}). AsH^{-} is the predominant species under physiological pH conditions. It's notable that AsH^{-} acts as a potent reductant, producing $As^{\bullet-}$ through the one-electron oxidation reaction. Subsequently, the $As^{\bullet-}$ radical would lose another electron, resulting in the generation of dehydroascorbic acid. H_2O_2 facilitates the oxidation of ascorbic acid, thereby generating more $As^{\bullet-}$ radicals. These radicals are capable of attacking H atoms within chitosan, leading to the formation of chitosan macroradicals, which could react with caffeic acid to produce catechol-chitosan conjugates. This radical-induced grafting technique could also be extended to incorporate tannic acid, gallic acid and related chemicals onto polymers, yielding gallol-polymer conjugates possessing antioxidant properties.[314–316]

7. Bioinspired artificial adhesives

Drawing from the synthesis methods outlined in Section 6, a considerable array of biomimetic artificial adhesives have been engineered, leveraging both surface micro-nano structures and/or chemical components to achieve adhesion. In this section, we delve into the development of biomimetic artificial adhesives inspired by various biological adhesion mechanisms. This includes structural biomimetic adhesives, such as those mimicking gecko bristle arrays, treefrog polygonal arrays,

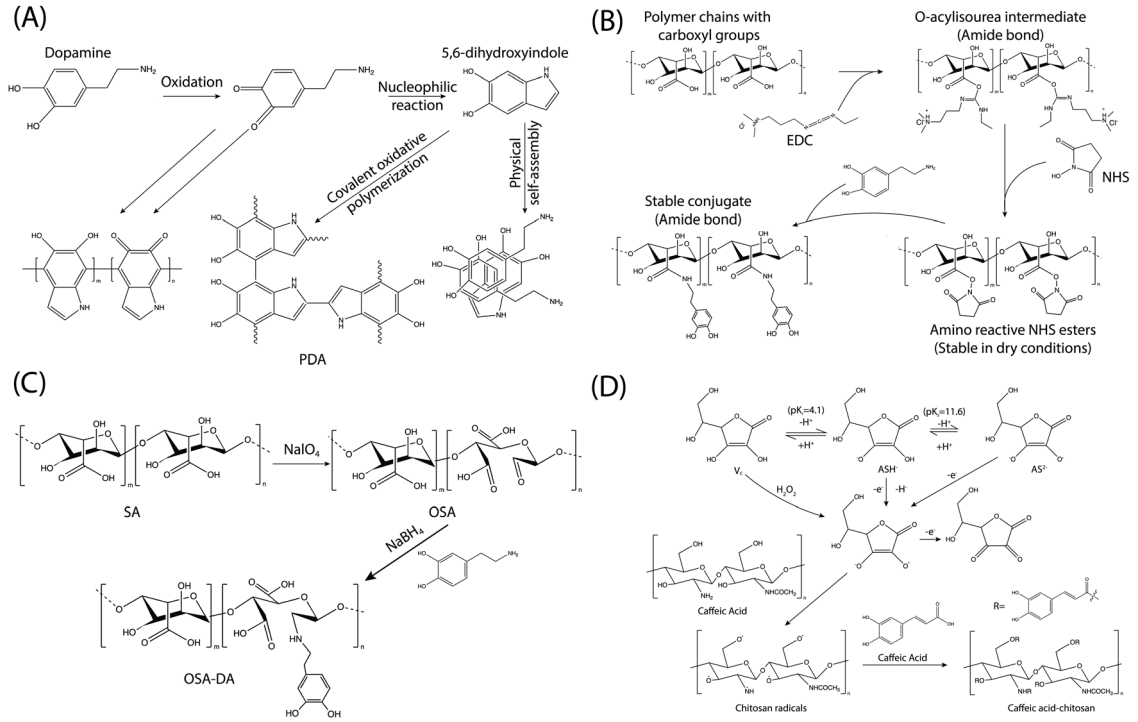

Fig. 10 Schematics of typical modification methods for incorporating catechol and its derivatives into polymers. (A) Self-polymerization of dopamine. (B) 1-Ethyl-3-(3-dimethylaminopropyl) carbodiimide/*N*-hydroxysuccinimide (EDC/NHS) coupling chemistry. (C) Schiff-base chemistry. (D) The free radical-induced grafting method using the ascorbic acid/H_2O_2 redox system.

octopus suckers, and other organisms' microscale hook arrays *etc.* Additionally, chemically biomimetic adhesives featuring specific chemical functional groups inspired by mussels will also be discussed.

7.1. Structural biomimetic adhesives

In recent decades, numerous bio-inspired artificial structural adhesives have been engineered to replicate the remarkable adhesive capabilities observed in nature, including those found in gecko pads, tree frog pads, octopus suckers, and other adhesive structures in various organisms (Fig. 11). While these artificial adhesives have achieved significant interfacial adhesive strength, they frequently exhibit subpar adhesion performance in challenging environments, such as dusty or rough surfaces.[278] In this part, we will explore the research advancements in biomimetic adhesive surfaces inspired by diverse adhesion structures.

7.1.1. Gecko-inspired setae arrays. Gecko-inspired setae arrays serve as a prime example of dry adhesives engineered for solid–solid contact. This arrangement fosters direct interaction between two solid interfaces, triggering the generation of van der Waals forces resulting from molecular interactions between adjacent molecules. These forces play a pivotal role in facilitating normal adhesion, thereby allowing artificial adhesives to achieve effective adherence. Notably, a uniform stress distribution contributes to robust adhesion, whereas stress concentration can lead to the formation of interfacial cracks, potentially propagating throughout the entire contact interface. Hence, achieving a large contact area and uniform stress distribution through meticulous structural and size design enhances the adhesion strength of gecko-inspired adhesive surfaces. Early explorations in this domain revealed a consistent design trajectory aimed at emulating the geometric characteristics of gecko toe pad structures (Fig. 12). Broadly, this evolution can be delineated into five distinct stages: (i) fabrication of freestanding vertically aligned micro- and nanofiber arrays (Fig. 12A); (ii) diversification of tip shapes (Fig. 12B); (iii) variation in fibril stem shapes (Fig. 12C); (iv) incorporation of anisotropic geometries such as angled fibril stems, sloping tips, or a combination of both (Fig. 12D); (v) establishment of hierarchical structures (Fig. 12E).

To investigate the impact of structure on gecko-inspired adhesives, Campo *et al.* employed ink printing curing to produce various vertical arrays with distinct geometries such as flat, spherical, flat with rounded edges, spatula, mushroom, and concave tips.[317] Their study revealed that arrays featuring mushroom and spatula tips exhibited significantly stronger adhesion compared to the control group with other tip shapes. Similarly, Xue *et al.* reached a comparable conclusion, noting that vertical arrays with hemispherical tips, when using rigid polymers, lacked detectable adhesion, whereas arrays with mushroom tips displayed adhesive properties.[318] This improved adhesion of mushroom-tipped vertical arrays is attributed to the umbrella-capped structure, which effectively mitigates stress concentration, thereby impeding crack formation and propagation across contact interfaces.[319] Furthermore, this umbrella-capped design also demonstrates greater resilience to dust particles and surface defects, enhancing adaptation to substrate roughness

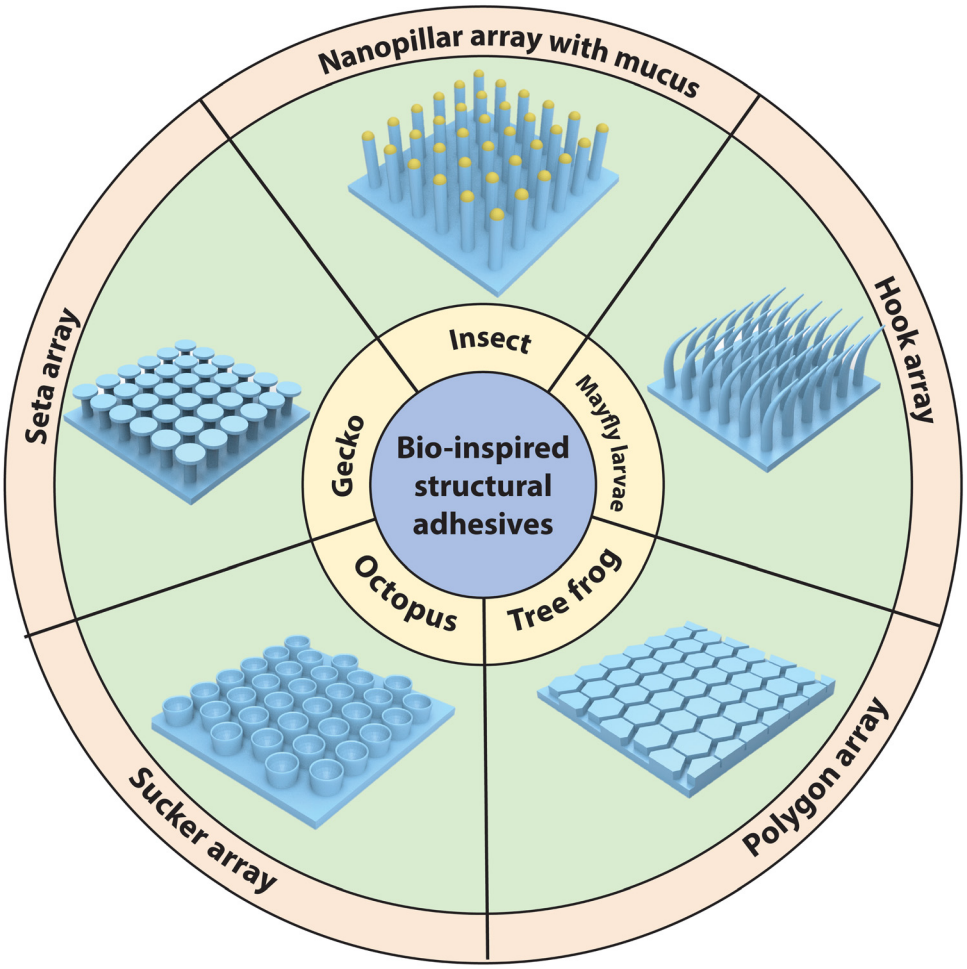

Fig. 11 Structural adhesive surfaces inspired by nature's designs at micro- and nanoscales comprise a variety of forms. Such as the mushroom array inspired by geckos, the sucker array modeled after octopuses, the nanopillar array with surface mucus inspired by insects, the polygon patterns mimicking tree frogs, and the hook array inspired by mayfly larvae.

and ensuring conformal contact formation.[319] Consequently, to find the best adhesion shape parameter, Carbone *et al.* systematically studied geometric parameters of the umbrella cap, particularly focusing on the ratio (R_e/R_i) between cap radius (R_e) and pillar radius (R_i), and the ratio (s/R_i) between pillar thickness and radius to optimize the mushroom tips.[48] And they found that when s/R_i falls within the range of 0.2–0.3, and R_e/R_i exceeds 2, the optimal performance could be attained.

On the other hand, the JKR model indicates that adhesive strength decreases as the contact radius increases, providing a fundamental framework for designing gecko-inspired adhesive surfaces. In a study by Greiner *et al.*, the adhesion properties of fibers with varying radii were systematically examined, revealing a significant increase in interfacial adhesion as the fiber radius decreased, aligning with the predictions of the JKR model.[320] Additionally, ultra-thin pillars, often at the nanoscale, may exhibit another advantage that they are less susceptible to disturbances at the contact interfaces.[321,322] Consequently, gecko-inspired setae arrays featuring nanoscale pillars demonstrate greater tolerance to dust particles and surface defects, showcasing superior adaptability. Moreover, the gecko-inspired micro- and nanopillars' adhesion performance is highly related to their aspect ratios.[323] Aksak *et al.* revealed that decreasing aspect ratios significantly enhances structural stiffness through finite element simulation.[324] However, this increase in stiffness may compromise conformal contact with the substrate, diminishing adaptability to rough surfaces. This observation may explain the rarity of low aspect ratios in natural dry adhesion systems, as they are not typically the desired design objective for most adhesive systems. Conversely, research has indicated that higher aspect ratios can bolster interfacial adhesion.[325] Nonetheless, it is important to note that slender fibers may easily adhere to nearby fibers due to interfacial interaction forces, leading to adhesion failure.[326] Additionally, drawing inspiration from the inclined setae of geckos, artificial adhesives featuring inclined arrays and inclined tips both exhibit notable friction and adhesion anisotropy, facilitating an easy transition between attachment and detachment.[40,327] Furthermore, several studies have showcased that hierarchical structures can reduce adhesive stiffness, enabling conformal contact with rough surfaces and enhancing adaptability to surface roughness.[11]

7.1.2. Tree frog-inspired polygonal patterns. The geometric configuration of polygonal micropillars found on the toes of

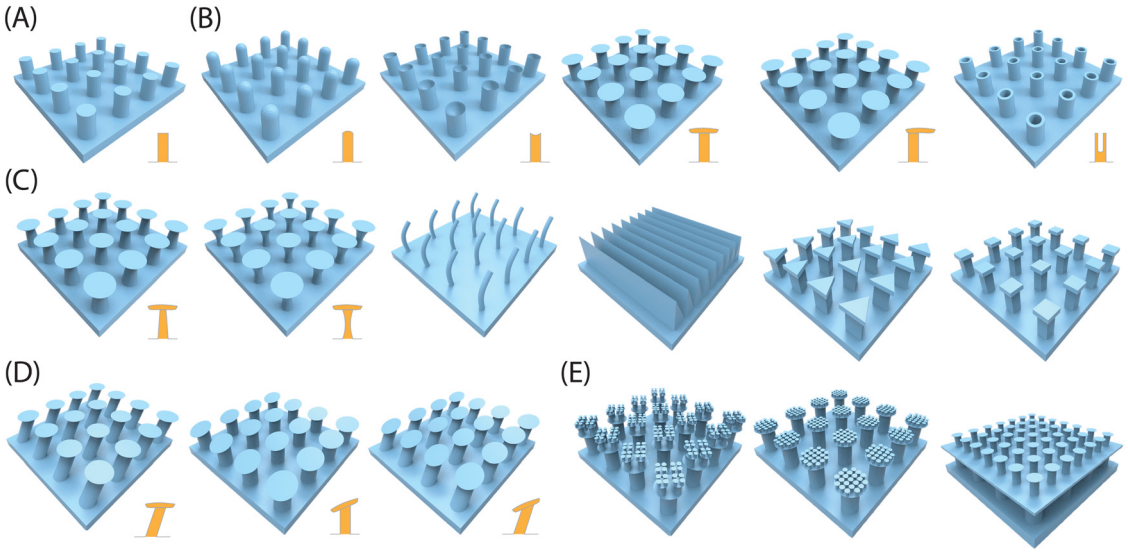

Fig. 12 The development of gecko-inspired dry adhesive structures. (A) Vertically aligned micro- and nanofibers. (B) Tips with different shapes. (C) Fibril stems with different shapes. (D) Anisotropic structures, including fibril sloping stems, sloping tips, and a combination of both. (E) Hierarchical structures.

tree frogs equips them to thrive in humid environments. In addition to the van der Waals forces arising from direct contact between these micropillars and solid surfaces, there also exists wet adhesion, which primarily stems from capillary forces generated by liquid bridges formed between the micropillars and contacting surfaces. As described in eqn (9), the magnitude of capillary force depends heavily on liquid film's thickness, denoted as h. The overall morphology and uniformity of the liquid film are largely affected by the configuration of the polygonal micropillar array, as this arrangement dictates the flow and drainage of liquid between the micropillars. Consequently, optimizing the geometric structures of tree frog-inspired adhesives is pivotal for enhancing their ability to adhere in wet conditions. Research on biomimetic wet adhesives for imitating tree frog pads mainly involves the shape, size and hierarchical structure of micropillars (Fig. 13).

Due to the diverse polygonal micropillars observed in tree frog toe pads, Chen *et al.* conducted a systematic comparison of friction forces across seven different surface patterns, as depicted in Fig. 13A, determining that hexagonal micropillars exhibited superior adhesion performance.[53] This superiority stems from the micropillar structure directly influencing the drainage capacity of the channels, which significantly impacts the flow dynamics of liquid within them. Hexagonal channels demonstrate improved drainage, preventing liquid accumulation that could otherwise flush into contact interfaces, thereby reducing the thickness of the liquid film and enhancing friction and adhesion. Furthermore, Iturri *et al.* compared the

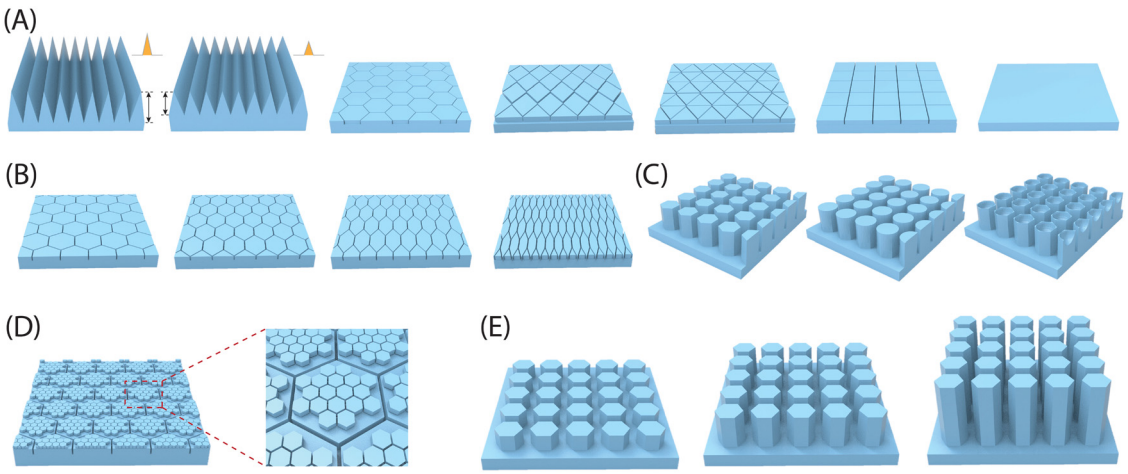

Fig. 13 The development of tree frog-inspired wet adhesive structures. (A) Polygonal micropillars with different shapes, including tooth structures with different height (0.5 mm and 1 mm), hexagonal pillars, rhomboid pillars, triangular pillars, quadrangle pillars and smooth surfaces. (B) Hexagonal micropillars with different top corners, including 120°, 90°, 60°, and 30°. (C) Hexagonal micropillars with different terminates, such as planar, T-shaped, and concave tips. (D) Hierarchical hexagonal micropillars. (E) Hexagonal micropillars with different heights (5, 10, and 20 μm).

friction forces of elongated and regular hexagonal micropillars, illustrated in Fig. 13B, revealing that elongated structures manifest greater friction compared to the regular structures in wet conditions, owing to their reduced bending stiffness and increased edge density along the moving direction.[17] Moreover, in exploring the influence of tip shape, Drotlef *et al.* engineered hexagonal micropillars terminated with planar, T-shaped, and concave tips, as demonstrated in Fig. 13C.[328] Interfacial adhesion measurements underscored the dominant role of capillary interactions in wet environments, with terminal structures exerting minimal influence on wet adhesion force. Additionally, hierarchical hexagonal micropillars could facilitate the self-splitting of liquid into smaller units (Fig. 13D), promoting the uniform distribution of liquid across the micropillars. Consequently, this leads to the formation of a thinner and more uniform liquid film, enhancing the capillary force.[28]

Furthermore, the wet adhesion capabilities are significantly influenced by the dimensions of the micro-and nanopillars. Iturri *et al.* investigated the impact of micropillar height (Fig. 13E) and found that the friction difference between pillars of 5–10 μm height was nearly negligible.[17] However, when the pillar height increases to 20 μm, the excessive deformation rate of the pillars leads to a notable reduction in friction under wet conditions. This deformation can cause the pillars to aggregate, thereby reducing the contact area.[17] Additionally, Xie *et al.* extensively examined the impacts of additional parameters on the adhesive performance of hexagonal structures.[27] They found that the interplay among height, width, and length ratios had a notable impact on related adhesive performance, challenging the idea of a single dominating parameter. The dominance of combined parameters stems from their substantial impact on the effective contact area between two interfaces and the drainage capacity of the channel. Moreover, Zhang *et al.* proposed hexagonal micropillars with $V_p \approx V_c$ enhance wet adhesion, where V_p represents the volume of liquid film adhered to each microstructure when the thickness of the interfacial liquid film equals the width of the channel, and V_c denotes the liquid volume in the channel around each micropillar when the liquid film thickness is zero.[28] This sizing approach promotes liquid self-splitting, leading to a more uniform liquid distribution and increased capillary area, partly elucidating the significant impact of combined parameters. Regrettably, due to the complexity of environments, there is currently no complete theory to unveil the adhesion mechanisms of different polygonal structures, thereby constraining the advancement of related biomimetic adhesives.

7.1.3. Octopus-inspired suckers. The octopus is a notable example of marine creature employing suction cups for reliable adhesion in water. A significant factor contributing to its underwater adhesion is suction force, which is directly influenced by the pressure differential and effective contact area. Hence, ensuring proper sealing and adaptability to contact interfaces is crucial for maximizing pressure differential and effective contact area, thereby achieving superior adhesion. Research on biomimetic adhesives aimed at emulating octopus suckers primarily focuses on studying the curvature, shapes, size, and hierarchical structure of cavities (Fig. 14).

It's been intriguingly discovered that artificial suckers designed with structures resembling those of real octopus suckers demonstrate enhanced adhesion. Baik *et al.* successfully replicated the infundibular and circumferential rims of octopus suckers, resulting in corresponding bioinspired suckers that demonstrated exceptional adaptability and consistency in adhering to objects in water.[51] These suction cups are equipped with curved cavities internally to decrease edge modulus, facilitating conformal contact with substrates and ensuring effective sealing. In addition, they also investigated the impact of the curvature radius on these suckers (Fig. 14A), revealing that a curvature of 0.93 yields a larger effective contact area and the best switchable adhesion compared to other

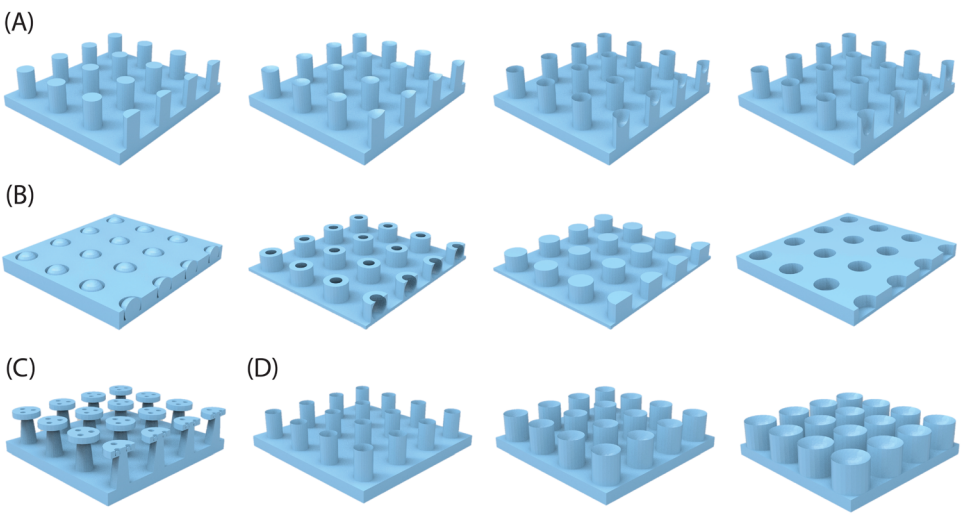

Fig. 14 The development of octopus-inspired wet adhesive structures. (A) Suckers with different curvature radii (~1.00, ~0.66, ~0.84, ~0.93). (B) Suckers with different shapes, including octopus-inspired architecture, perforated cylinders, cylindrical pillars and cylindrical holes. (C) Hierarchical micropillars with suckers on top. (D) Suckers with different diameter sizes (15, 50, and 500 μm in diameter) with ~0.93 curvature.

curvatures.[51] Furthermore, by emulating the protuberance on the roof of the sucker, they integrated microdomes into the sucker structure (Fig. 14B), resulting in robust wet adhesion owing to additional capillary-assisted suction effects generated by cohesive forces among liquid molecules.[8] Another study by Lee *et al.* highlighted that microdomes within the sucker prevent the outer wall from collapsing, ensuring underwater adhesion stability.[49] The presence of compressible air results in restricted interfacial adhesive strength in suction devices utilized in atmospheric conditions, where pressure differentials typically range from 10 to 40 kPa.[329] In contrast, these devices exhibit significantly higher adhesive strengths in water or oil environments, attributed to their incompressibility. To address this challenge, Dayan *et al.* employed direct 3D printing of elastomeric microstructures *via* the two-photon lithography technique to create a sophisticated, three-dimensional adhesive microstructure that combines features inspired by both octopus and gecko, as depicted in Fig. 14C. This bioinspired adhesive offers the advantages of both octopus and gecko-inspired microstructured adhesives, facilitating robust and reversible adhesion on both wet and dry surfaces.[330]

Regarding the impact of size on octopus suckers (Fig. 14D), Spolenak *et al.* suggested that the adhesive force generated by a sucker is directly proportional to its surface area, indicating that underwater adhesive strength does not strictly adhere to the contact-splitting principle under constant pressure difference.[331] Nevertheless, larger suction cups are prone to pressure leakage due to imperfect conformal contact, leading to a significant decline in suction force.[8,51] This could be explained by Smith's finding, he observed that smaller suckers are capable of generating higher pressure differences compared to larger ones, as smaller cavities experience less circumferential stress, enabling them to withstand greater differential pressure.[332] However, this observation is contingent upon the assumption of a consistent wall thickness, as hoop stress varies with the ratio of cavity volume to wall thickness.

7.1.4. Biomimetic adhesive structures inspired by other organisms. Apart from the aforementioned typical biological adhesion structures, there exist additional structural adhesion mechanisms on various biological surfaces in nature that researchers have leveraged to develop biomimetic adhesion materials. For instance, some insects, like beetles and blowflies achieve wet adhesive properties through liquid bridge-induced capillary adhesion. Unlike the polygonal column structure of tree frog paws, the adhesive pad structure of these insects bears a closer resemblance to gecko pads.[197] For instance, Xue *et al.* developed a biomimetic porous fiber adhesive by integrating capillary adhesion and softening technique induced by hydration. This biomimetic adhesive utilizes nanorod arrays made of block copolymers as fiber adhesive elements and is attached to a porous film composed of the same material. Notably, the continuous pores of the film aids in transporting the infused liquid from the adhesive's interior to the top of the fiber adhesive elements. The combined effects of moisture-induced softening and the additional adhesion force provided by the infused liquid result in a solid–solid contact supported by capillary action between the adhesive and the adherend (Fig. 15A),

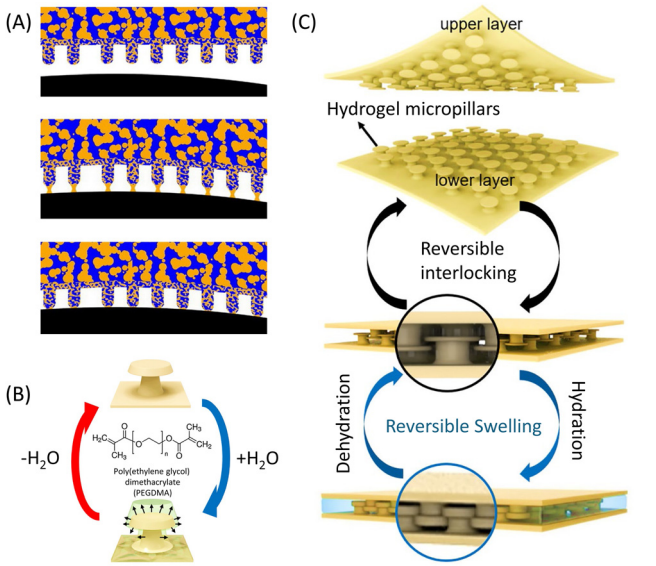

Fig. 15 The development of biomimetic adhesive structures inspired by other organisms. (A) Depicts the schematic of capillarity-supported formation of solid–solid contact. Reproduced with permission from ref. 333 Copyright 2015, Nature Publishing Group. (B) Illustrates the reversible swelling and deswelling process of the PEGDMA microhooks. (C) Schematic illustration of microhook adhesives utilizing shape reconfiguration induced by hydration to achieve a reversible mechanical interlocking mechanism to enhance wet adhesion. Figures B and C reproduced with permission from ref. 140 Copyright 2017, American Chemical Society.

leading to a substantial increase in adhesion and work of adhesion. This capillary-supported contact reveals that the adhesion force and adhesion work are independent of the external load. In conditions of low relative humidity (RH), the influence of capillary action, which remains unaffected by RH, becomes the predominant factor in determining the adhesion work. Moreover, as additional liquid accumulates on the contact surface, both the adhesion work and the distance at which the liquid bridge ruptures between the adhesive and the adherend will increase correspondingly.

Furthermore, adhesion mechanisms based on mechanical interlocking and friction strategies are present in nature, as exemplified by acanthoideae.[334,335] Park *et al.* employed the soft lithography technique to create microhook arrays based on polyethylene glycol dimethacrylate, thus developing an adhesive that can be fastened through structures in humid conditions. The unique structural configuration of the microhooks, featuring protruding heads, facilitated effective interlocking between two mating arrays. Upon exposure to water, water became entrapped in the three-dimensional polymer networks of PEGDMA, resulting in significant volume expansion (Fig. 15B). This reversible shape change, triggered by water, enables the microhooks to revert to their initial size once the water is removed (dried). Such humidity-triggered shape reconfiguration enabled strong adhesion under wet conditions in hydrogel fastener-type adhesives (Fig. 15C).

To effectively contrast the adhesion capabilities of adhesive surfaces inspired by the structures of different organisms, which achieve adhesion through structural mechanisms, they have been systematically compiled in Table 4.

Table 4 Characteristics of bio-inspired structural adhesives, encompassing their inspirations, materials, structures, test methods, and adhesive strength

Inspiration	Materials	Structures	Test methods	Substrates	Adhesive strength	Ref.
Gecko	PMMA	Vertical fibers	Probe on flat	Planar probe	~1.5 kPa	336
Gecko	Polyimide	Vertical fibers	Tensile test	Glass	~30 kPa	47
Gecko	SMP and graphene powder	Vertical fibers	Flat punch	Glass	~280 kPa	337
Gecko	PDMS	Vertical fibers	Tensile test	Si wafer	~34.8 N cm^{-2}	338
Gecko	PDMS	Vertical fibers	Probe on flat	Flat probe	~65 kPa	276
Gecko	CNT and SU8	Hierarchical pillars	Shear test	Glass sphere	185 ± 50 N cm^{-1}	339
Gecko	PDMS	Hierarchical pillars	Flat punch	Aluminum & glass	43.58 ± 4.25 kPa	340
Gecko	PU coating P(DMA-*co*-MEA)	Micro-fiber arrays with mushroom tip	Flat punch	Glass	~0.4 N	341
Gecko	PDMS coating poly(DA-MEA-NIPAM)	Vertical fibers with mushroom tip	Flat punch	Glass, silicon wafer, plastics	~10 kPa	57
Gecko	SMP	Vertical fibers with mushroom-shaped tips	Flat punch	Glass	~332.8 kPa	342
Gecko	PDMS	Wedged structures	Lap shear	Si wafer	11-50 kPa	343
Gecko	PDMS	Hierarchical vertical pillars	Probe on flat	Flat probe	~20 kPa	344
Gecko	PDMS with PAAm-PNIPAAm-PAA/Fe	Vertical fibers with mushroom tips	Flat punch	Glass, plastics	10–40 mN	345
Gecko	PDMS	Hierarchical inclined pillars	Lap shear	Glass	14–54 kPa	346
Gecko	PU	Vertical fibers with mushroom-shaped tips	Probe on flat	Glass hemisphere	~180 kPa	347
Clingfish	Silicone elastomer	Micropillar array with suction discs	Flat punch	Silicone elastome	~14 kPa	348
Beetle	PVS	Vertical fibers	Flat punch	Glass	140–170 mN	349
Remora fish	PDMS	Vertical lamellas & spinules	Flat punch & lap shear	Glass	~270 kPa (flat punch), ~195 kPa (lap shear)	350
Octopus	PDMS	Sucker with curved inner cavity	Lap shear	Glass	~30 kPa	50
Octopus	pNIPAM and PEGDA	Sucker with microdomes	Flat punch	Glass	~21 kPa	49
Octopus	PUA	Microcavities with protuberance-like dome-shaped structures	Flat punch	Si wafer	35–45 kPa	8
Octopus	PUA	Dome-like protuberance structures	Flat punch	Si wafer	1–2 N cm^{-2}	52
Octopus	PUA	Meniscus-controlled, unfoldable 3D microtips	Flat punch	Si wafer	~120 kPa	51
Octopus & Amphibians	PDMS	Hierarchical hexagonal microstructures covered with octopus-like convex structures	Peeling & flat punch	Silicon wafer, tissue	15–25 J m^{-2} (peeling), 40–50 kPa (flat punch)	351
Octopus	PDMS coated with Mfps	Millimetric square arrays of micro-suckers	Flat punch	Glass	~40 kPa	352
Octopus & Gecko	Photocurable resin	Vertical mushroom-shaped tips and suckers	Probe on flat	Glass hemisphere	~52.4 kPa	330
Suction cups	PU	Cupped microstructures	Flat punch	Glass	~1 MPa	353
Suction cups	PU	Cupped microstructures	Flat punch	Glass	0.3–0.5 MPa	354
Hooks	PEG-dMA	Microhook arrays	Tensile test & lap shear	Itself	80–140 kPa (tensile), 600–800 kPa (lap shear)	140
Tree frog	PDMS	Micro-square arrays	Flat punch	Glass	1.16–25 kPa	355
Tree frog	PDMS	Micro-hexagonal arrays (regular hexagonal)	Probe on flat	Ruby sphere	0.2–1 kPa	328
Tree frog	PU	Micro-hexagonal arrays (regular hexagonal)	Probe on flat	PMMA probe	~0.32 kPa	27
Tree frog	PDMS	Micro-hexagonal arrays (elongated hexagonal)	Probe on flat	Spherical ruby probe	~0.1 kPa	17
Tree frog	PDMS	Hierarchical hexagonal microstructures	Flat punch	Glass	~20 kPa	28
Bioinspired	PEGDMA	Vertical fibers	Flat punch & lap shear	Glass, Au, tissue	~120 kPa (flat punch), ~15 kPa (lap shear)	280
Bioinspired	Parylene/germanium nanowire forests	Randomly distributed pillars	Lap shear	Itself	~220 kPa	356
Bioinspired	PU	Randomly distributed micro-/nanopores	Lap shear & 180° peeling	Aluminum, ceramic, glass, plastic, and tissue	52.66–150.25 kPa (lap shear), 213.13–576.24 N m^{-1} (peeling)	156

7.2. Chemical biomimetic adhesives (mussel-inspired functional chemical groups)

The array of adhesives based on chemical components inspired by mussel chemistry developed over recent decades can be broadly categorized into two main types based on their bonding types and states: tape-based and glue-based adhesives (Fig. 16). Glue-based adhesives are typically formulated from liquid precursor solutions and experience a curing process either in air or underwater, facilitating interfacial interactions at the molecular level. Meanwhile, the liquids undergo polymerization and/or crosslinking to solidify (Fig. 16A). These adhesives typically

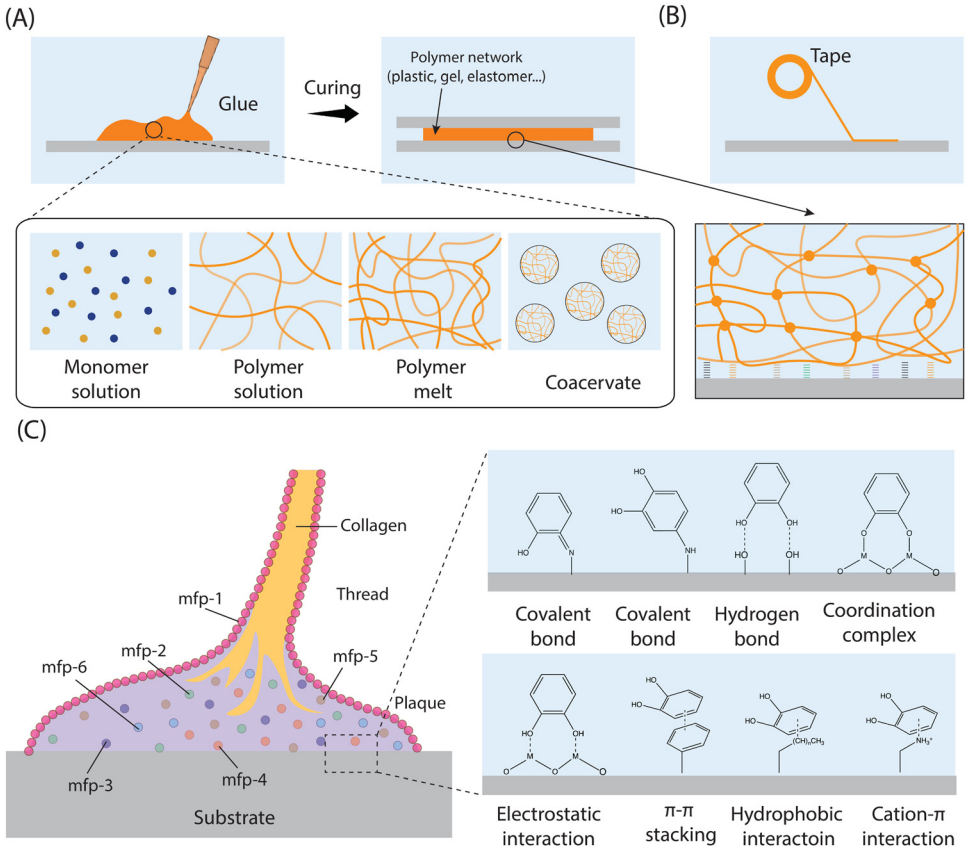

Fig. 16 Biomimetic adhesives inspired by mussel's chemistry. (A) Glue-type adhesives inspired by mussel chemistry, and the initial form of these adhesives ranges from liquid monomer or polymer solutions to melts, coacervates, or their combinations. (B) Tape-type adhesives inspired by mussel chemistry, typically manifest as soft, viscoelastic elastomers or gels. (C) Illustration depicting the structural layout of mussel byssus, indicating the arrangement of key mfps (mussel foot proteins) and common interactions (covalent bonds and physical interactions) inspired by mussel adhesion mechanisms.

boast high bonding strength and often fail cohesively, indicating stronger adhesion than cohesion. However, they necessitate lengthy curing periods, and the bonds formed are typically irreversible. Fan *et al.* have previously provided a comprehensive overview of glue-type adhesives; thus it will not be extensively covered in this work.[42] In contrast, tape-like adhesives are soft solids that adhere directly to dry or wet surfaces through chemical and/or physical interactions (Fig. 16B). Such adhesives generally offer instantaneous and reversible adhesion. Nonetheless, their bonding strength tends to weaken due to inefficient dehydration and/or surface roughness of the substrates, leading to poor interfacial contact. Consequently, the development of tape-type adhesives often focuses on enhancing dehydration and promoting the formation of robust interfacial bridges, a challenge spanning various length scales. The adhesives inspired by mussel adhesion chemistry involved in this part are primarily tape-shaped adhesives because they have greater similarity to previously discussed structural biomimetic adhesives, which is good for us to compare the advantages and disadvantages of different biomimetic mechanisms (structural and chemical components) and provide corresponding directions for future research.

Drawing inspiration from the adhesive proteins present in mussels, catechol chemistry has emerged as a prevalent approach for establishing diverse interfacial connections between tape adhesives and substrates.[31] Catechol is highly versatile, capable of physically and covalently crosslinking with different functional groups (Fig. 16C). For example, its hydroxyl groups could engage in electrostatic interactions with metal oxides and enable hydrogen bonding with hydrophilic surfaces. Furthermore, its benzene ring could facilitate cation–π interactions, hydrophobic interactions, and π–π stacking with adherents exhibiting different interface characteristics (Fig. 16C).[262] For the situation that the catechol is oxidated to quinone, the related product could establish covalent bonds with amines and thiols through Michael addition, while establishing robust coordination complexes with metal oxides.[262] Mussel-inspired tape-type materials, based on molecular interactions, encompass a range of bulk adhesives such as nanometer-thick polymer coatings, plastic films, elastomers, and hydrogels.[42] Their adhesion capabilities vary according to material properties and bonding mechanisms, which comprise physical interactions such as electrostatic forces, host–guest interactions, and hydrogen bonding; as well as chemical bonds created through processes such as Michael additions, Schiff base reactions, and C–H insertions.[43] To effectively contrast the adhesion capabilities of mussel-inspired tape adhesives with different interfacial mechanisms, the related works have been systematically compiled in Table 5.

Table 5 Characteristics of mussel-inspired tape adhesives, encompass their materials, interaction types, test methods, and adhesive strength

Materials	Interaction types	Substrates	Test methods	Adhesive strength	Ref.
Poly(cation-adj-π) gels	Electrostatic interactions & cation–π complex	Glass, metal, plastics, hydrogels (wet)	Flat punch & lap shear	~60 kPa	357
P(cation-*co*-π_{rich})	π–π and cation–π interactions	Glass, metal, plastics (wet)	Flat punch & lap shear	100–180 kPa	358
CD	Macroscopic supramolecular assembly	Azobenzene hydrogel (wet)	Lap shear	~6 kPa	359
PEG-dA + TA	Hydrogen bonds	Glass, tissue (wet)	Tensile test & lap shear	~130 kPa (tensile), ~22 kPa (lap shear)	360
P(MATAC-*co*-AAm)	Electrostatic interactions	P(AAc) gel (wet)	Flat punch	10–20 kPa	361
P(AAm) + TA + Alg-Na	Hydrogen bonds	Glass, Al, plastic, tissue (wet)	Lap shear	5–20 kPa	362
P(AAc) + TA + chitosan + Al^{3+}	Hydrogen bonds	Glass, tissue (wet)	Lap shear	4–18 kPa	363
Hydrophobically-modified gelatin	Hydrophobic interactions	Tissue (wet)	Tensile test	5–15 kPa	364
PVA hydrogel	Hydrogen bonds	Glass (wet)	Lap shear	~305 kPa	365
p(APMA-*co*-THMA)	Hydrogen bonds	Glass (dry)	Lap shear	~118 kPa	366
PACG hydrogel	Hydrogen bonds & electrostatic interactions	Intestine (wet)	180° peeling	~298 J m^{-2}	367
P(AAc-*co*-BA-*co*-Aa) organogel	Hydrophobic interactions	Glass, metal, plastics (wet)	90° peeling & lap shear	5–15 kPa (lap shear), 200–400 J m^{-2} (peeling)	368
P(AAc-*co*-MEA-*co*-Aa-*co*-AU)	Hydrophobic interactions	Glass, metal, plastics (wet)	Lap shear	5–25 kPa	369
TAs	EDC/NHS coupling, hydrogen bonds, & electrostatic interactions	Porcine skin (wet)	180° peeling	~1116 J m^{-2}	13
Tetra-PEG with NHS esters	EDC/NHS coupling	Porcine skin (dry)	Lap shear	~20 kPa	370
DST without NHS ester	Hydrogen bonds & electrostatic interactions	Porcine skin (wet)	180° peeling	~710 J m^{-2}	371
Cucurbit [8] uril-based hydrogel	Host–guest interactions	Glass (dry)	Lap shear	~1.1 MPa	372
P(AAm-*co*-urushiol) + Glycerol	Hydrophobic interactions & hydrogen bonds	Glass (wet)	180° peeling & lap shear	200–400 J m^{-2} (peeling), ~16 kPa (lap shear)	373
P(AAc-*co*-UCAT) + chitosan	Covalent/electrostatic attraction/π–π/cationic–π/hydrogen bonds	Tissues (wet)	180° peeling	900–1200 J m^{-2}	374
PEDOT:Hep hydrogels	Schiff's base reaction	Cardiac muscle (dry)	Lap shear	~1.6 kPa	375
PAMAM-*g*-Diazirine	Carbene reaction	PET (dry)	Lap shear	~45 kPa	376
PAAM hydrogel	Mechanical interlock	P (AAc-*co*-AAM) hydrogel (wet)	Lap shear	~130 J m^{-2}	377
P([MATAC][TFSI])	Hydrophobic interactions	Glass, metal, plastics, wood (wet)	Lap shear	200–700 kPa	378
PAH-catechol	Covalent bonds	Glass, tissue, PET (wet)	Lap shear	1.5–10 kPa	379
SRBSS	Covalent bonds	Tissue (wet)	Lap shear, tensile test, 180° peeling	~1.04 MPa (lap shear), ~0.76 MPa (tensile), ~1021 J m^{-2} (peeling)	181
SF organo-hydrogel	Covalent bonds	Tissue (dry)	90° peeling	~17.46 J m^{-2}	380
Sil-MAS	Photo-induced polymerization	Rat skin (dry)	Lap shear	~100 kPa	381
NPs-P-PAA hydrogel	Catechol-based chemistry	Porcine skin (dry)	Lap shear	~27.5 kPa	158
TAPTRA	Catechol-based chemistry	Porcine skin (dry)	Tensile test	~600 J m^{-2}	382
AdhHG/HAp	Photo-induced polymerization & Catechol-based chemistry	Porcine skin (dry)	Tensile test	~120 kPa	383
L-DMA–PCL hydrogel	Hydrogen bonds, π–π interaction, cation–π interaction, & metal coordination	PTFE, PP, stainless steel, aluminum, glass (dry)	Tensile test	21.1–38.4 kPa	384
Alg/PAM-FT	Electrostatic interactions, covalent bonds & physical interpenetration	Skin (dry)	Peeling test	50–70 J m^{-2}	385
PDA–PAM-C_n	Hydrophobic interactions	Porcine skin (dry)	Tensile test	20–25 kPa	386
CLD hydrogel	Hydrogen bonds, metal complexation, & hydrophobic interaction	Wood, glass, pig skin, pig bone, pig heart, pig liver and pork	Tensile test	0.88–88.64 kPa	387
*x*DA-*y*QT-QP hydrogels	Hydrogen bonds	Porcine skin (dry)	Lap shear	7.5–10 kPa	388

In summary, the choice between structural and chemical adhesion in the construction of biomimetic artificial adhesives depends largely on the intended applications. Structural adhesion-based adhesives, like those mimicking gecko feet, offer reversible adhesion but are susceptible to contamination from particles such as dust. Conversely, adhesives based on mussel chemistry exhibit strong interfacial adhesion, making them difficult to peel off. On the other hand, structural adhesion faces challenges such as limited adhesion strength and suitability for specific environments; for instance, gecko-inspired adhesives

lose their effectiveness in humid or underwater conditions due to hydration. Therefore, future research needs to focus on leveraging the advantages of both structural and chemical adhesion to develop advanced biomimetic artificial adhesives.

8. Smart artificial adhesives with tunable adhesion properties

Recent advancements in smart materials have paved the way for the development of intelligent adhesives.[389–391] The inherent characteristics of these soft smart materials empower biomimetic artificial adhesives with enhanced attachment and easier detachment through chemical changes or mechanical deformations controlled by external stimuli. By integrating these biomimetic adhesives with smart materials such as hydrogels, liquid crystalline elastomers, magnetic nanoparticles, thermoplastic polyurethane, *etc.* researchers have achieved widespread switchable, reconfigurable, and stimuli-responsive adhesion. This has been accomplished by adjusting various environmental stimuli, including light, thermal, mechanical, magnetism, electricity, humidity, pressure, chemicals, *etc.* (Fig. 17).[57,279,345,392–395] These strategies could offer innovative insights for developing the next generation of biomimetic adhesives, substantially broadening their applicability across diverse fields.

8.1. Tunable adhesion for the solid–liquid adhesion system

In the solid–liquid adhesion system with adjustable adhesion force, the existing responsive intelligent interfaces are mainly divided into two categories: (1) solid structure responsive surfaces, which directly undergo structural or chemical changes upon external stimulation, thereby affecting the adhesion state between the surface and the droplets; (2) porous responsive surfaces, where lubricant liquid is infused into the pores. When external stimuli are applied to these liquid-infused porous surfaces, the infused lubricant liquid alters its wetting morphology on the solid surface, consequently influencing the contact between the droplet and the surface to adjust the solid–liquid adhesion force accordingly. The following discussion will provide examples of these two types of smart responsive solid–liquid interfacial adhesion systems to illustrate their similarities and differences.

8.1.1. Responsive solid structure surfaces. During the last decades, research on solid–liquid interfaces has predominantly

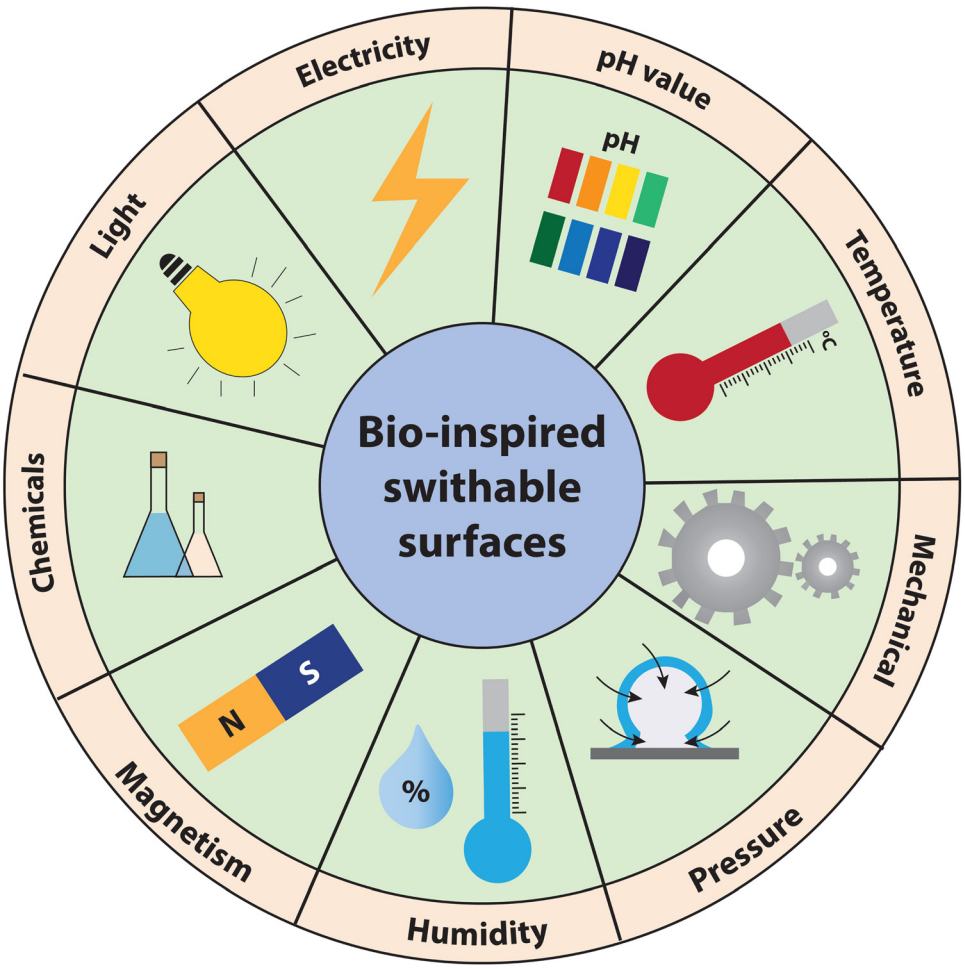

Fig. 17 The various external stimuli of smart artificial adhesives with tunable adhesion properties. Typical stimuli include light, thermal, mechanical, magnetism, electricity, humidity, pH, pressure, chemicals, *etc.*

centered on enhancing the anti-wettability and reducing the adhesion between solid surfaces and liquids through two main approaches: structural modification involving the creation of micro-nano structures on the solid surface, and chemical modification through the application of liquid-repellent polymers.[84] While these methods effectively prevent droplets from spreading and promote easy sliding off the surface, the uncontrollable detachment behavior of droplets on solid surfaces is often undesirable. Consequently, there has been a shift towards investigating stimulus-responsive surfaces with controllable wetting and adhesion properties. In recent years, numerous smart and responsive materials have been developed to modify the structure and/or chemical composition of surfaces, allowing for intelligent and remote control of their physical and/or chemical characteristics in response to environmental stimuli. This advancement has enabled traditional wettable surfaces to acquire controllable wetting and adhesion behaviors to liquids, facilitating the transition between low and high droplet adhesion on their surfaces. Through the dedicated efforts of researchers, a range of surfaces capable of altering droplet adhesion and wetting behavior in response to various stimuli have been successfully engineered.[85,396] Although stimulus-response surfaces employ various actuation behaviors, the internal working mechanisms can generally be classified into the following categories (Fig. 18).

Strategy I: modulating the physical shape of micro-nano structures to adjust the wettability and adhesion of solid surfaces (Fig. 18A). For example, Wang *et al.* devised a novel approach for self-assembling mushroom-like pillar arrays, omitting the need for templates. Through the application of a magnetic field, these mushroom-like pillars underwent reversible deformation, thereby inducing a switch in wetting and adhesion behavior for oil.[397] It was observed that the contact angles of hexadecane droplets on these superamphiphobic surfaces could transition reversibly between $150 \pm 1^\circ$ (low adhesion state) and $38 \pm 2^\circ$ (high adhesion state). Intriguingly, these switchable surfaces exhibited remarkable capabilities for transporting oil droplets without the need for lubricating liquid films. This research not only achieves extensive and reversible wetting switches for oil but also unveils new pathways for fabricating adjustable superamphiphobic surfaces featuring adaptable mushroom-like microstructures. Such surfaces could find application in microstructure-dependent friction, adhesion control, and various other fields. Notably, if using magnetically responsive materials like nickel, iron, and strontium ferrite in the creation of micro-structured surfaces allows for the remote manipulation of wetting behavior through adjusting micro- and nanopillars.[398,399] This enables a transition between a superomniphobic state with low adhesion and an omniphilic state with high adhesion by adjusting an external magnetic field. For instance, the interaction between water and liquids with low surface tension can be influenced by applying an external magnetic field, owing to the presence of magnetic materials on a reconfigurable surface.

Strategy II: modulating the distribution and morphology of micro-nanostructures on the surface through stretching or bending of the substrate to adjust the wettability and adhesion of solid surfaces (Fig. 18B). Drawing inspiration from natural organisms, Bai *et al.* devised a sunlight-driven recoverable superhydrophobic surface with micropillar array based on laser etching on a thermal-sensitive substrate.[400] The light-responsive behavior was further achieved by introducing the reduced graphene oxide (rGO) into the shape-memory polymer (SMP) due to its photothermal properties. As a consequence, the temperature of the composite increased to 80 °C after exposure to sunlight, demonstrating excellent light-heat conversion efficiency. This temperature exceeds the RGO-SMP composite's glass transition temperature (T_g = 47 °C), thereby easily triggering its shape-memory behavior through natural sunlight exposure. When the micropillar array of the RGO-SMP composite was subjected to deformation *via* pressing or stretching treatments, the surface exhibited a state of high liquid droplet adhesion (contact angle: $143.8^\circ \pm 1.8^\circ$, slide angle: $40^\circ \pm 2^\circ$). Notably, the complete restoration of the original surface morphology and related superhydrophobic low adhesion (contact angle: $152.3^\circ \pm 1.8^\circ$, slide angle: $9.5^\circ \pm 0.5^\circ$) occurred upon sunlight irradiation for several minutes, showcasing remarkable recovery capabilities. Generally,

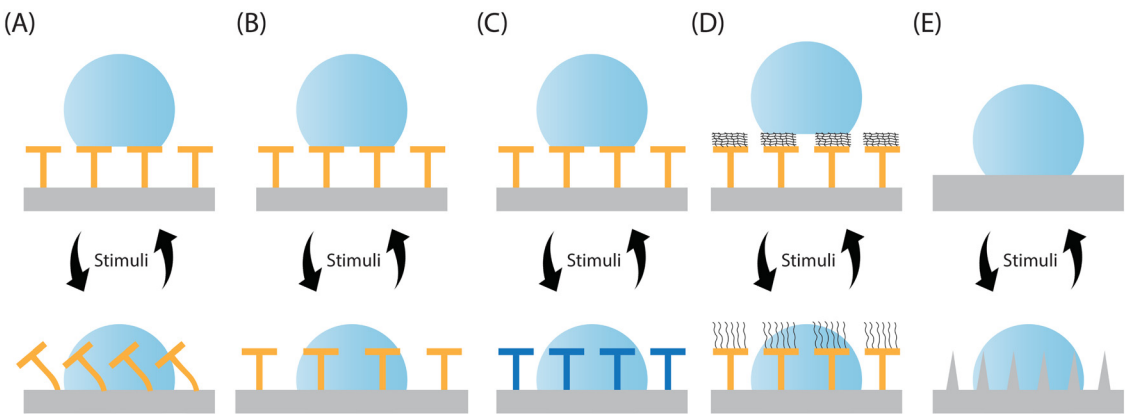

Fig. 18 Construction strategies to control surface wetting and adhesion for solid structure surfaces. (A) Modulating the physical shape of micro-nano structures. (B) Modulating the distribution and morphology of micro-nanostructures on the surface through stretching or bending of the substrate. (C) Modulating the chemical properties of micro-nano structures. (D) Modulating the acting state of functional molecules. (E) Modulating the formation or disappearance of microneedles.

the structure and distribution of micro-nano arrays can undergo alterations when the whole substrate is subjected to mechanical force, which can be categorized into pressure, tension, and torsion based on the type of mechanical stimulus.[401] Mechanical stimulation offers the benefits of prompt, substantial, continuous, and eco-friendly effects. This form of stimulation primarily affects polymer-based micro-nano array structures, frequently combined with structural recovery mechanisms aroused by other stimuli that could lead to the recovery of the structures.

Strategy III: modulating the chemical properties of micro-nano structures to adjust the wettability and adhesion of solid surfaces (Fig. 18C). Inorganic semiconductor oxide materials like TiO_2, ZnO, SnO_2, WO_3, and V_2O_5, which generate electron–hole pairs when exposed to light, can undergo reversible changes in polarity, chemical configuration, or composition under light stimulation.[402] Through specific methods, photosensitive materials can be shaped into micro-nanostructures to achieve reversible wettability responses. For instance, Kang *et al.* presented a study on TiO_2 nanotube arrays (NTAs) capable of undergoing reversible transitions between under-oil superhydrophobicity and superhydrophilicity.[403] This smart controllability is achieved through a combination of UV irradiation and heating processes, leveraging the interplay between surface nanostructures and chemical composition variations. Initially, the TiO_2 NTAs surface exhibits under-oil superhydrophobicity, characterized by low water droplet adhesion, following a straightforward anodizing and heating procedure. Upon exposure to UV irradiation, the surface shifts to under-oil superhydrophilicity, exhibiting high water droplet adhesion, and subsequent heating restores its original under-oil superhydrophobic state. This reversible transition between extreme states is facilitated by alternating UV irradiation and heating treatments. Importantly, it is observed that following both UV irradiation and heating in air, the TiO_2 NTAs surface demonstrates uniform superhydrophilicity. The discrepancy in behavior between air and oil environments highlights the significant impact that environmental media, in addition to surface microstructure and chemical composition, can have on wetting and adhesion properties.

Strategy IV: modulating the acting state of functional molecules to adjust the wettability and adhesion of solid surfaces (Fig. 18D). The process of surface grafting polymer brushes has emerged as a crucial domain of investigation aimed at tailoring material interface characteristics.[404–406] Some polymer brushes employed for grafting exhibit molecular traits that respond to variations in external environmental conditions, rendering them particularly suitable for applications requiring smart wetting and adhesion surfaces. For example, Bauman *et al.* utilized benzophenone-initiated UV polymerization to graft a layer of poly(*N*-isopropylacrylamide) (PNIPAAm) onto micro-pillared surfaces, resulting in the creation of a temperature-responsive surface capable of modulating surface wettability and adhesion based on external temperature adjustments.[407] When the ambient temperature is above the lower critical solution temperature point (LCST), the grafted PNIPAAm brushes remain immiscible with water, rendering the surfaces highly hydrophobic with low adhesion, characterized by a large contact angle of 120°. Conversely, below the LCST, the grafted PDMS micropillar surface swells and absorbs water, transitioning to a hydrophilic state with high adhesion, as evidenced by a smaller contact angle of 33°. Notably, grafting on micropillars, as opposed to flat surfaces, amplified the change in contact angle across PNIPAAm's hydrophobicity–hydrophilicity switch and improved graft hydration. This synergistic effect between grafted PNIPAAm and micropillars yielded a robust temperature-responsive wetting and adhesion property.

Strategy V: modulating the formation or disappearance of microneedles to adjust the wettability and adhesion of solid surfaces (Fig. 18E). Introducing magnetic particles like iron, cobalt, or ferric oxide into the elastic substrate allows for the controlled formation of magnetic cones, leading to enhanced contact between the solid–liquid interface, thereby enabling precise control over adhesion between the interface and the droplets. Guo *et al.* devised a magnetically responsive gel interface comprising iron powder/polydimethylsiloxane (Fe/PDMS)/silicone oil.[408] By manipulating the substrate's morphology using a magnetic field, intelligent control over water droplet movement on this interface was achieved. When no magnetic field was applied, the sliding angle (SA) of the water droplet measured $7.9 \pm 1.0°$, showing low droplet adhesion. However, under a 0.4 T magnetic field, the SA increased to $40.5 \pm 4.2°$, which means high droplet adhesion. Upon removal of the magnetic field, the droplet's sliding angle reverted to its initial value, enabling it to slide along the interface once more. This is because without a magnetic field, the gel-droplet interface is exceptionally smooth, exhibiting a linear roughness (R_a) of 0.968 μm, and the droplet is in the Cassie state with low adhesion. Consequently, droplets can slide easily. Conversely, application of a magnetic field induces the formation of a vertical magnetic cone array on the substrate surface, elevating R_a to 12.101 μm, and transitioning the contact interface to the Wenzel state with high adhesion. This extends the three-phase contact line, significantly increasing droplet movement resistance and interfacial adhesion force, thereby pinning droplets to the interface and impeding sliding. Upon magnetic field removal, the interface morphology reverts, allowing droplets to resume sliding.

The aforementioned five strategies represent the primary methods for fabricating stimulus-responsive surfaces capable of controlling the wetting and adhesion properties of droplets. While we have provided examples following each construction strategy to aid reader comprehension, it's essential to note that beyond the stimulus types covered in these instances, numerous other stimulus types have also been constructed using similar strategies. Consequently, we have compiled in Table 6 a summary of the key stimulus-responsive surfaces utilized for manipulating droplet behavior in recent years. This table includes details such as their composition, construction strategies, stimulus types, and corresponding operational mechanisms.

8.1.2. Responsive slippery liquid-infused porous surfaces (SLIPs). Unlike solid structure-responsive surfaces, responsive slippery liquid-infused porous surfaces usually entail the

Table 6 Bio-inspired and artificial strategies to control surface wetting and adhesion for solid structure surfaces

Materials & structures	Strategy	Stimuli	Working mechanisms	Ref.
High-aspect-ratio Ni wires topped with micrometer-sized hemispherical caps	Strategy I	Magnetic	The magnetic field was used to bend Ni micronails to adjust the wetting and adhesion state	398
Negative photoresist IP-S with deformable doubly re-entrant structures	Strategy I	Liquid evaporation	The doubly re-entrant microstructures can bend directionally and recover rapidly during evaporation/immersion in some selected solvents	409
Elastomer micropillar array with magnetic-responsive particles	Strategy I	Magnetic	The different distances and orientations between micropillars and the magnet would lead to different magnetic field strengths, thus exhibiting different deflection behaviors	399 and 410
PDMS with micropillars	Strategy II	Mechanical	Combining the mechanical tuning strategy with capillary-force-driven self-assembly (CFSA) to achieve a controllable transformation of the CFSA structure	411
Shape memory polymer (SMP) with micropillar arrays	Strategy I	Thermal & mechanical	After heating and pressing under external pressure, the micropillars collapsed. Further heating the surface, the surface micro- and nanostructure recovered	412–414
Shape memory film with 1–20 μm micro-caps	Strategy II	Mechanical	Tuning surface topography *via* reversible stretching/bending	415
Polydopamine-treated porous meshes with nano-Ag pine needles and aminoazobenzene (AABN)	Strategy III	UV Light & visible light	Irradiated with 365 nm UV light, the N=N bond of AABN was broken and rotated, the hydrophilic silver pine nanoneedles were exposed. After irradiation with visible light, the mesh could turn back to its initial state	416
Photoreconfigurable azopolymer with micropillar	Strategy I	P-polarized light	The micropillar array could be bent and reconstructed under p-polarized light	417
Shape memory PU with micropillar arrays	Strategy I	Near-infrared (NIR) light	Subjected to near-infrared light at a power of 1.0 W, the surface microstructure undergoes gradual degradation due to heat. Lower the NIR power to 0.5 W, the destroyed structure will recover	418
Carbonyl iron particles (CIP) doped PU SMP with micropillar arrays	Strategy I	Mechanical & Near-infrared (NIR) light	After pressing under external pressure, the micropillars collapsed. Further irradiated with 808 nm NIR, the curved micropillars could be restored	419
Piezoelectric PVDF/PMMA fibers grafted with 4-carboxybenzenediazonium tosylate and 4-(heptadecafluorooctyl) benzenediazonium tosylate diazonium salt	Strategy IV	Electric	The grafted $-C_6H_4C_8F_{17}$ functional group would experience rearrangement under the application of electric field triggering, and change the acting state of functional molecules	406
CIPs/PDMS elastomers	Strategy V	Magnetic	The applied magnetic field can change the surface microstructure and roughness	420
PS film with high-aspect-ratio magnetic micropillar arrays	Strategy I	Magnetic	Applying an external magnetic field, the microarray can be freely switched between the upright state and left and right bending	421
PDMS with magnetized micropillar array (NdFeB magnetic particles), and surface hydrophobization treatment	Strategy I	Magnetic	Magnetic nano/micropillar array (MNA) has a low adhesive gradient along the direction of magnetically induced tilt-angles. Tilt-angles of nano/micropillars can be controlled by the external magnetic field	422
Magnetic PDMS microciliary array (Co magnetic particles), and surface superhydrophobization treatment	Strategy I	Magnetic	Under an alternating external magnetic field, the surface alternates between clustered and nonclustered structures	423
PDMS with microplate array filled with magnetic particles	Strategy I	Magnetic	The deformation of pillar array under the external magnetic force results in the transformation of hydrophilicity of the surface, which largely enhances the adhesion	424
Multi-layered TiO_2	Strategy III	UV light	Electron holes can be generated on TiO_2 surface because of the irradiation of UV light, which will further combine with lattice oxygen to create unstable oxygen vacancies. Thus, the chemical properties of surface can be switched based on the dissociation of water molecules and generation of Ti–OH groups	425

introduction of a lubricating liquid layer into the pores (Fig. 19).[426] This liquid layer coats the entire solid surface structure, prompting droplets on the surface to interact with it, thereby impacting the wetting and adhesion behavior of the droplets. It should be noted that the traditional definition of SLIPs means that the liquid height of the lubricating layer is higher than the height of the micro-nano structure of the solid surface, where the lubricating layer liquid and droplets are immiscible, meaning they do not dissolve in each other and do not undergo any chemical reactions.[427]

As shown in Fig. 19A, the wetting and adhesion behavior of a repellent droplet varies between a solid structure surface without a lubricating layer and SLIPs with a lubricating layer. This discrepancy arises due to the presence of the lubricating layer, which prevents direct contact between the droplets and the micro-nanostructure of the solid surface. Consequently, adhesion

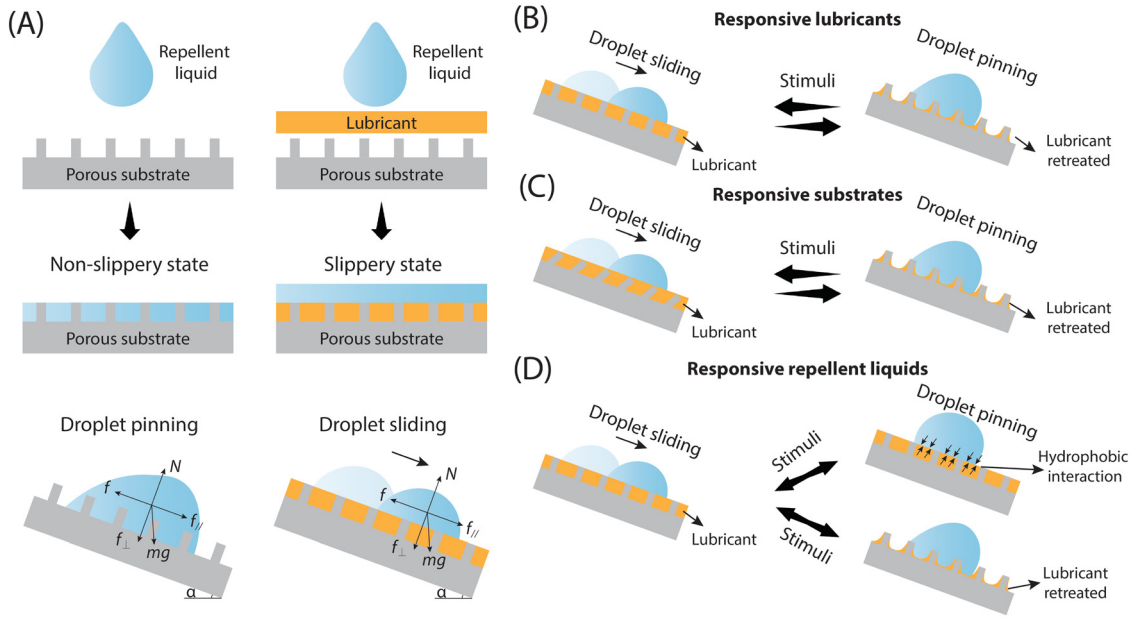

Fig. 19 Construction strategies to control surface wetting and adhesion for SLIPs. (A) The difference in droplet behavior on the substrate with or without a lubricant layer. (B) Utilizing a responsive lubricant layer to fabricate SLIPs capable of controlling the wetting and adhesion properties of repellent droplets. (C) Utilizing a responsive porous substrate to fabricate SLIPs capable of controlling the wetting and adhesion properties of repellent droplets. (D) Utilizing responsive repellent droplets to fabricate SLIPs capable of controlling the wetting and adhesion properties of repellent droplets.

is reduced, as the solid-droplet three-phase contact line and the chemical properties of the solid surface could be neglected in this situation, allowing the repellent droplets to exhibit sliding behavior on the lubricating layer with minimal external force. Moreover, by implementing stimulus-response mechanisms to regulate the relative heights of the lubricating layer liquid and micro-nano structures of the solid surface, it becomes possible to influence the wetting and adhesion properties of repellent droplets through both the lubricating layer and micro-nano structures of the solid surface (*e.g.* the transition between the Cassie model and the Wenzel model), enabling corresponding adjustments in adhesion. During the past decade, researchers have made significant strides in developing responsive SLIPs that enable the modulation of droplet wetting and adhesion on solid–liquid composites. Although stimulus-responsive SLIP utilizes different actuation mechanisms, similar to responsive solid structured surfaces, their inner working mechanisms can also be summarized into different categories. (PS: Since responsive SLIPs still belong to the solid–liquid adhesion system, we will continue the numbering in the previous part when introducing the construction strategies.).

Strategy VI: modulating the wetting or coating status of responsive lubricants to adjust the wettability and adhesion of SLIPs system (Fig. 19B). Employing lubricants possessing stimulus-responsive properties for actuation is regarded as a promising method for developing SLIPs featuring reversible wetting and adhesion. In such cases, external stimuli can directly control the status (overcoats or retreats into the substrate) of lubricant layers, altering the contact dynamics between repellent droplets and SLIPs, to adjust the wetting and adhesion behavior of the repellent droplet. For example, Tian *et al.* presented a novel approach for rapid and precisely controllable liquid movement on smart SLIPs with magnetic responsive lubricant.[428] The prepared SLIPs exhibit instantaneous responsiveness to changes in the magnetic field gradient, leading to a rapid transition in surface roughness within milliseconds. This responsiveness far surpasses that of other surfaces by at least one order of magnitude. As a result, water droplets can seamlessly track the motion of the composite interface in response to the magnetic field gradient. Additionally, by adjusting the motion direction of the magnetic field gradient, the transport direction of water droplets can be effectively controlled. This composite interface holds promise for applications such as microfluidic devices, where it can serve as an efficient pump for transporting immiscible liquids and various objects within microchannels. Building upon Tian *et al.*'s work, Wang *et al.* expanded on this concept by developing a range of magnetically responsive SLIPs systems with diverse characteristics by incorporating ferrofluids (which serve as responsive lubricants) into various microstructured substrates.[429] They conducted a comprehensive analysis comparing the magnetic pressure ($|P_m| \approx \mu_0 M_s H_0$) and capillary pressure $\left(P_\gamma = \frac{2\gamma}{d_y}\right)$ to determine the conditions under which ferrofluids are either trapped within or extracted from the pores of the substrate. Here, μ_0 denotes the vacuum permeability; M_s represents ferrofluid's saturation magnetization; H_0 signifies the external magnetic strength; γ refers to the ferrofluid/air interface tension; and d_y indicates the channel width and porous substrate's maximum diameter. When $|P_m|$ is less than or equal to P_γ, the ferrofluid becomes trapped within the porous structure. In contrast, the

ferrofluid will be squeezed out and cover the porous structure when $|P_m|$ exceeds P_γ. Systematical study was carried out by meticulously analyzing the influence of capillary pressure and magnetic force on entrapment and extraction of ferrofluid. Ultimately, they achieved droplet flow control and adhesion switching across various scales, from micrometers to centimeter. On the other hand, adjustments in the wetting and adhesion characteristics of repellent droplets on SLIP surfaces can also be accomplished by changing the state (phase) of the lubricating layer. For instance, Wang *et al.* integrated paraffin with a directional porous substrate to create temperature-responsive SLIPs with anisotropic behavior.[430] Specifically, when the ambient temperature fell below the melting point of paraffin (44–46 °C), the repellent liquids remained in the Wenzel state, impeding sliding in all directions. However, as the environmental temperature surpassed the melting point, the paraffin transitioned into a liquid phase, rendering the surface anisotropically slippery. Consequently, the repellent liquid could slide effortlessly in a the direction parallel to the grooves.

Strategy VII: modulating the surface's geometry of responsive solid substrates to adjust the wettability and adhesion of the SLIPs system (Fig. 19C). In many cases, the wetting behavior of reversible SLIPs, which rely on responsive substrates, can be altered reversibly by adjusting the geometric features of the solid surface, without altering their chemical composition. Simply changing the surface structure of the substrate can lead to changes in the motion characteristics of a repellent droplet on the SLIPs, and this wettability manipulation induced by responsive substrates is consistent, reversible, and predictable.[426] For instance, Yao *et al.* devised a mechanical stretching SLIPs system by combining a PDMS membrane and a Teflon membrane featuring an irregular porous structure, thereby creating an elastic solid substrate.[431] They then infused a perfluorinated liquid into the substrate to serve as a lubricant. In its unstressed state, a thin layer of lubricant completely covered the porous substrate, resulting in a smooth lubricant/repellent liquid interface. This configuration allowed repellent liquid droplets to slide effortlessly due to minimal interfacial adhesion. However, when mechanical tension was applied, such as a 6% strain, the elastic substrate elongated, causing the lubricant to retract into the expanded nanopores. Consequently, the porous solid became exposed to the repellent liquid, leading to a rough lubricant/repellent liquid/solid interface and increased interfacial adhesion. As a result, the repellent liquid droplet became pinned to the surface. Moreover, the researchers found that the sliding angle (SA) increased with higher strains if the amount of lubricant was fixed. Similarly, under a certain strain, surfaces with less lubricant exhibited higher SA values. Apart from altering the overall shape of the entire substrate, the interaction between repellent droplets and SLIPs can be manipulated by directly controlling the shape of the micro-nano structures on the substrate's surface. Huang *et al.* devised magnetically transformable SLIPs composed of PDMS micropillars embedded with ion particles.[432] Under the influence of magnetic fields exceeding 0.1 T and directed in various orientations, the micropillars exhibited reversible transformations between an upright position and complete bending. In the upright position, repellent droplets made contact with the hydrophobic tips of the micropillars, resulting in the formation of air pockets between the repellent droplet and the solid substrate, thus rendering the droplet hydrophobic. Conversely, when the micropillars were fully bent by an external magnetic field, the repellent droplet came into contact with the continuous lubricant film, inducing a slippery state in the droplet. Consequently, the surface showcased the capability to switch between superhydrophobic and slippery states, with the repellent droplet demonstrating bouncing and sliding behaviors, respectively.

Strategy VIII: modulating the responsive repellent droplets to adjust the wettability and adhesion of the SLIPs system (Fig. 19D). The manipulation of repellent droplets' wetting and adhesion behaviors on SLIPs can also be achieved by imparting responsiveness to repulsive droplets. This responsiveness includes imparting additional force to the repellent droplet to change its contact area and state with SLIPs, or changing the active ingredients of the repellent droplet under stimulation. For example, in an electrowetting experiment, applying an electric field between a conducting liquid and a counter electrode beneath the liquid surface reduced the contact angle (CA) of a droplet on this surface.[433] Taking inspiration from this mechanism, Guo *et al.* devised a bar-shaped electrode suspended above the surface to ensure continuous contact between the repellent droplet and the electrode during the sliding process.[434] Without voltage applied, the droplet slid effortlessly due to the presence of a thin layer of lubricant. However, the electrostatic attraction between the substrate and droplet increased when voltage was applied (*e.g.* a water droplet with 3.5 V, a KCl droplet with 0.5 V, and an ionic liquid droplet with 2.5 V). Diminishing the lubricant thickness and causing the droplet to be pinned on the surface. Subsequently, they delved into how the properties of the lubricant, including viscosity and conductivity, influenced the wettability and/or adhesion-switching characteristics of electric field-responsive SLIPs.[435,436] Compared to lubricants with high viscosity and non-conductive properties, those with low viscosity and conductivity facilitated repellent liquid motion switching under a lower voltage. This difference stemmed from the solid-like nature of high-viscosity lubricants, which rendered them less deformable. Furthermore, the potential to trap a KCl droplet decreased from 1.5 V to 0.5 V by changing the conductivity of lubricant, owing to the formation of an extra electrical double layer within substrate and droplet. When it comes to the strategy of changing the active ingredients of the repellent droplet under stimulation, Wang *et al.* showed that biological droplets containing ssDNA exhibited thermoresponsive wetting behavior on SLIPs.[437] As temperature ranges from 10 to 30 °C, the ssDNA undergoes reversible molecular conformation changes, resulting in decreased exposure of hydrophobic parts and weakened interfacial adhesion. Consequently, the biological droplets displayed easier sliding at higher temperatures. This study presents possibilities for controlling the motion of biological liquids in microdevices.

Similar to the construction strategies for responsive solid structure surfaces. Numerous other stimulus types and materials have also been constructed as responsive SLIPs for manipulating droplets' behavior using the above three strategies. Consequently, we have assembled a summary of the key stimulus-responsive SLIPs utilized for manipulating droplet behavior in recent years in Table 7. This table provides information on their composition, construction methods, types of stimuli employed, and corresponding operational mechanisms.

8.2. Tunable adhesion for solid–solid and solid–liquid–solid adhesion systems

By integrating the adhesive structures and/or chemical compositions outlined in Section 7 with advanced smart materials, a variety of switchable, reconfigurable, and stimulus-responsive adhesives used for solid–solid and solid–liquid–solid adhesion systems have been realized.[459] These smart stimuli-responsive adhesives have significantly expanded their utility across diverse fields when compared to conventional biomimetic adhesive surfaces. In this part, we categorize these reversible adhesives into two groups according to their adhesion mechanisms: those relying on reversible physical interactions and those based on reversible covalent bonds.

8.2.1. Tunable adhesion based on reversible physical interactions. Generally, smart reversible adhesives rely on physical interactions to achieve adhesion, including dipole–dipole interactions, metal–ligand interactions, hydrogen bonds, π–π interactions, hydrophobic interactions, mechanical interlocking *etc.*, as their primary bonding mechanism. This is because these intermolecular adhesion forces are typically weak, allowing for reversible bonding and debonding under mild conditions. Consequently, most of the reversible adhesives developed to date are based on these weak adhesion forces. Similar to stimulus-response adhesive surfaces (solid–liquid adhesion system) for controlling droplet wetting and adhesion, the internal working mechanisms of switchable adhesives based on physical interactions used for solid–solid and solid–liquid–solid adhesion systems can also be classified into different categories (Fig. 20).

Strategy 1: modulating the physical shape of substrates to adjust the adhesion of adhesive surfaces (Fig. 20A and B). This strategy primarily achieves reversible toggling between robust adhesion and effortless detachment by adjusting the shape of the adhesive substrate to alter the contact area between its surface's micro-nano adhesive structures and the adhered surface. It mainly involves two categories: shape drive, which does not involve changes in substrate volume and deformation drive based on changes in substrate volume. As an example of the former (Fig. 20A), Kizilkan *et al.* introduced a bioinspired photo-responsive adhesive (BIPMTD) comprising three layers: a surface layer with mushroom-like structures, a light-sensitive liquid crystal elastomer (LCE) in the middle, an extra layer in the bottom for sealing.[392] This innovative adhesive exhibits robust adhesion, facilitated by the PDMS microstructured adhesive layer in the absence of ultraviolet light. Conversely, upon exposure to ultraviolet light, the adhesive undergoes surface bending due to the photoisomerization-induced shape alteration of azobenzene units. This transformation reduces the actual contact area between the PDMS adhesive microstructures and the adherend surface, leading to the detachment of the adhesive from the adherend surface. When it comes to the deformation drive based on changes in substrate volume, it usually exists in responsive hydrogel adhesives. For example, Yi *et al.* introduced a wet-responsive and biocompatible hydrogel adhesive that offers switchable and controllable adhesion properties (Fig. 20B).[279] In their dry state, the hydrogel adhesives exhibit remarkable adhesion strength, reaching approximately 191 kPa, facilitated by nano- or microstructure arrays on the surface. Upon contact with water, both nano/microscopic and macroscopic shape reconfigurations occur within the hydrogel adhesive, effectively disabling adhesion (∼0.30 kPa) with an exceptionally high adhesion switching ratio (>640). The superior adhesion characteristics persist through multiple cycles of hydration and dehydration, indicating their reusability. Composed of a biocompatible hydrogel, these adhesives offer controllable adhesion modulation with water, rendering them compatible with a variety of materials and surfaces, including biological substrates.

Strategy 2: modulating the physical shape of micro-nano structures to adjust the adhesion of adhesive surfaces (Fig. 20C and D). Adjusting the shape of adhesive structures proves to be an effective method for developing responsive adhesives capable of transitioning between states of strong and weak adhesion in response to external stimuli. Similar to the manipulation of substrate shape, the adjustment of micro-nano structure shape also falls into two categories: shape-changing that doesn't entail alterations in micro- and nanostructure volume and deformation-driven adjustments relying on changes in micro- and nanostructure volume. As an exemplar of shape-changing without altering micro- and nanostructure volume (Fig. 20C), Zhao *et al.* devised a dynamic adhesive system capable of adjusting adhesion levels on demand. Specifically, they engineered a mushroom-shaped adhesive endowed with a magnetized tip, enabling rapid and reversible morphological changes through magnetic manipulation.[460] This smart adhesive operates in two modes: selective pickup and pick-and-place. In the selective pickup mode, applying an external magnetic field induces bending deformation in the tip, facilitating a switch between adhesive states (''on'' and ''off''). Conversely, in the pick-and-place mode, the external magnetic field aids in releasing the target object by initiating upward bending deformation in a micro-beam component of the tip, thereby creating an initial crack at the adhesion interface. As the edge crack propagates, adhesion weakens, leading to the instant release of the target object. Such a smart adhesive system holds promise for applications requiring precise and rapid control over movements. Another viable approach to achieving responsive adhesion involves manipulating the size of adhesive structures, which is particularly effective in wet-responsive hydrogel adhesives due to the utilization of mechanical interlocking (Fig. 20D). Park *et al.* created an innovative flexible hydrogel adhesive that dynamically reshapes in response to moisture and achieves superior adhesion in damp environments by virtue of its

Table 7 Bio-inspired and artificial strategies to control surface wetting and adhesion for SLIPs

Materials	Strategy	Stimuli	Working mechanisms	Ref.
SLIPs based on *n*-paraffin-infused organogel	Strategy VI	Thermal	When the ambient temperature surpassed the melting point (T_m) of *n*-paraffin, the *n*-paraffin within the PDMS film transitioned into a liquid phase. This liquid *n*-paraffin, which floated atop the organogel, functioned as the lubricant in the SLIPs, droplets could slide. In contrast, it tuned to solid phase under temperature below T_m, resulting in a high-adhesion Wenzel state of the water droplet	438
SLIPs based on the porous substrate with solidifiable/liquid paraffin mixture as a lubricant	Strategy VI	Thermal	By varying the proportion of solidifiable to liquid paraffin, the surface's ability to control the movement of water droplets can be adjusted between pinning and sliding at room temperature. For instance, with a ratio of 1 : 25 of solidifiable to liquid paraffin, the melting point (T_m) of these temperature-responsive SLIPs was approximately 28 °C. Consequently, as the ambient temperature rose from 22 °C to 30 °C, the droplet's behavior transitioned from pinning to sliding	439
SLIPs based on 12-HSA gelled with mineral oil	Strategy VI	Thermal	SLIPs could gel partly melt around 72 °C and form a lubricant layer covering the whole structure	440
SLIPs based on the porous substrate with thermotropic liquid-crystalline material (5CB), as a lubricant	Strategy VI	Thermal	As the environmental temperature reached 38 °C, the 5CB (liquid crystal) transitioned into an isotropic state, forming a lubricating layer on the surface. Consequently, as the temperature rose, the repellent droplets exhibited increased ease of sliding on the surface	441
SLIPs based on elastic film with inverse opal PU as substrate	Strategy VII	Mechanical	Under 42% strain, the elastic PC SLIPs experienced negative pressure in the expanded pores, causing the lubricant to retract into them. As a result, the rough surface became exposed, leading to the repellent droplet being pinned in place	442
SLIPs with anisotropic microgrooved structure	Strategy VII	Mechanical	Asymmetrically stretching the microgrooved SLIPs enables the attainment of unidirectional sliding for repellent droplets. This is facilitated by the formation of fan-shaped grooves and variations in the lubricant covering states at different ends	443 and 444
SLIPs based on PDMS + Fe_3O_4 or Co microparticles	Strategy VII	Magnetic	The orientation of SLIPs' microcilia can be altered by adjusting the orientation of the magnetic field, thereby achieving a reversible wetting and adhesion state, and thus maintaining the desired droplet mobility	445 and 446
SLIPs based on a multilayer structural substrate with shape dynamic changing under voltage	Strategy VII	Electric	Upon applying a 12 kV voltage to the SLIPs, the film experienced in-plane expansion. Consequently, the lubricant descended into the enlarged porous regions, resulting in a rough interface devoid of lubricant coverage. Consequently, the droplet became pinned to the surface	447
SLIPs based on shape-memory polymer-modified graphene sponges	Strategy VII	Electric & mechanical	Under compression, the lubricant infused into the graphene sponge is expelled, creating a smooth film of lubricant on the surface (low adhesion to droplet). When a voltage (*e.g.*, 6 V) was applied to the SLIPs, the graphene sponge regained its initial configuration through electrothermal and shape-memory effects. Consequently, the lubricant permeated the graphene sponges, causing the water droplet to adhere to the surface	448
SLIPs based on poly(3-hexylthiophene-2,5-diyl)/[6,6]-phenyl-C61-butyric acid methyl ester (P3HT/PCBM) film	Strategy VIII	Light & electric	Applying illumination can transition a water droplet from sliding to pinning. This occurs as photogenerated electrons in the light elevate the charge density of the droplet, leading to an augmented electrostatic force that immobilizes the droplet on the surface	449
SLIPs based on ZnO nanorod	Strategy VIII	Light & electric	Initially, a low voltage (2.0 V) was applied to the film in darkness. Subsequently, illumination at 80 mW cm^{-2} was introduced and then removed to regulate the motion of the droplet. This is because the wetting and adhesion states of the water droplets could transition reversibly between the Cassie state and the unstable Wenzel-Cassie state under this situation	450
SLIPs based on thermally activated magnetic field responsive surface with a thin layer of ferrofluid covered	Strategy VI	Thermal & magnetic	SLIPs could gel partly melt at high temperatures and form a lubricant layer that could respond to the magnetic field to control the movement of the repellent liquid	451
SLIPs based on microsized Ga-In LMPs, P(VDF-TrFE) copolymer & SiO_2 NPs	Strategy VIII	Near-infrared (NIR) light	The 5% LMP/P(VDF-TrFE) film experiences a rapid temperature increase to 40 °C within 50 milliseconds when exposed to NIR irradiation at 100 mW mm^{-2}. Consequently, its light-induced peak-to-peak charge density swiftly reaches up to 1280 pC mm^{-2} within 0.5 seconds, which is sufficient for droplet movement. In contrast, the temperature decreases without NIR irradiation, diminishing the thermal agitation of molecular chain. Thus, free charge on surfaces vanished and polarization were rapidly recovered	452
SLIPs based on laser-structured graphene and polyvinylidene difluoride composites (L-G@PVDF)	Strategy VI	Visible & NIR light	In the absence of light irradiation, a water droplet adheres to the paraffin due to its high surface adhesion. However, paraffin would change from solid state to liquid state upon heating. The photothermal effect of L-G@PVDF surface facilitates the conversion from high adhesion to low adhesion between water droplet and paraffin by simply exposing to light irradiation	453

Table 7 (*continued*)

Materials	Strategy	Stimuli	Working mechanisms	Ref.
SLIPs based on a porous silica-based substrate containing azobenzene groups	Strategy VII	UV light	Upon exposure to UV light at a wavelength of 365 nm, the azobenzene groups within the polymer framework underwent a conformational change from *trans* to *cis*. This transition caused a slight contraction in the porous substrate, leading to the release of silicone oil from the substrate's bulk to the swabbed surface, thereby forming a fresh lubricant layer	454
SLIPs based on microplate array (LS-MMA) with micro-groove arrays	Strategy VII	Magnetic	When subjected to a magnetic field, LS-MMA undergoes bending along the direction of the magnetic field owing to the magnetic moment present in the iron powder chain. With the continuous movement of the magnets, each microplate oscillates asymmetrically in a specific direction, resembling the motion of respiratory cilia. This movement pattern facilitates the manipulation of droplet behavior on the LS-MMA	455
SLIPs based on shape memory polymer (SMP) tube	Strategy VII	Magnetic	The asymmetrical configuration of the SMP tube, along with its internally lubricated surface characterized by remarkably low contact angle hysteresis (CAH) with most liquids, facilitates the spontaneous directional movement of droplets. Throughout this self-transportation process, the resistance originating from the magnetic-responsive gel can be dynamically adjusted by the application or removal of a magnetic field, offering an additional means of actively controlling liquid behavior	456
SLIPs based on wires coated with superhydrophobic nanoparticles and impregnated with paraffin	Strategy VI & Strategy VII	Thermal & magnetic	Upon heating, the embedded paraffin liquefies, creating a lubricant layer over the SLIPs. This mechanism mirrors the pitcher plant-inspired action, which effectively removes intricate droplets that would otherwise remain adhered to conventional superhydrophobic surfaces. On the other hand, the shape of the microwires could also be adjusted to change the wetting state of the microstructure by the lubricating layer	457
SLIPs based on PDMS coated with silicone oil	Strategy VIII	Light, electric & magnetic	Exposed to light, the functional repellent droplets containing CNT (photothermal-droplets) would show lower CA due to the lower surface tension aroused by the photothermal effect. By introducing light irradiation from single side, the droplet could keep on moving until reach dark area. Similarly, electric and magnetic fields can also be used to change the wetting and adhesion properties of functional repellent droplets such as charged droplets or magnetic droplets on the surface of SLIPs, thereby manipulating their movement behavior	458

adjustable microhook array.[140] Studies on hydrogel microhooks' structural characteristics and swelling behavior revealed that the microhooks experience directional swelling and undergo shape changes upon contact with moisture. This shape adaptation triggered by hydration notably boosts the adhesive's performance in wet conditions. Moreover, the adhesive's wet adhesion strength progressively increases with prolonged exposure to moisture. After 20 hours of swelling, the hydrogel microhook array achieves a maximum adhesion force of 79.9 N cm^{-2} in the shear direction, marking a 732.3% increase compared to dry conditions (9.6 N cm^{-2}). Therefore, wet-responsive adhesion can be achieved using simple hydrogel adhesive structures alone, without the need for extensive surface modification, by controlling humidity or water stimuli.

Strategy 3: modulating the base stiffness of substrates to adjust the adhesion of adhesive surfaces (Fig. 20E). Generally, a higher base stiffness results in a restricted contact area between adhesive structures and a rough surface, consequently resulting in a diminished adhesion force. Conversely, a lower base stiffness enables more conformal or complete contact between these structures and the surface, resulting in a relatively higher adhesion force. Taking inspiration from the climbing behavior of geckos, Li *et al.* devised a hierarchical adhesive structure aimed at achieving high and adaptable adhesion on non-flat surfaces.[393] Their adhesive, composed of three layers, mimics the epidermal adhesive structures, toe muscles, and electromyographic signals found in geckos. The structure includes a top layer with mushroom-shaped structures, a middle layer made of thermoplastic polyurethane with modulated stiffness, and a bottom layer consisting of an electrothermal film. Upon applying voltage, the temperature increases, causing the middle layer to transition from a hard to a soft state, facilitating conformal contact between the mushroom-shaped structures and the rough adherend surface. Consequently, the adhesive force is significantly enhanced, surpassing that of conventional gecko-inspired adhesives by 1–2 orders of magnitude. When the voltage is removed, the electrothermal layer returns to its original hard state, allowing for easy detachment of the adhesive from the rough surface. This controllable variation in structural stiffness, regulated by voltage, enables reversible attachment and detachment functions, holding considerable potential for applications in both industrial settings and everyday life.

Strategy 4: modulating the acting state of functional molecules to adjust the adhesion of adhesive surfaces (Fig. 20F and G). Certain adhesive molecules possess adhesion properties that adapt to changes in external environmental conditions, making

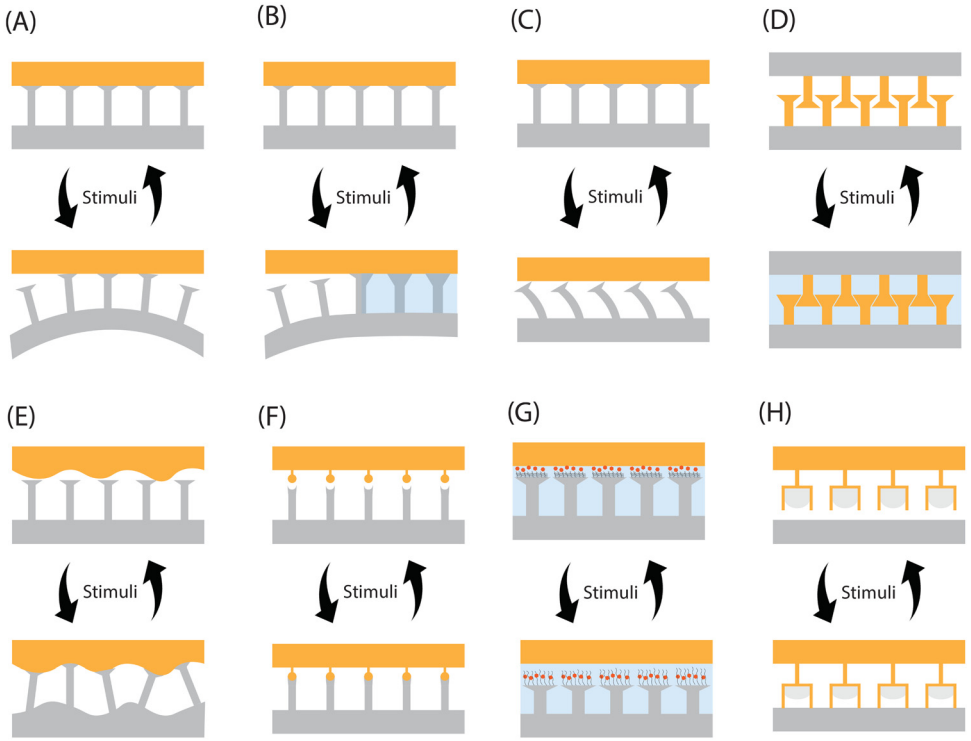

Fig. 20 Construction strategies to control surface adhesion for adhesives. (A) and (B) Modulating the physical shape of substrates, (A) no volume changes, (B) volume changes. (C) and (D) Modulating the physical shape of micro-nano structures, (C) no volume changes, (D) volume changes. (E) Modulating the base stiffness of substrates. (F) and (G) Modulating the acting state of functional molecules, (F) altering the characteristics of adhesive molecules, (G) employing different bonding molecules. (H) Modulating the vacuum level of the adhesive structure.

them ideal candidates for creating intelligent adhesives. For example, Ahn *et al.* introduced an innovative approach leveraging supramolecular host–guest chemistry to construct underwater reversible adhesion of molecular interaction-based tape-type adhesives.[461] They employed a "hook and loop (also known as "velcro")" approach to modify two types of silicon surfaces: one was functionalized with aminomethylferrocene (Fc) guest molecules to develop a "hook" configuration, and the other was functionalized with cucurbit[7]uril (CB[7]) host molecules to create a "loop" configuration (Fig. 20F). Through water disposal, the host–guest complex formation of their "velcro" exhibited remarkable adhesion strength, particularly in aqueous environments. Furthermore, reversible adhesion could be attained by altering the valence state of the Fc guests. The oxidation of Fc to Fc^+, with a significantly lower binding affinity to CB[7] compared to Fc, diminished the adhesion properties of the "velcro". Apart from directly altering the characteristics of adhesive molecules, diverse adhesion molecules can also be incorporated into the adhesive interface. This enables the modulation of adhesion force by employing different bonding molecules to fulfill the different adhesion strengths under distinct stimuli. Based on this mechanism, Zhao *et al.* devised a smart adhesive capable of switching its adhesion properties underwater.[7] Their approach integrates host–guest interaction, catechol chemistry, and a thermoresponsive polymer into a single system (Fig. 20G). At temperatures below the lower critical solution temperature (LCST), such as 25 °C, the thermosensitive polymer P(NIPAM-*co*-CD) (where CD denotes β-cyclodextrin) is water-soluble and forms a swelling layer on the surface. Consequently, the adhesive component, dopa, remains spatially confined beneath the P(NIPAM) molecules that are hydrophilic, diminishing dopa's contact area with the adherend surface. When temperatures higher than the LCST, the P(NIPAM-*co*-CD) transitions to a more hydrophobic state and undergoes agglomeration. This transition exposes the dopa group on the surface, enhancing interfacial adhesion. As a result of this mechanism, the adhesive coating demonstrates robust underwater adhesion at elevated temperatures (40 °C) but weaker adhesion at lower temperatures (25 °C).

Strategy 5: modulating the vacuum level of the adhesive structure to adjust the adhesion of adhesive surfaces (Fig. 20H). This strategy is mainly applicable to the structure of imitation octopus suckers. It is known to all that octopus suckers rely on the pressure difference between the inside and outside of the sucker to achieve adhesion. Therefore, by regulating these pressure variances, we can achieve adjustable adhesion. For instance, Wang *et al.* introduced an innovative design inspired by the octopus, aiming to emulate both the morphology and muscle-like actuation of its suckers to create a highly adaptable adhesive.[66] This smart adhesive comprises two cavities divided by a flexible membrane: the upper cavity contains magnetic particles, while the lower one remains empty. By manipulating an external magnetic field, the deformation of the elastic membrane can be controlled, thereby altering the volume of

the cavity and inducing variable adhesion through pressure changes. The versatility of this adhesive was demonstrated through applications such as transfer printing and manipulation of diverse surfaces, showcasing its potential for deterministic assembly and utilization in both dry and wet conditions for industrial or robotic tasks.

The five strategies outlined above serve as fundamental approaches for creating stimulus-responsive adhesives (achieve bonding through physical interactions) with controllable adhesion behavior for solid–solid and solid–liquid–solid adhesion systems. While specific examples have been provided for each construction strategy to enhance reader understanding, it is important to acknowledge that beyond the covered stimulus types, various other stimuli have also been utilized employing similar methodologies. Additionally, we have assembled a comprehensive summary in Table 8, highlighting the key stimulus-responsive adhesives employed for manipulating adhesion behavior in recent studies. This table encompasses pertinent details including composition, construction methodologies, types of stimuli employed, and associated operational mechanisms.

8.2.2. Tunable adhesion based on reversible covalent bonds. Traditionally, covalent bonds are regarded as one of the strongest bond types, requiring substantial energy for disruption once formed. Consequently, due to their perceived irreversibility, covalent linkages in polymeric adhesives have been viewed as "fixed." However, it's noteworthy that under specific conditions (*e.g.*, catalytic presence and elevated temperatures), covalent bonds can undergo exchange (referred to as reversible covalent bonds), exemplified by reactions like transesterification or disulfide exchange.[472] Such reactions fall under the purview of dynamic covalent chemistry (DCC).[473] This part delves into various polymeric adhesives leveraging associative and/or dissociative DCC (Fig. 21), the former encompassing processes such as transesterification, transimidation, borate transesterification and transalkylation, the latter involves reactions such as disulfide metathesis, thiol–ene reaction, Diels Alder reaction, and amino formic acid ester exchange, to illustrate their efficacy in switchable adhesives.

8.2.2.1. Associative dynamic covalent chemistry for constructing switchable adhesives. In the context of associative dynamic covalent bond exchange, the process involves simultaneous breaking and reformation of bonds (Fig. 21A). Despite bond activation, the macromolecular connectivity (topology) experiences minimal alteration due to the relatively constant bond density.[474] Below, we delve into several reversible polymer adhesives utilizing associative DCC, which encompass transesterification, transimination, boronic ester exchange, and transalkylation.

Switchable adhesion based on transesterification. Transesterification is a chemical process involving the exchange of ester and alcohol groups, typically requiring high temperatures (>100 °C) and catalysts like Lewis acids or strong Brønsted bases.[475] This reaction is characterized by the retention of network bonds and crosslinks throughout its progression. Unlike traditional dissociative reactions, transesterification involves simultaneous bond dissociation and re-association, placing it within the category of associative dynamic covalent chemistry. In recent years, polyester-based epoxy materials have gained prominence in adhesive applications. For instance, Hao *et al.* developed a repairable and removable adhesive with a high lignin content (>47 wt%).[476] This adhesive is produced by curing polyethylene glycol diglycidyl ether with modified Kraft lignin functionalized with –COOH groups under the action of the zinc catalyst. Notably, this adhesive exhibits rapid stress relaxation at high temperatures, ensuring exceptional self-healing capabilities within 15 minutes. Additionally, due to its swelling properties, the adhesive can be easily removed from tin plates in low-concentration NaOH solutions (0.01–0.1 M).

Switchable adhesion based on transamination. The imine bond arises from the classical organic reaction known as the "Schiff base reaction". This bond forms through a condensation reaction between an amine and an aldehyde, yielding an imine compound. Functioning as a dynamic covalent bond, the imine bond frequently shows the self-healing attributes of numerous materials. Due to the mild conditions required for imination and transimination, and the controllable kinetics achievable through stimuli such as temperature, moisture content, and pH alterations, diverse adhesive materials can be tailored. Park *et al.* synthesized a hydrogel adhesive comprising polyallylamine-hydrocaffeic acid (PAA-CA) to introduce catechol moieties into the PAA structure.[379] By adjusting the pH, PAA-CA hydrogels were formulated to engage in dynamic imine bond formation *via* the Schiff base reaction, without the need for additional crosslinkers. Under mildly acidic conditions (pH = 5.5), dissociation of the imine bonds within the PAA-CA hydrogel weakens the crosslinking, resulting in lower wet adhesion strength ($\sim$3.1 kPa) compared to dry conditions ($\sim$3.6 kPa). However, at neutral conditions (pH = 7.4), the adhesion strength significantly increases, reaching approximately 17 kPa, representing a 4.6-fold enhancement relative to dry conditions, owing to the formation of imine bonds at neutral pH.

Switchable adhesion based on boronic ester exchange. Five-membered ring boron esters are synthesized *via* the esterification of 1,2-diol and boric acid in an aqueous environment, ultimately forming compounds with a trigonal planar structure. Rahman *et al.* have presented an innovative approach to developing robust, reversible, and recyclable adhesives by integrating dynamic covalent bonds of boronic ester into standard triblock thermoplastic elastomers (polystyrene-*b*-poly(ethylene-*co*-butylene)-*b*-polystyrene, referred to as SEBS), which can bind reversibly with various fillers and substrates.[477] In their study, a dynamic covalent linkage was successfully formed between silicon dioxide nanoparticles (SiNP) and boronated SEBS triblock copolymer (S-Bpin). Notably, the SiNP S-Bpin compound, containing 20 wt% SiNP, exhibited strong adhesive properties on surfaces composed of aluminum, steel, and glass. Therefore, dynamic boronic acid esters offer an appealing bonding mechanism for adhering to fillers or surfaces featuring hydroxyl functional groups.

Switchable adhesion based on transalkylation. Transalkylation refers to a chemical process where an alkyl group is

Table 8 Bio-inspired and artificial strategies to control surface adhesion for adhesives that achieve bonding through physical interactions

Materials	Strategy	Stimuli	Working mechanisms	Ref.
Polyethylene glycol (PEG) hydrogel with bioinspired micropillar arrays	Strategy 2	Humidity/ water	The biomimetic microstructure facilitates precise and uniform contact with target surfaces, whereas the PEG polymer absorbs moisture at the interface, promoting capillary adhesion aroused by hydrogel pillar expansion	280
Mushroom-shaped PDMS pillar arrays integrating the Fe_3O_4 nanoparticles coated with PNIPAM	Strategy 4	NIR light	PDMS pillars integrated with nanoparticles exhibit excellent responsiveness to near-infrared (NIR) radiation. When NIR light is applied, the localized increase in surface temperature leads to the dehydration of the adhesive, exposing its functional groups	57
Gecko-inspired adhesive with elastomeric micropatterns containing magnetic microparticles	Strategy 2	Magnetic	The micropillars exhibited bending and rotational motion around their axes as the magnet approached and moved around the sample. With stronger field gradients, increased bending and contact between the pillars, or between the upper part of the pillar and the backing layer of the array, were observed depending on the bending direction of the pillars. Upon removal of the magnet, the pillars reverted to their initial positions	462
PDMS matrix dispersed with iron oxide particles	Strategy 3	Magnetic	When a magnetic field is only introduced during the preload phase of a standard adhesion test cycle, the magnetically controlled dry adhesive system's rigidity would be enhanced, leading to reduced adhesion strength. Conversely, if the magnetic stimulus is only active during the peeling phase, the increased stiffness of the backing layer aids in preventing peeling, thus improving the adhesive strength	463
PDMS mushroom-like adhesive structure supported by an electrically active liquid crystal elastomer	Strategy 1	Electric	When a voltage is applied, the electrothermal effect generates heat, causing the LCE film to contract. This contraction results in the bending deformation of the adhesive structure, which decreases the contact area between the adhesive structure and the opposing surface, leading to reduced adhesion. Upon removing the voltage, the contraction of the LCE film stops, allowing the hierarchical structure to return to its original shape, thereby restoring high adhesion	464
Mussel-inspired copolymer coating-decorated mushroomed pillars with the thermal-responsive hydrogel layers	Strategy 1	Thermal	Utilizing the thermal-responsive curving mechanism of the adhesive, it can curl downwards to firmly grasp substrates, achieving strong attachment when below the LCST and resulting in high adhesion (high contact area between adhesive structures and adherend surface). Conversely, it curls upwards to enter the detachment state, resulting in low adhesion (low contact area between adhesive structures and adherend surface)	345
Polyurethane (PU) as the backing layer and graphene/shape memory polymer (GSMP) as the pillar array	Strategy 2	UV light	Under UV irradiation, the photothermal effect of graphene alters GSMP micropillars to a viscoelastic state, facilitating seamless contact on surfaces of varying roughness. The microstructure array can switch between states with different adhesion strength by controlling UV "on" and "off"	337
Graphene/PDMS composite (GP) as the backing layer and PDMS as the micropillar array	Strategy 2	UV light	Under UV irradiation, graphene leverages its photothermal properties to warm the micro-pillars, which alters the conformation of the PDMS molecular chains, thereby increasing the number of adhesive areas with the substrate. This increase in adhesive areas, along with the reorganized arrangement of the PDMS chains, contribute to significantly higher adhesion compared to conditions without UV irradiation	465
PDMS micropillar arrays with MoO_{3-x} quantum dots	Strategy 2	NIR light	A temperature gradient is created due to the near-infrared irradiation to MoO_{3-x} quantum dots, resulting in the un-uniform expansion and eventually appears as a curling structure. Based on this, the contact area is reduced, causing the decreased adhesion or even detachment	466
Channeled poly(*N*-isopropylacrylamide) (PNIPAm) hydrogel containing bio-inspired dopamine-comonomers	Strategy 4	Thermal	Beyond the lower critical solution temperature (LCST), PNIPAm transitions into a hydrophobic state, aiding in water removal from the interface and facilitating stronger adhesion to the glass surface through hydrogen bond formation by the catechol groups. Conversely, at room temperature, the hydrated hydrophilic PNIPAm chains repel the substrate surface, leading to a significant reduction in adhesion strength. This interplay between the catechol groups and channeled structures significantly enhances switching efficiency and adhesion strength	467
Cu^{2+}-curcumin-imidazole-polyurethane (CIPUs:Cu^{2+})	Strategy 4	NIR light & alcohol	Upon exposure to NIR light, CIPUs:Cu^{2+} absorb the light, converting it into heat. This heat disrupts the metal–ligand coordination bonds between segments, resulting in the loss of adhesion ability on the substrate surface. Once the NIR light source is deactivated, the substrate can be re-bonded using a heat-cool method, restoring the adhesive properties. Similarly, when alcohol is applied, it dissolves the weaker metal coordination bonds and causes the molecular segments to swell, resulting in a rearrangement of the polymer network structure. This leads to reduced adhesion between the polymer and the substrate	468
Adhesive based on side-chain crystalline polymers and self-adhesive polymers (tetradecyl acrylate/octadecyl acrylate)	Strategy 3	Thermal	Crystalline polymers with side chains can melt and recrystallize reversibly in response to temperature changes. This property enables the material to transition between high and low adhesive strengths by altering its flexibility (stiffness) and thus changing the contact area with the substrate at different temperatures	469
Skin-adhesive patches with PDMS-based 3D microtips and polyurethane-based microsuckers	Strategy 5	Vacuum	The PU-based elastomer, known for its flexibility, yielded a microsuction cup array adaptable to varying pressures. Upon the application of a gentle load, the height of the microsuckers decreased, enhancing their ability to conform to rough surfaces effectively	51

Table 8 (*continued*)

Materials	Strategy	Stimuli	Working mechanisms	Ref.
Gecko-inspired elastomeric microfibrillar adhesive membrane supported by a pressure-controlled deformable gripper body	Strategy 5	Vacuum	The adhesive strength could be managed by adjusting the internal pressure and leveraging the principles of uniform load distribution across interfaces. This flexible adhesive device maximizes the bonding potential of the fiber membrane, achieving an adhesive efficiency of about 26%, representing a 14-fold increase compared to the adhering membrane without load sharing	71
Microstructured shape memory polymer	Strategy 2	Thermal & Mechanical	This was accomplished by capitalizing on the bulk material characteristics of SMP and surface microstructuring. The remarkable reversible adhesive performance is credited to the SMP's ability to change rigidity based on temperature and its capacity for temporary shape locking of adhesive microstructures, along with permanent shape recovery between flat and microtip configurations	470
Multilegged LCN (liquid crystal network)-based gripper with gecko-inspired adhesive pillars	Strategy 1	Thermal	As temperature rises, the LCN cantilever bends upward, leading to a reduction in the contact area between the bonding structure and the adhered surface, consequently decreasing the adhesion force. Conversely, as temperature decreases, the LCN cantilever returns to its initial shape, increasing the contact area between the bonding structure and the adhered surface, thus enhancing the adhesion force	471

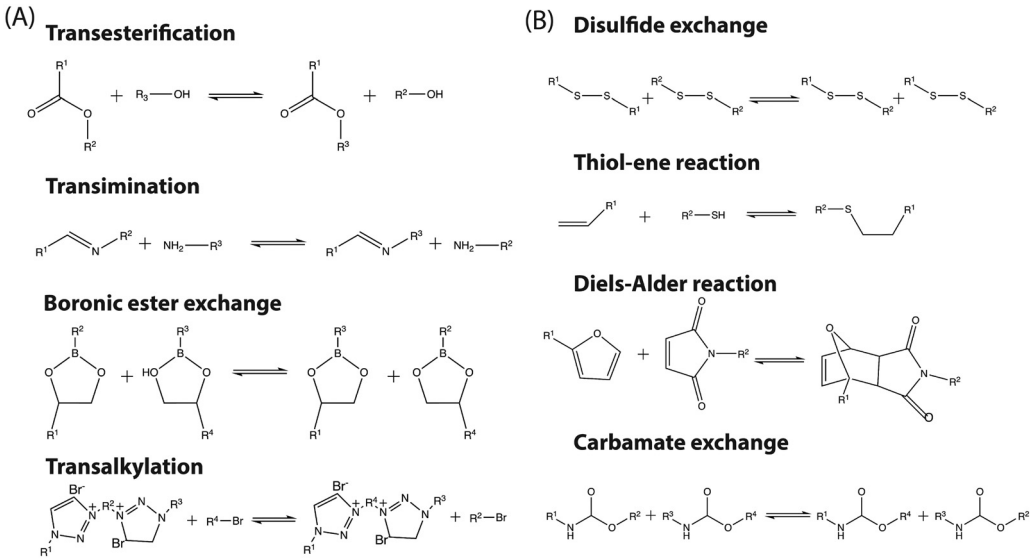

Fig. 21 Exchange reactions in dynamic covalent chemistry with associative and dissociative exchange mechanisms, for switchable adhesives based on reversible covalent bonds. (A) Associative dynamic covalent chemistry for reversible adhesives, including transesterification, transimidation, borate transesterification and transalkylation. (B) Dissociative dynamic covalent chemistry for reversible adhesives, such as disulfide metathesis, thiol–ene reaction, Diels Alder reaction, and amino formic acid ester exchange.

transferred from one compound to another. This reaction is often utilized to employ the alkyl group as a blocking agent prior to subsequent steps in a synthesis. An illustrative example of transalkylation involves the crosslinking of poly(1,2,3-triazole) with an alkyl halide, resulting in the formation of an ionic liquid polymer network known as polytrizolium. Oh *et al.* have engineered dual-crosslinked thermosetting material composed of phenyl-based linkers (irreversible network) and 1,2,3-triazolium units (reversible network), which shows reversibility and triggered debonding characteristics.[478] The reversible part exhibits high rigidity at room temperature and becomes soft due to dissociation at higher temperatures. Consequently, a covalent exchange of alkyl chains ensues, facilitating the reshuffling of the entire network upon heating. On the other hand, the latter unit undergoes self-immolation into smaller fragments through sequential 1,4-eliminations triggered by a molecular signal, inducing orthogonal and selective de-crosslinking of the thermosets. These thermosets exhibit stimulus-responsive properties as polymer adhesives. Upon gluing glass pieces, they demonstrate high adhesive strength and can be rejoined upon heating after detachment. However, exposure to a molecular signal drastically reduces adhesion under mild conditions, leading to effortless detachment.

8.2.2.2. Dissociative dynamic covalent chemistry for constructing switchable adhesives. Unlike the associative covalent exchange, the dissociative dynamic covalent chemistry involves the initial debonding within the polymer chain triggered by stimuli, followed by the subsequent re-bonding or exchange reaction (Fig. 21B). In this pathway, bond exchange may lead to

a reduction in the polymer's crosslink density and a weakening of its physical properties.[479] To illustrate the versatility of dissociative dynamic covalent bonds in crafting switchable adhesives, various examples such as disulfide metathesis, the thiol–ene reaction, the Diels–Alder reaction, and carbamate exchange are introduced.

Switchable adhesion based on disulfide metathesis. The disulfide bond represents a dynamic covalent linkage that readily undergoes cleavage and reformation under mild conditions. Due to the low energy properties of disulfide bonds, they can easily engage in exchange reactions with disulfide bonds under photoinitiation or room temperature, through radical and thiosulfate anion pathways.[480] Pierre *et al.* introduced a novel reversible and self-healable adhesive based on a polybenzoxazine (poly(CAR-4apds))-based thermoset incorporating disulfide bonds and cardanol.[481] A notable feature of this adhesive is its low activation energy ($\sim$64 kJ mol^{-1}) and rapid stress relaxation process, which maintains an adhesive strength of up to 2 MPa on aluminum surfaces even after five repair cycles and enables rapid self-healing at lower temperatures. In addition, compared to previous studies, the activation energy for the disulfide bonds in poly(CAR-4apds) ($\sim$55 kJ mol^{-1}) is significantly lower than that observed in the epoxy ester exchange process ($\sim$88 kJ mol^{-1}), representing a reduction of approximately 70%. Moreover, owing to the relatively low E_a of disulfide bond exchange, the topology freezing transition temperature (T_v) of poly(CAR-4apds) was validated to be -8.5 °C, below the T_g (40 °C) of poly(CAR-4apds), thus facilitating the reversible adhesion of this thermoset.

Switchable adhesion based on the ene–thiol reaction. In the ene–thiol reaction, thiols (HS–R′) and olefins (C═C–R) react under the condition of light exposure, effectively forming thioethers (R–C–C–S–R′). These thiol–ene couplings have found extensive application in polymer crosslinking due to their swift reaction kinetics and minimal sensitivity to O_2. For instance, Cheng *et al.* demonstrated the feasibility of light-induced, radical-mediated dynamic bonding in thiol–ene elastomer adhesives, termed photo-CANs.[482] The dynamic behavior arises from the inherent flexibility of sulfide bonds with free radicals. The elastomers are covalently bonded without the irradiation of UV light, and show high stability, minimal creep, low hysteresis, as well as exceptional temperature tolerance. In contrast, the elastomer become flowable and show self-healing behavior after exposing to UV light. The reversible process can be repeated over 180 cycles. Remarkably, the adhesion strength of the elastomer decreases under UV exposure compared to its non-illuminated state, with minimal variation in peeling displacement. This design approach for reversible adhesives could be utilized in the creation of ene–thiol crosslinked elastomers, accommodating a diverse range of vinyl groups and backbone chemistries.

Switchable adhesion based on Diels–Alder reaction. The Diels–Alder reaction involves the formation of a six-membered ring between a diene and a dienophile through a concerted reaction. This reaction, particularly between furan as a diene and maleimide as a dienophile, has found diverse applications in dynamic covalent bond exchange due to its mild reaction conditions and high yield. For example, Wu *et al.* incorporated dynamic covalent bonds into polyurethane backbone to develop hot melt adhesive (CDI-PUR-DA). The Diels–Alder adducts were cleaved when temperature is over 110 °C, resulting in the decrease of viscosity ($\sim$4 Pa s).[483] Conversely, upon cooling, the viscosity reverted to its initial value owing to the reformation of the Diels–Alder adducts. Moreover, the introduction of smaller size of urea-furan dimers could further improve the adhesion strength, indicating urea-furan dimers play a crucial role as chain extenders in (retro-)Diels–Alder reactions.

Switchable adhesion based on carbamate exchange. Due to the hydrogen bonding of carbamate and the semicrystalline structure among component segments, carbamate has found versatile applications. The isocyanate group becomes active with rising temperatures because it is shielded by an oxime-urethane bond. This characteristic allows for the separation of oxime and isocyanate. As a result, polyurethane (PU) containing oxime demonstrates adhesion strength similar to that of crosslinked ones at room temperature, and behaves like thermoplastic PU when heated. For instance, by leveraging the properties of thermoset (PUR)-HMAs and TPU-HMA, Wang *et al.* developed dynamically crosslinked PU hot-melt adhesives (DPU-HMA) through the incorporation of reversible oxime-carbamate bonds.[484] The effectiveness of this approach was further validated through lap shear tests. The adhesion strength of DPU-HM, after curing for different time (5 minutes and 1 day), was notably superior to that of commercial adhesives. Moreover, oxime-PU displayed an ultimate adhesion strength of 9.02 $\pm$ 1.36 MPa (10 days of curing), with repeated adhesion strengths maintained above 4.40 $\pm$ 0.92 MPa even after undergoing four cycles of detachment, akin to hot-melt TPU.

The described reactions provide primary methods for developing intelligent adhesives using reversible covalent bonds with adjustable adhesion properties. Apart from the research mentioned above, there exist additional instances of fabricating reversible adhesives utilizing dynamic covalent chemistry, which we haven't covered in this work. Moon *et al.* have compiled a comprehensive summary of related endeavors, which individuals keen on exploring further can consult.[473]

9. Applications

As outlined earlier, through the implementation of nature-inspired principles in designing surface structures and/or chemicals, engineered adhesive surfaces have demonstrated remarkable capabilities in adaptable and controllable adhesion. Biomimetic adhesive surfaces have garnered significant attention across various fields, encompassing a wide range of liquid-related applications such as self-cleaning, functional textiles, droplet manipulation, microfluidics, solar evaporation, and water collection, as well as solid-related applications including adhesives, bioelectronics, sensors, soft grippers, soft robots and tissue engineering.[6,11,12,261,485] In this section, we focus on emerging applications in fields such as

Fig. 22 Various applications of bioinspired adhesives. Typical applications include soft robots (climbing robots, soft grippers), wearable devices (sensors, electronic skins), droplet manipulation (pipetting devices, fog collection) and biomedical engineering (wound dressing, drug delivery), *etc.* The picture of the climbing robot is reproduced with permission from ref. 486 Copyright 2007, IEEE Xplore. The picture of the soft gripper is reproduced with permission from ref. 487 Copyright 2021, Wiley-VCH. The picture of the sensor is reproduced with permission from ref. 488 Copyright 2017, Wiley-VCH. The picture of the electronic skin is reproduced with permission from ref. 489 Copyright 2021, Elsevier Ltd. The picture of the fog collection is reproduced with permission from ref. 490 Copyright 2016, Wiley-VCH. The picture of the pipetting device is reproduced with permission from ref. 448 Copyright 2017, AAAS. The picture of the drug delivery is reproduced with permission from ref. 491 Copyright 2022, AAAS. The picture of the wound dressing is reproduced with permission from ref. 492 Copyright 2020, AAAS.

droplet manipulation, climbing robots, soft grippers, wearable electronics, and biomedical engineering, among others (Fig. 22).

9.1. Droplet manipulation

The directional motion of droplets, especially on a microscale, holds significant importance across various applications such as sensors, directional self-cleaning, and microfluidic devices, garnering increasing attention.[396,426,493,494] Typically, the directional motion of droplets relies on the difference in interfacial adhesion force on different sides of the liquid droplet, which is induced by gradients of surface-free energy and Laplace pressure.[495–497] Advancements in superwettability surfaces, encompassing liquid-infused surfaces, superhydrophobic surfaces, hydrophilic surfaces, and wettability-patterned surfaces, have led to the development of surfaces with dynamic wetting and adhesion properties.[498–501] Notably, slippery liquid-infused porous surfaces exhibit a superior performance for timely and *in situ* control of droplet motion behaviors among these surfaces. Leveraging structured biomimetic SLIPs capable of switching between slippery and nonslippery states, precise and timely control over droplet motion can be achieved. Herein, we will discuss various applications, such as chemical microreactions employing controllable mixing processes, pipetting devices with timely extrusion mechanisms, and high-efficiency fog collection systems, developed based on SLIPs.

Bio-inspired slippery liquid-infused porous surfaces (SLIPSs) have garnered considerable interest due to their notable features such as liquid repellence, self-cleaning capabilities, and low contact angle hysteresis (CAH), rendering them suitable for various liquids, including those ranging from high to low surface energy, and finding utility in chemical microreactions. For instance, Guo *et al.* achieved controllable manipulation of droplets and bubbles on amphibious slippery gel surfaces created by integrating magnetically responsive iron/poly(dimethylsiloxane) (Fe/PDMS) gel films with silicone oil.[408] These surfaces exhibit magnetic responsiveness and demonstrate minimal resistance forces with water droplets in the air and bubbles underwater, while showing strong affinity to bubbles underwater, thus possessing amphibious characteristics. Under the influence of a pulsing magnetic field, the amphibious slippery gel surface enables the controlled sliding of water droplets and bubbles.

It's noteworthy that unlike traditional SLIPS, this gel-based SLIPs demonstrates robust cyclic performance (>100 cycles) in both air and water environments. This durability primarily stems from the outstanding dispersion capability of lubricant layer. Unlike prior SLIPs designs, where the lubricating layer liquid could only be dispersed within the physical pores of the main material, in this system, silicone oil can be evenly distributed within the cross-linked PDMS network for storage. Leveraging the responsive SLIPs' excellent control over droplets on it, it can function as a microreactor to regulate droplet-based localized chemical reactions (Fig. 23A). For example, in their study, a 2.5 μL droplet (0.05 M pyrocatechol, designated as droplet A) was initially deposited on the responsive SLIPs and pinned at the magnet's edge. Subsequently, another 2.5 μL droplet (0.05 M $FeCl_3$, designated as droplet B) was introduced onto the surface, and the local magnetic field strength at the location of droplet B was adjusted to guide droplet B to move toward droplet A until the two droplets made contact. Upon contact, droplets A and B underwent a chemical reaction and merged to form a new droplet, designated as droplet C. Once the magnetic field at the location of droplet C is removed, it will slide off the SLIPS surface due to reduced friction. In addition to manipulating the chemical reactions of droplets in air environments, this responsive SLIPs could also control the mixing of bubbles underwater through its excellent amphibious property, thus broadening its potential applications in gas–liquid microreactors.

In addition to microreactors, responsive SLIPs can also be integrated into pipetting devices to facilitate the manipulation of liquid transport patterns, including on/off switching, speed control, and directional changes. These pipetting devices streamline liquid handling tasks in microplates and microarrays, which are typically time-consuming and labor-intensive, particularly in applications such as practical blood grouping

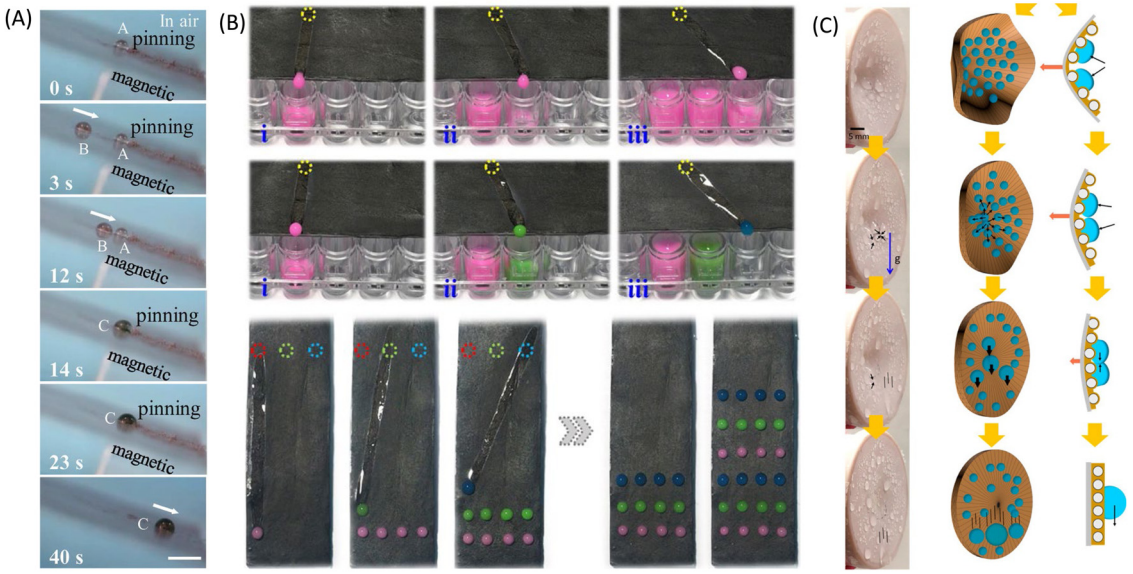

Fig. 23 Bioinspired adhesives for droplet manipulation. (A) Responsive SLIPs serve as microreactors. The picture is reproduced with permission from ref. 408 Copyright 2019, Wiley-VCH. (B) Responsive SLIPs serve as pipetting devices. The picture is reproduced with permission from ref. 502 Copyright 2018, AAAS. (C) Responsive SLIPs used for collecting water and fog in the air. The picture is reproduced with permission from ref. 444 Copyright 2017, American Chemical Society.

diagnosis. For example, Wang *et al.* utilized paraffin as a lubricant to infuse structural graphene film, creating programmable switchable SLIPs.[502] This film, leveraging graphene's photothermal property, exhibited controllable patterned wettability. Upon exposure to masked near-infrared light, the paraffin transitioned from a solid to a liquid state, enabling programmable and dynamically controlled motion paths for droplets (Fig. 23B). Through this meticulously designed thermoresponsive pathway, repellent droplets could be precisely and reversibly directed to the desired destination on demand, minimizing the risk of cross-contamination. This photocontrollable droplet manipulation device serves as a versatile platform for pipetting droplets. Similarly, the researchers further enhanced the graphene sponge with a shape-memory polymer, incorporating lubricant to produce electrothermally switchable SLIPs.[448] On these switchable SLIPs, the motion behavior of repellent droplets could reversibly transition between sliding and pinning upon the application of pressure or voltage, respectively. Leveraging this mechanism, a multichannel pipette was integrated to accurately dispense liquids onto target microplates. Notably, there were no residual repellent liquids left on the surface of the switchable SLIPs. Consequently, the array of switchable SLIPs possessed the capability to efficiently pipette different samples without the risk of contamination. This multichannel pipette eliminates the need for complex operations and the consumption of pipette tips or pins, greatly simplifying the liquid manipulation process.

Utilizing the gradient distribution of surface structures to collect water and fog in the air and directing the motion behavior of droplets for fusion are previous research focal points, which have shifted to responsive SLIPs currently.[503–505] For instance, a series of bioinspired structural surfaces have been engineered by mimicking the micro- and nanostructures and the wettability of various species to achieve fog collection. Examples include spider silk-inspired fibers,[506] desert beetles-inspired hydrophilic/hydrophobic patterned surfaces,[507] cactus-inspired surfaces with gradient wettability,[508] petals-inspired conical lamella,[509] pitch plant-inspired slippery surfaces,[510] and cross-species-inspired slippery surfaces.[511] A notable advantage of employing responsive SLIPs over previous structural surfaces for fog collection lies in their programmable nature, offering the potential for high collection efficiency. Researchers can optimize fog harvesting rates by dynamically adjusting the switching patterns of responsive SLIPs in real time based on environmental conditions. For example, Wang *et al.* achieved high-efficiency water collection using a mechanically stretch-responsive SLIPs.[444] Under strong wind, their film underwent concave deformation, causing captured droplets to be pinned and coalesce on the surface (Fig. 23C). Consequently, the water droplet size increased and was shed to the collector, enhancing water collection efficiency. Specifically, when wind speeds exceeded 11 m s^{-1}, the tensile stress-responsive SLIPs realized more than double the water collection efficiency compared to passive control by strong wind. This result highlights that active and programmable control of external stimuli promises higher fog collection efficiency with environmental adaptability. Similarly, Huang *et al.* developed magnetic field-responsive SLIPs with a micropillar array for programmable fog harvesting.[490] When the micropillars were upright, their tips faced the fog, facilitating rapid water collection. Once the droplets on the micropillars reached a certain size, external magnetic fields could bend the micropillars, removing the droplets. Therefore, efficient fog harvesting can be achieved by optimizing the programming of magnetic-responsive SLIPs based on actual

fog conditions. By adjusting wetting states and programming patterns of responsive SLIPs in response to environmental factors such as wind direction and speed as well as fog humidity, fog harvesting efficiency can be further optimized in real time.

9.2. Climbing robots

As the demand for non-horizontal operations has risen in recent years, there's a pressing need for climbing robots capable of scaling vertical walls and even inverted ceilings. However, the usability of conventional climbing robots, such as wheeled and magnetic adhesion types, is often constrained by the wall's slope and surface material. By leveraging the strong adhesion properties of biomimetic adhesives, climbing robots employing biomimetic adhesion mechanisms could securely attach to walls made of different compositions, significantly expanding their potential applications (Fig. 24A).[512] Some studies indicate that wheel-legged and tracked climbing robots equipped with mushroom-shaped arrays show promise for scaling vertical surfaces.[11,513,514] However, due to constraints in their movement models, these types of climbing robots are not widely adopted. Legged robots, in comparison to wheeled and tracked variants, offer greater flexibility. They inherently possess a safety margin: if one leg loses adhesion, the remaining legs can still support the robot on the surface. Moreover, legged robots adhere to the wall surface discretely, allowing them to navigate defects or cracks in the wall. This enhances their adaptability and widens their range of applications.

For example, Stickybot, a quadruped climbing robot, utilized gecko-inspired switchable adhesive surfaces with anisotropic microstructures to climb smoothly on vertical surfaces (Fig. 24B).[515] However, due to its limited degrees of freedom, it could only ascend. Consequently, during the design process of Stickybot III, integrated ankles with roll and yaw flexures to enable steering.[518] On the other hand, Abigaille II, a lightweight hexapod climbing robot inspired by spiders, employed isotropic microstructures to generate adhesion force, enabling movement across vertical surfaces.[519] Nevertheless, its climbing speed on such surfaces was restricted to a mere 0.1 cm s^{-1}, and vibrations during climbing could compromise adhesion. Thus, Abigaille III, an upgraded version, has enhanced overall construction and control systems, maintaining the dexterity of Abigaille II on flat vertical walls while also climbing stably on uneven surfaces.[520] Additionally, a tendon-supported structure was implemented to evenly distribute stress at contact interfaces, enhancing adhesive properties and load-bearing capabilities. By recognizing the adaptability of tree frog-inspired wet adhesives to moist conditions, He *et al.* introduced an adhesive surface featuring quadrilateral smooth micropillars.[355] This surface was successfully applied to a hexapod climbing robot design and facilitated climbing on slopes exceeding 80°. However, limitations in the design of adhesive foot modules hindered these legged robots from climbing on inverted ceilings. One potential solution involves utilizing soft materials as the supporting layer of adhesive foot modules. For instance, Ko *et al.* developed the UNIclimb, a gecko-inspired four-legged robot, with stable climbing capabilities on both vertical surfaces and inverted ceilings.[521] Employing a thick sponge layer in multilayered adhesive foot modules allowed conformal contact against contact interfaces of varying orientations and roughness. This layer also functioned as a shock absorber, reducing shock from actuators and enhancing

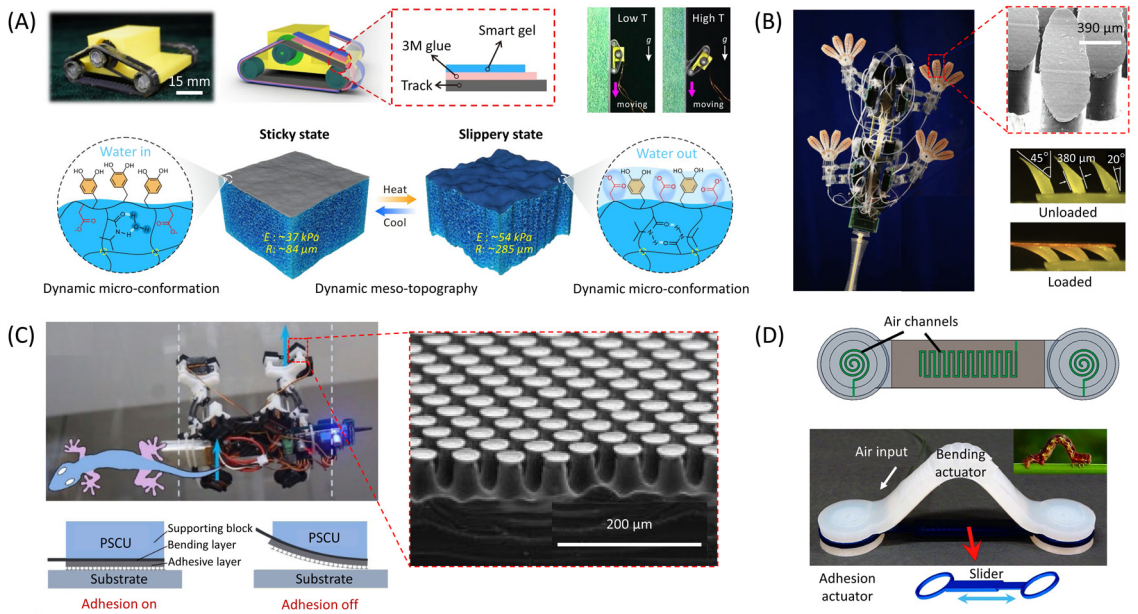

Fig. 24 Bioinspired adhesives used for climbing robots. (A) Mussel-inspired hydrogel adhesives for tracked climbing robots. The picture is reproduced with permission from ref. 512 Copyright 2022, Springer Nature. (B) Gecko-inspired micro-structured adhesives for legged climbing robots. The picture is reproduced with permission from ref. 515 Copyright 2008, IEEE. (C) Soft–hard–soft sandwiched composite adhesive structure for a legged climbing robot. The picture is reproduced with permission from ref. 516 Copyright 2022, Springer Nature. (D) The picture is reproduced with permission from ref. 517 Copyright 2018, Mary Ann Liebert Inc.

climbing performance. Similarly, Li *et al.* utilized foam as a support structure within the layered adhesive design (employing a soft–hard–soft configuration) for a ceiling-mounted inverted walking robot. This design aids in evenly distributing the load and providing shock absorption (Fig. 24C).[516]

Regrettably, conventional mechanical climbing robots, due to their large size, struggle to navigate confined spaces, particularly narrow environments. Conversely, soft robots utilizing bio-inspired adhesives, owing to their compactness and flexibility, excel in performing transfer operations in such cramped conditions. For instance, Wang *et al.* incorporated graphene into PDMS to create photothermal actuation effects, resulting in a light-driven soft robot based on gecko-inspired triangular arrays.[69] This robot showcased stable movement capabilities even while carrying loads exceeding 50 times its own weight. However, due to the inherent limitations, integrating complex mechanisms into small soft robots poses challenges. Consequently, the gecko-inspired adhesives in this robot struggle to achieve substantial effective contact areas and uniform stress distribution, limiting its ability to climb slopes steeper than 30°. Tang *et al.* innovatively introduced a novel design of a pneumatic-actuated bioinspired soft adhesion actuator, combining octopus-inspired suckers with inchworm locomotion (Fig. 24D).[517] This actuator, featuring extremely soft bilayer structures with an embedded spiral pneumatic channel, operates on both land and underwater surfaces. Unlike traditional adhesion actuators, which rely on suction, this design employs pneumatic inflation to create negative pressure, enabling strong and rapid reversible adhesion on various smooth surfaces. Leveraging this switchable adhesion mechanism, an innovative load-bearing amphibious climbing soft robot (ACSR) was developed, incorporating a soft bending actuator. The ACSR exhibited exceptional versatility, operating on a wide array of horizontal and vertical surfaces, both dry and wet, on land and underwater. Impressively, it can transport objects weighing up to 200 grams, over five times its own weight, and achieves a vertical climbing speed of approximately 286 mm per minute, both on land and underwater. This speed corresponds to crawling 1.6 times its body length per minute. The groundbreaking research expands the capabilities and versatility of soft robots, particularly in tasks such as window cleaning and underwater inspection in challenging environments. Furthermore, Zhang *et al.* introduced a multimodal soft crawling-climbing robot (SCCR) inspired by inchworms, capable of achieving various locomotion modes by synchronously controlling body deformation and foot friction forces.[522] The SCCR utilized three bending fiber-reinforced pneumatic artificial muscles (PAMs) in series to mimic the inchworm's characteristic "Ω" deformation. By manipulating the quasi-static deformation shapes of the PAMs and the anchoring status of the suckers, the SCCR could achieve different locomotion gaits. Notably, it achieved speeds of up to 21 mm s^{-1} (0.11 body length s^{-1}) and could carry a payload of 500 g (about 15 times its weight) on plastic horizontal surfaces. Additionally, it demonstrated the ability to climb vertical walls at a speed of 15 mm s^{-1} (0.079 body length s^{-1}) while carrying a 20 g payload. More importantly, this SCCR could also showcase diverse locomotion capabilities in aquatic environments.

9.3. Soft grippers

Mechanical grippers serve as standard transfer units in industrial settings for object manipulation. However, these grippers often employ substantial closure force to grasp and transfer objects, necessitating additional energy and posing a risk of damage to fragile items. Fortunately, bio-inspired adhesive surfaces offer a unique adhesion mechanism that eliminates the need for extra energy to maintain adhesion. Instead, they require only a small preload to generate significant adhesive grasping force, offering distinct advantages in the realm of soft grippers. Typically, based on the application scenarios, grippers utilizing bioinspired adhesives can be categorized into dry grippers and wet grippers.[11]

In dry environments, gecko-inspired adhesives serve as prevalent adhesion units for grippers. Typically, these grippers detach from the substrate through two mechanisms: buckling and shearing. In buckling-induced detachment, common structures include isotropic designs like mushroom-shaped pillars (Fig. 25A). These adhesives detach easily due to stress concentration from buckling or stretching during overloading or peeling.[11,71,488] Conversely, shearing-induced detachment employs anisotropic dry adhesive surfaces featuring inclined pillars and/or asymmetric tips. Grippers utilizing this design achieve highly anisotropic adhesion and friction, facilitating swift switching between attachment and detachment, such as those with micro wedge structures.[343] Furthermore, effective utilization of gecko-inspired adhesives in grippers necessitates maintaining principles of large, more effective contact area and uniform stress distribution.[67] For example, Jiang *et al.* implemented tendon and pulley differentials in their gripper system to ensure uniform tension across each adhesive unit (Fig. 25B).[252] This load-sharing mechanism extends small adhesive patches to larger effective contact areas. Additionally, Li *et al.* incorporated the adaptive-locking mechanisms in their gripper to accommodate surfaces with varying heights and curvatures, enabling conformal interfacial contact.[516] By locking the adaptation configuration, load distribution becomes uniform, allowing effective manipulation of both flat and curved objects.

In damp environments, adhesives inspired by tree frogs are preferred for their capillary action. Particularly in moist surgical settings, conventional surgical clamps often necessitate significant clamping forces to prevent slippery tissues from moving, posing a risk of soft tissue damage.[11] Recognizing the robust wet friction resulting from the capillary force, Zhang *et al.* introduced two-level hexagonal micropillar adhesive surfaces inspired by tree frogs onto surgical graspers.[28] This adaptation increased wet friction force by ninefold and reduced soft tissue deformation by 90% compared to graspers with sharp tooth interfaces. In addition, tree frog-inspired adhesives could also demonstrate their potential in handing objects in moist conditions. For example, Nguyen *et al.* engineered a soft robotic hand that employs adhesives mimic tree frogs to effectively grip items with irregular surfaces in wet conditions (Fig. 25C).[523] On the other hand, octopus-inspired adhesive surfaces demonstrate exceptional wet adhesion due to suction force, particularly remarkable underwater adhesion owing to water or oil's incompressibility. Drawing inspiration from the flexible movement

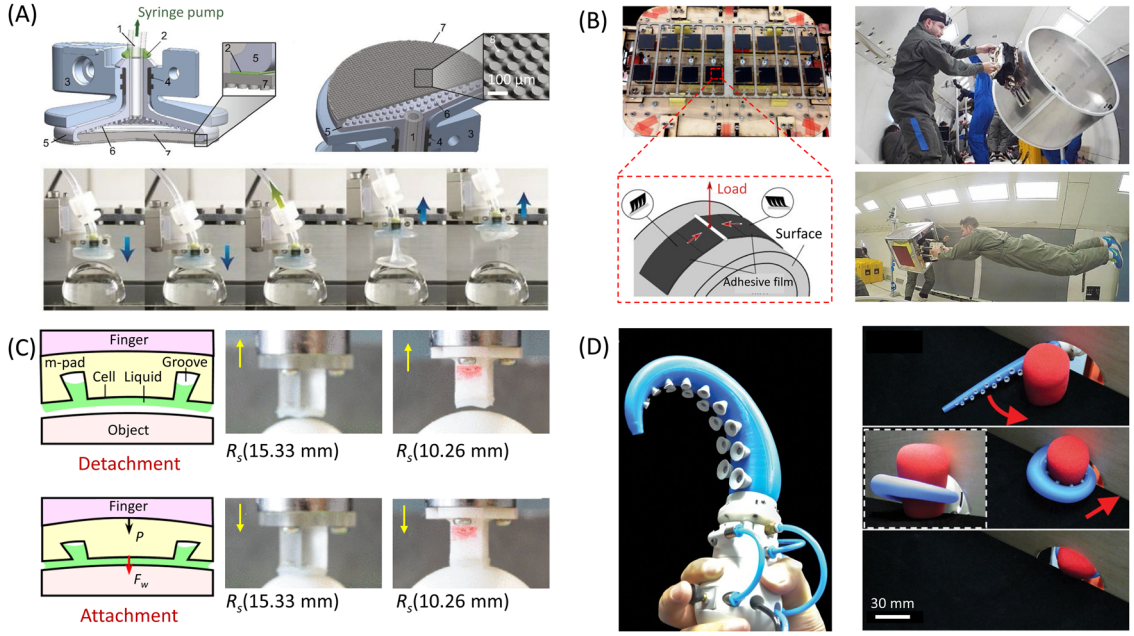

Fig. 25 Bioinspired adhesives used for soft grippers. (A) Gecko-inspired load-sharing soft grippers with isotropic mushroom-shaped pillars. The picture is reproduced with permission from ref. 71 Copyright 2017, National Academy of Sciences. (B) Gecko-inspired load-sharing soft grippers with inclined pillars (asymmetric tips). The picture is reproduced with permission from ref. 252 Copyright 2017, AAAS. (C) Tree frog-inspired soft grippers with capillary force. The picture is reproduced with permission from ref. 523 Copyright 2021, IEEE. (D) Octopus-inspired soft grippers with suction force. The picture is reproduced with permission from ref. 524 Copyright 2020, Mary Ann Liebert Inc.

and grasping actions of the soft suction cups on octopus arms, Mazzolai *et al.* developed a new type of soft gripper. This gripper demonstrates superior grasping performance in a variety of enclosed situations.[525] Similarly, capitalizing on variations in arm taper angle among octopus species, Xie *et al.* integrated octopus-inspired suckers into a tapered soft gripper, allowing it to effortlessly grasp diverse objects through a combination of bending and suction action (Fig. 25D).[524]

Regrettably, most grippers utilizing bioinspired adhesives are single-functional, lacking real-time monitoring of the grasping state. To address this limitation, Hu *et al.* created an innovative layered structure that integrates both adhesive and sensing capabilities.[526] This adhesive features a multilayer design; the top layer consists of mushroom-shaped micropillars for robust adhesion, the middle layer includes a cylindrical array, and the bottom layer contains pairs of metal electrodes designed specifically for capacitive sensing. Additionally, Wu *et al.* introduced a groundbreaking soft gripper mimicking bioluminescent octopus dorsal-ventral structure, showcasing exceptional grasping capabilities in underwater settings.[29] Furthermore, by leveraging variations in flow induced by diverse grasped objects at the suctorial mouth, the gripper can discern object dimensions and types. In summary, the future trend lies in integrating sensing functionality with bio-inspired adhesives and applying them to grippers.

9.4. Wearable electronics

Thanks to their robust adhesion properties, bioinspired adhesive surfaces have garnered significant attention for the development of biocompatible bioelectronics.[261] In comparison to conventional adhesives, biomimetic adhesives triggered by structural or chemical cues offer several key advantages, including robust wet and underwater adhesion, the elimination of the need for glue, enhanced adaptability and repeatability, and consistent self-cleaning capabilities. By integrating these structural adhesives with embedded electronic chips or sensors, wearable bioelectronic devices have seen extensive development for monitoring physical parameters such as stress and temperature, as well as electrophysiological signals like electrocardiograms and electroencephalograms.[488,527–529] Additionally, these devices are capable of collecting different biofluids to gather biochemical data including glucose and pH levels, as well as enzyme activity.[530] Equipped with reliable real-time monitoring features, these smart skin patches offer a straightforward, economical, and dependable method to deliver health feedback, facilitating prompt preliminary diagnosis and treatment.

However, the complexity of skin and tissue surfaces presents challenges, including the skin's multi-layered structure and the irregular wetting conditions of body tissue surfaces, most adhesives may exhibit less than satisfactory interfacial adhesion properties on the skin.[531] To address this challenge, modifications have been made to mushroom-shaped setae arrays to better conform to the skin's layered morphology (Fig. 26). For example, Drotlef *et al.* developed an adhesive tape that emulates the mushroom-shaped structure of gecko bristles and reproduced the layered structure of the skin on this adhesive *via* the inking method.[488] These adapted structures enable the adhesive to establish conformal contact with the skin, thereby enhancing interfacial adhesion. In addition, the presence of moisture on perspired skin and body tissues can reduce the interfacial

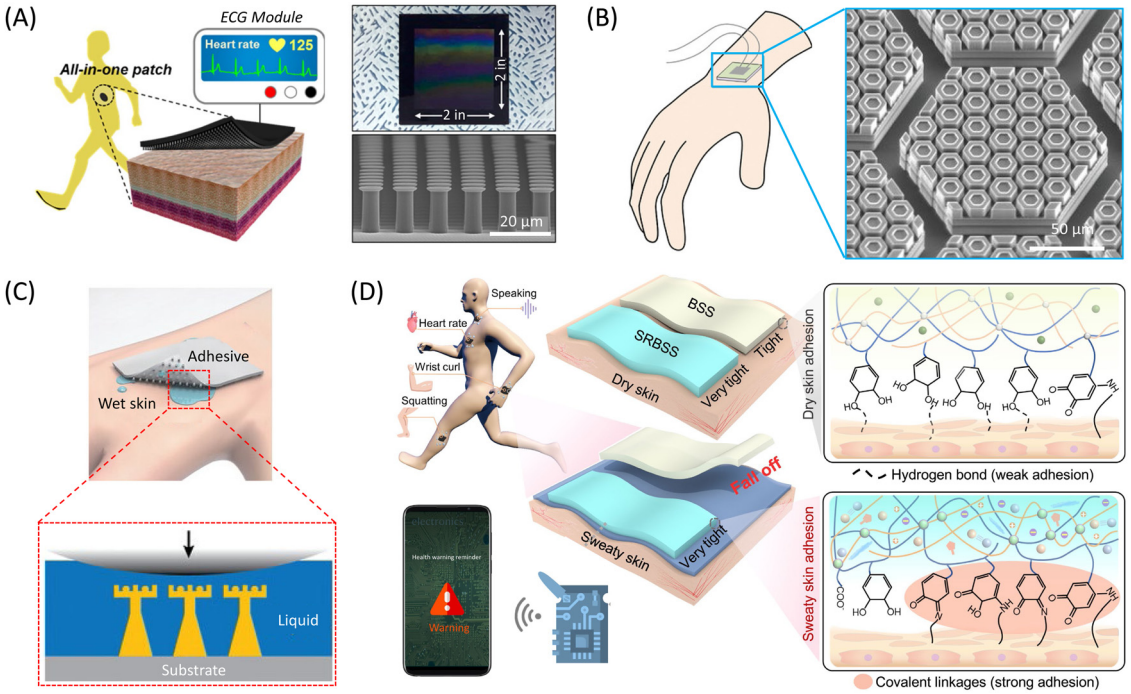

Fig. 26 Bioinspired adhesives used for wearable electronics. (A) Gecko-inspired conductive adhesive for ECG electrodes. The picture is reproduced with permission from ref. 65 Copyright 2016, American Chemical Society. (B) Tree frogs-inspired conductive adhesive for wearable flexible electronics. The picture is reproduced with permission from ref. 28 Copyright 2020, Wiley-VCH. (C) Octopus- and gecko-inspired micro-structured adhesives for wearable electronics. The picture is reproduced with permission from ref. 330 Copyright 2021, Wiley-VCH. (D) Mussel-inspired hydrogel adhesives for wearable electronics. The picture is reproduced with permission from ref. 181 Copyright 2023, Elsevier BV.

adhesion of adhesives with gecko-inspired setae arrays. In response, Zhang *et al.* proposed a two-level hexagonal micropillar adhesive surface, inspired by the hierarchical hexagonal structure of tree frog toes, capable of adhering to humid skin surfaces (Fig. 26B).[28] Furthermore, octopus-inspired functional surfaces have demonstrated significant interfacial adhesion on perspired skin and even on tissues inside the body surrounded by interstitial fluid, owing to negative pressure effects. Dayan *et al.* prepared a hybrid adhesive that combines sucker structures inspired by octopuses and gecko feet, showcasing strong reversible adhesion on both wet and dry surfaces (Fig. 26C).[330] This innovation provides valuable insights for the application of wearable devices in various contexts. Apart from structural-based adhesive electronics, chemical-based adhesive electronics also exhibit commendable performance on sweaty skin and tissues. For instance, Li *et al.* introduced a sweat-resistant bioelectronic skin sensor (SRBSS) inspired by the adhesion mechanism of mussel (Fig. 26D).[181] The SRBSS demonstrates robust adhesion to human skin with different surface features, as well as reliable and sensitive performance in electrical signal detection. Additionally, this hydrogel's low swelling and antibacterial behavior make it suitable for use as an interface in electronic skin devices for prolonged, real-time monitoring of bioelectric signals, even in the presence of sweat. This innovation offers a fresh perspective on the design of wearable electronic sensors for human–computer interactions.

Integrating electrodes with adhesives presents another challenge that requires addressing. Traditional adhesive tapes incorporating metal electrodes often suffer from stress concentration, leading to peeling around the electrode and compromising the entire interface.[11] For example, Bae *et al.* found that their adhesive tape could only provide effective adhesion for electrodes under mild conditions, such as during rest, to prevent crack propagation.[532] To counteract the self-peeling issue stemming from the additional metal electrode, Drotlef *et al.* integrated a skin-adhesive film with strain sensors for monitoring vital signals like heart rate.[488] Moreover, Kim *et al.* introduced two types of carbon nanomaterials into PDMS to create a conductive adhesive with enhanced electric percolation (Fig. 26A).[65] This innovative elastomer combines skin adhesion and biological signal acquisition, enabling direct collection of human body signals without the need for extra metal electrodes. Importantly, the conductive adhesive surface can effectively capture biological signals even during physical activities and underwater, surpassing the capabilities of typical acrylic-based medical patches with metal electrodes. Compared to structural adhesive sensors, chemically bonded conductive gels are a better option to solve the problems aroused by the metal electrodes. This is due to the fact that they are inherently conductive without the need for additional electrodes and can exhibit mechanical properties similar to those of rubber elastomers. The remarkable electrochemical stability, moldability, and biocompatibility of conductive hydrogel adhesives have unlocked new avenues for applications across various fields, including soft robotics, wearable devices, artificial skin, flexible touch screens, and brain–machine interfaces.[527,533–543] Particularly, wearable electronics incorporating stretchable ionized

hydrogel adhesives have garnered significant interest for their capabilities in temperature, pressure, and strain sensing, as well as neurophysiological communication properties.[62,544–546] These wearable electronics not only offer excellent flexibility and high sensitivity to bioelectric signals but can also translate physiological activity signals into detectable electronic signals, thus expanding the possibilities for early diagnosis and therapy of serious diseases.[380,547–550] For example, Cai *et al.* presented a skin sensor system based on self-adhesive hydrogels, which hinges on the heterogeneous integration of the silica nanoparticles with vinyl groups (VSNP) and polyacrylamide (PAM) to form a viscous hydrogel (VSNP-PAM) to serve as the resilient elastic matrix, coupled with orthogonal bending sensing structure contributed by 1D and 2D nano conductive materials.[548] This hydrogel exhibits exceptional compliance and viscoelasticity to adapt to human skin, making it well-suited for skin sensor applications. Notably, the VSNP-PAM hydrogel achieves high toughness ($\sim$7020 J m^{-2}) and very low hysteresis ($<$ 0.1) through synergistic interactions between spatially abundant hydrogen bonding in PAM chains and covalent bonding between PAM and VSNPs, ensuring rapid responsiveness ($\sim$90 ms) and remarkable resilience ($\sim$240 ms) of the skin sensor. Moreover, the high stretchability of the VSNP-PAM hydrogel allows for harnessing the mechanical instabilities of 2D MXene nanosheets and 1D PpyNWs adhered to the pre-stretched hydrogel, resulting in tailored self-organized hierarchical structures. Controlled relaxation of prestrains in a specific order facilitates the transformation of these hierarchically crumpled structures upon stretching, enabling MXene-PpyNW sensing components with functionality across a wide working range. Additionally, by laminating two heterostructure networks together, the sensing mechanism can transition from piezoresistive to a capacitive effect, empowering tactile sensing in x, y, and z directions, and detection of proximity from a distance of up to 20 cm.

9.5. Biomedical engineering

Compared to synthetic adhesives, bioinspired adhesives utilizing biopolymers offer distinct advantages in biomedical applications due to their excellent biocompatibility, biodegradability, non-toxicity, cost-effectiveness, and renewable nature.[551–554] Bioinspired structure and or chemistry adhesion has emerged as a promising approach to enhancing bioinspired adhesives for biomedical purposes.[5,41,44] Particularly, the mussel-inspired chemistry strategy not only enhances the self-adhesive properties of bioinspired adhesives but also improves their chelating and coordinating capabilities, biological compatibility, and bioactivity. Additionally, it enables secondary reactions with various molecules, facilitating the creation of hybrid materials with tailored properties. In this section, we will underscore the significance of bioinspired adhesives in biomedical applications such as tissue adhesion, hemostasis, wound healing, drug delivery, *etc.*

Millions of individuals experience a wide range of tissue wounds every year, from minor skin cuts to severe injuries, caused by various factors such as accidents, chronic conditions like diabetic ulcers, and surgical procedures.[555] The standard clinical approach to treating these injuries involves reconnecting the damaged tissues and closing the wound area to halt bleeding, prevent fluid leakage, and ultimately restore tissue integrity and function.[39,556] Historically, sutures and staples have been the primary methods used to achieve these objectives. They effectively bring tissues together during the healing process, providing stability and resistance to mechanical stress, thereby reducing the risk of wound reopening.[557] Despite their widespread use and effectiveness in many scenarios, they have limitations. For instance, they may not be suitable for situations requiring the containment of body fluids or air leakage prevention. Additionally, when dealing with large wounds, achieving complete closure can be challenging. Suturing is a time-intensive process that increases the duration of surgery and the likelihood of complications such as infections.[558] In emergencies, where time is of the essence, suturing may not be feasible due to its prolonged application time.[559] Although staples could offer rapid closure, their subsequent removal and the mechanical stress they exert on tissues limit their utility. Furthermore, both sutures and staples could cause tissue damage and scarring if tissue alignment is not precise during application.[560] Moreover, they are not suitable for minimally invasive or microsurgical procedures with limited access to the surgical site. Bioinspired adhesives present an appealing alternative for surgical interventions, as they can provide mechanical support, promote hemostasis, seal wounds, and prevent leakage (Fig. 27A).[561,562]

Hyaluronic acid hydrogels grafted with catechol or gallol are highly appealing as tissue adhesives. These hydrogels, modified with dopamine, are synthesized by attaching catechol groups to the hydrogel polymer chains with the help of $NaIO_4$ (for oxidation), resulting in robust tissue adhesion.[565] The catechol groups within the mussel-inspired hydrogel exhibit a strong binding affinity towards various nucleophilic groups, including amido, thiol, imidazole, *etc.*, which accounts for its adhesive properties. Consequently, the hydrogel can effectively adhere to peptides or proteins on the tissue surface. For example, Liang *et al.* devised a multifunctional nanocomposite hydrogel by combining dopamine-grafted hyaluronic acid with PDA-coated rGO, aiming for efficient wound dressing applications.[566] This injectable nanocomposite hydrogel exhibited favorable attributes such as swelling capacity, biodegradability, adjustable rheological properties, and satisfactory mechanical strength. The incorporation of catechol groups and PDA from hyaluronic acid grafted with dopamine endowed the hydrogel with enhanced tissue adhesion, reliable antioxidant properties, hemostatic benefits, and antibacterial behavior driven by NIR light. Furthermore, these hydrogels demonstrated sustained drug release for over 10 days and displayed remarkable facilitation of full-thickness skin wound repair in a mouse model. Consequently, these multifunctional composite hydrogels hold promise as viable candidates for advanced wound healing dressings. In the realm of innovative wound dressings mentioned above, current research primarily emphasizes their biochemical functionalities. However, wound dressings capable of promoting early wound healing by inducing wound closure through biomechanical forces have been overlooked. To address this problem, Li *et al.* innovated the

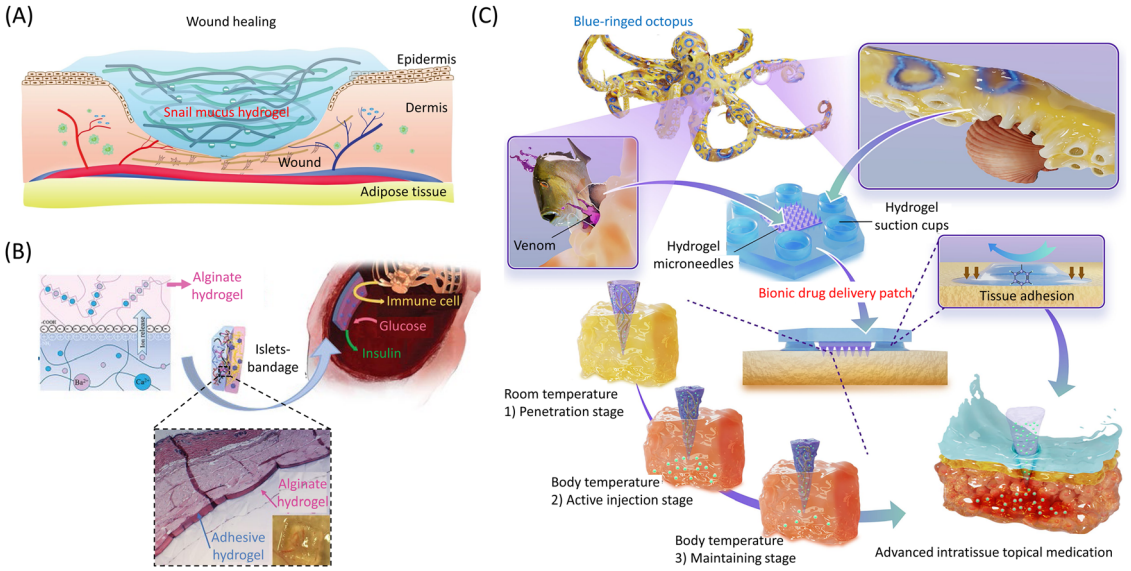

Fig. 27 Bioinspired adhesives used for biomedical engineering applications. (A) Biomimetic hydrogel adhesive used for wound healing and hemostasis. The picture is reproduced with permission from ref. 563 Copyright 2023, Springer Nature. (B) Mussel-inspired hydrogel bandage containing both adhesive layer and islet-encapsulating layer used for drug delivery. The picture is reproduced with permission from ref. 366 Copyright 2020, Wiley-VCH. (C) Octopus-inspired hydrogel microneedle patch with tissue adhesion and drug injection functions. The picture is reproduced with permission from ref. 564 Copyright 2023, AAAS.

creation of multifunctional antibacterial adhesives and antioxidant hemostatic hydrogel dressings using a blend of polyethylene glycol monomethyl ether modified glycidyl methacrylate functionalized chitosan (CSG-PEG), methacrylamide dopamine (DMA), and zinc ions.[567] These hydrogels exhibited notable hemostatic capabilities in both mouse liver hemorrhage and mouse-tail amputation models, alongside inherent antibacterial properties against Methicillin-resistant *Staphylococcus aureus* (MRSA). Additionally, the hydrogel's effective volume contraction and tissue adhesion facilitated early wound closure and promoted wound healing. These findings suggest their promising potential as an alternative for treating infected wounds.

In addition to wound healing and hemostasis, the ability to release drugs is another major feature of the new bionic adhesive. Ryu *et al.* fabricated a fully cross-linked intraperitoneal (IP) patch and a partially cross-linked (c-IP) patch through the freeze-drying of catechol-grafted chitosan.[568] The IP patch exhibited robust adhesion (~42 kPa) to wet tissue in the peritoneum of mice, whereas the c-IP patch showed a marginally lower strength of around 34 kPa. To investigate their efficacy in cancer therapy, both patches were infused with the anticancer drug 5-fluorouracil. Subsequently, cancer progression was simulated by introducing human colon cancer cells into the mice's peritoneum. One week later, the drug-loaded patches were applied to the peritoneal surfaces of the test mice. The results indicated that the medicated c-IP patch, thanks to its partially cross-linking network which aids in the prolonged release of the drug, exhibited a more pronounced anticancer effect than the medicated IP patch. Consequently, these partially cross-linked multifunctional patches show promise as adhesive drug carriers for cancer therapy. Similarly, Chen *et al.* introduced an adhesive hydrogel tape featuring high hydrogen bond density (Fig. 27B), leveraging the load-sharing effect of "triple hydrogen bonding clusters" (THBCs).[366] When integrated as side groups within the hydrogel matrix, THBCs impart robust adhesion of the hydrogel to various surfaces, including glass and tissues. This hydrogel serves as the foundation for the development of two groundbreaking therapeutic bandage aimed at treating diabetes (type 1) and liver cancer. To treat liver cancer, researchers incorporated human serum albumin combined with cisplatin medicine into hydrogel bandages. These bandages are biodegradable and could be directly adhered to the liver, enabling for precise drug delivery to the tumor site, and its therapeutic efficacy surpasses that of conventional injections. Moreover, the hydrogel's biodegradable nature ensures that it will break down in the body after releasing the drug. Conversely, the hydrogel bandages designed for diabetes treatment are used externally and are not biodegradable. They consist of two layers: an encapsulation layer for storing and releasing insulin, and an adhesive hydrogel layer that ensures long-lasting and stable attachment. Research has demonstrated that this bandage could maintain stable adhesion to the peritoneal wall of test mice for over a month, effectively managing blood sugar levels throughout that time. These cutting-edge hydrogel bandages offer a multifunctional platform for sustained drug delivery and targeted therapy, revolutionizing treatment approaches for these conditions.

Apart from biomimetic hydrogel adhesives for drug release inspired by mussel chemistry, researchers have also developed biomimetic adhesives for drug release inspired by biological surface structures. For example, Chen *et al.* prepared a glucose-responsive insulin delivery microneedle (MN) array patch designed to address hyperglycemia, employing red blood cell (RBC) vesicles or liposome nanoparticles containing glucose transporters (GLUTs) bound with glucosamine-modified insulin

(Glu-Insulin).[569] The MN array could penetrate the skin, as blood sugar levels increase, the higher glucose concentration in the interstitial fluid enhances its likelihood of binding to GLUT. This binding competes with glutamate insulin's attempt to attach to the same sites on GLUT. When glutamate insulin fails to bind, it is released into the system. This released insulin plays a crucial role in regulating glucose levels in blood. To ensure a sustained release of glucose-responsive insulin, researchers supplemented the system with additional free glutamate insulin, acting as ''reserve insulin''. This innovative GLUT-based smart insulin patch successfully maintained blood glucose control over the long term in mice with streptozotocin (STZ)-induced diabetes (type 1). Similarly, drew inspiration from the hunting tactics of the blue-ringed octopus, Zhu *et al.* crafted a wet-adhesive capable of controlled drug delivery through the microneedle patch structure (Fig. 27C).[564] This innovation aims to achieve adhesion to tissue surfaces and effective topical medication. Specifically, hydrogel suction cups based on pluronic F127 (F127) are crafted onto Silk-Fp to enable wet-bonding functionality. The interior surface of the suction cup is treated with tannic acid (TA) to establish biocompatible chemical bonding. Additionally, the flexible cup structure not only facilitates physical adhesion (>10 kPa) due to air pressure differentials but also shields the chemical bonding interface from liquid environments, ensuring the stability of the silk fibroin-pluronic F127 (Silk-Fp) patch against wet tissues for prolonged periods. Moreover, the Silk-Fp patch incorporates controllable drug-releasing hydrogel microneedles (MNs) containing silk fibroin (SF) and PNIPAm, designed to achieve efficient drug delivery within tissues. These Silk-Fp MNs can be loaded with anti-inflammatory medication (such as dexamethasone sodium phosphate, also known as DEX) for treating oral ulcers or with anticancer drugs (such as 5-fluorouracil, also known as 5-FU) for addressing epidermal tumors in early stage. Rely on the robust structure and high aspect ratio, Silk-Fp MNs can effectively breach mucosal layers beneath the epidermis or navigate through soft barriers like ulcers and tumors, thus enabling precise drug delivery strategies. The Silk-Fp MNs offer two distinct modes of drug delivery: the first provides rapid action, where drug release is triggered immediately by contractions from concentration gradients upon entry into target tissues; the second ensures sustained treatment, where drug dispensation is temperature-regulated. For instance, if the Silk-Fp MNs' temperature exceeds the phase transition threshold of PNIPAm, it switches from a hydrophilic to a hydrophobic state, facilitating drug dispersion. Consequently, Silk-Fp MNs ensure adequate drug concentration (<2 hours) during the initial treatment phase, followed by gradual drug release over the subsequent two days to sustain therapeutic efficacy in a hydrogel state. Thus, the biomimetic Silk-Fp patch, with stable wet adhesion and controllable intratissue drug delivery capabilities, exhibits the potential to accelerate the healing of oral ulcers through DEX release or effectively inhibit tumor growth when loaded with 5-FU.

In conclusion, the utilization of bioinspired adhesives holds promising prospects, capitalizing on the favorable amalgamation of natural adhesive structures and chemistry. This section aims to provide a thorough overview of the recent advancements in bioinspired adhesives across various domains including droplet manipulation, climbing robots, soft grippers, wearable electronics, and biomedical engineering. Table 9 summarizes the advantages and challenges of bioinspired adhesives in the aforementioned applications. It is anticipated that this comprehensive framework will stimulate increased interest among researchers to delve into this burgeoning field, thereby guiding the future development of innovative bioinspired adhesive systems.

10. Conclusions and perspectives

To thrive in diverse habitats, organisms have evolved unique micro-nano structures and/or chemical compositions, endowing them with exceptional adhesive properties crucial for tasks like securing themselves and capturing prey. This work delves into various adhesion models rooted in different natural systems, starting with the interaction forces at interfaces. Then, recent advancements in bio-adhesive surfaces and their synthetic counterparts are discussed, focusing on the structural and chemical aspects of contact interfaces. Combined with the detailed explanation of preparation and measurement methods for biomimetic adhesive surfaces. Particular attention is paid to switchable adhesives with smart response capabilities, ending with the latest developments in emerging applications. Although significant progress has been made in this field, there is room for the development of new technologies (Fig. 28).

First, there is a notable gap in comprehending the adhesion mechanisms stemming from both multiscale micro- and nanostructures and catechol chemistry, impeding the development and application of corresponding biomimetic adhesive surfaces. On a structural level, existing research has failed to deeply analyze the underlying working mechanisms of tree frogs' polygonal micropillars and the role of the dual-chamber structure of the octopus' sucker, hindering advancements in tree frog/octopus-inspired adhesive systems.[6] Regarding chemical aspects, uncertainties persist in understanding mussel chemistry's adhesion mechanisms. Although some studies employ measurement techniques like atomic force microscopy (AFM)/surface force instrument (SFA) along with related theoretical simulations to analyze the mussel's adhesion, they predominantly focus on specific systems (*e.g.*, mussel adhesion proteins and dopa chemistry), making it challenging to delineate each interaction's distinct contributions to adhesion and cohesion.[5] Moreover, the impact of polymer chemical composition and molecular configuration on shellfish adhesion requires careful consideration, stemming from the notable achievements in polymer-shellfish chemical combinations. To further elucidate the potential adhesion mechanisms of biological adhesive surfaces, it is imperative to leverage advanced characterization methods to deepen the understanding of biological adhesion systems.[579,580] Meanwhile, considerable efforts are still required to develop higher-precision characterization instruments or methods to enhance the research depth and width of biological adhesion mechanisms. Additionally, continuous exploration and

Table 9 Summary of advantages & challenges of bioinspired adhesives in different applications

Application fields	Specific devices/categories	Features/advantages	Limitations/challenges	Ref.
Droplet manipulation (responsive SLIPs)	Controllable chemical microreactions	Rapid, precise and remote manipulation High droplet transfer efficiency No geometry limitation of droplets'	Larger-scale liquid transport Droplet's contamination lubricant layer	408, 447, 493 and 570
	Pipetting devices	Simplify liquid handling in the microplate and microarrays Avoid cross-contamination No repellent liquids residual	Elastic slippery film structures are too soft, and need to be fixed on tough substrates Difficult to stretch	446 and 448
	Fog collection systems	Programmable control High collection efficiency Continuously collection	Larger-scale fog harvesting Water captured is easy to be affected by external factors	444 and 490
Climbing Robots	Tracked climbing robots with hydrogel adhesives	Large-span tailored adhesion Quick regulation between adhesive and non-adhesive state	Limited by the gradient and material of the wall surface	512
	Wheeled/tracked climbing robot with mushroom-shaped arrays	Climb on vertical surfaces	Movement model limitation	513, 514, 571 and 572
	Traditional legged robots	More flexible Better adaptability Safer	Can not climb on the inverted ceiling Limited adhesion capacity	355, 515, 518–520 and 573
	Legged robots with a supporting layer of adhesive foot modules	Stable climbing capacity on a vertical surface or an inverted ceiling Reduce the shock caused by the actuators Uniform load-sharing	Cannot adapt to narrow conditions	516 and 521
	Soft climbing robots	Small size and flexibility Better responsiveness High load	Limited adhesion Limited climbing angle of slopes	517 and 522
Soft Grippers	Gecko-inspired grippers with isotropic structure	Isotropic adhesion and friction	Easy to fall off when stress is concentrated Limited in dry environments	71, 488 and 574
	Gecko-inspired grippers with anisotropic structure	Anisotropic adhesion and friction Rapid switch between attachment and detachment	Limited in dry environments	343 and 575
	Tree frog-inspired grippers	Wet friction and adhesion aroused by the capillary force Applied in both dry & wet environments	Limited adhesion	28 and 523
	Octopus-inspired grippers	Excellent wet adhesion based on the suction force Applied in both dry & wet environments	Limited adhesion in dry environments	524, 525 and 576
Wearable Electronics	Gecko-inspired adhesive sensors	Conformal contact with the skin Reversible adhesion	Limited to dry skin	488
	Tree frog-inspired adhesive sensors	Conformal contact with the skin Reversible adhesion Applied to dry, wet, and oily skins	Limited adhesion strength	28
	Octopus-inspired adhesive sensors	Strong interfacial adhesion Applied to dry, wet, and oily skins	Complex structures	8 and 49
	Mussel-inspired adhesive sensors	Tough interfacial adhesion Applied to dry, wet, and oily skins	Complicated fabrication process Sometimes difficult to detach	181, 548, 577 and 578
Biomedical Engineering	Mussel-inspire tissue adhesives for sealing wounds	Excellent biocompatibility, biodegradability, non-toxicity, cost-effectiveness, and renewable Rapid cut closure Multifunctional	Based on direct chemical reactions for adhesion Catechol groups are easy to be oxidized Energy dissipation in the hydrogel bulk	561, 562 and 565–567
	Mussel-inspire tissue adhesives for drug delivery	Long working time Could be injectable Multifunctional	Catechol groups are easy to be oxidized	366 and 568
	Structural-inspire tissue adhesives for drug delivery	Rapid response Long working time Stable adhesion	Limited adhesion strength	564 and 569

discovery of new adhesion phenomena in nature are essential to complement and refine existing biological adhesion systems, thereby driving advancements in bioinspired adhesion systems.

Second, existing artificial biomimetic adhesives often encounter challenges in achieving adhesion properties comparable to biological prototypes or need to compromise in other properties to maintain adhesion capabilities. For instance, the hierarchical structure observed in natural biological surfaces demonstrates adaptability to contaminants and surfaces with varying roughness, a trait not yet replicated in artificial biomimetic materials

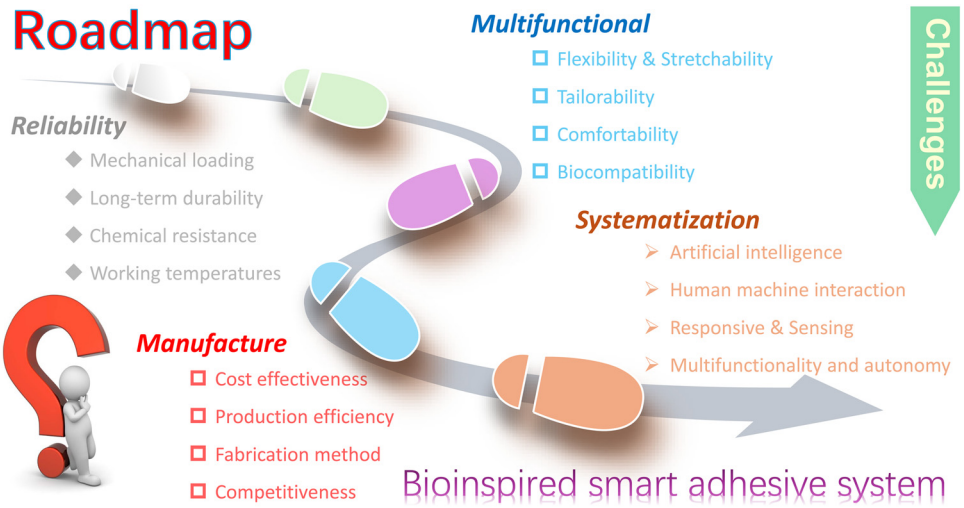

Fig. 28 Roadmap for the development of bioinspired adhesive system.

due to limitations in current manufacturing precision.[581] Thus, there is an urgent need for reliable and cost-effective fabrication techniques capable of mimicking multiscale structures. It is worth highlighting the rapid advancements in advanced additive manufacturing technologies, such as 3D or even 4D printing, which are poised to significantly enhance the practical application of large-scale, high-quality micro-nanostructured surfaces with optimal interfacial bonding strength. On the other hand, the unresolved problem of the polymerization mechanism and molecular structure of mussel polydopamine (PDA) poses challenges in designing adhesives based on its adhesion mechanism. Notably, the catechol group of PDA quenches free radicals during the synthesis process of hydrogel adhesives, leading to inhibited polymer chain length and cross-linking density, resulting in hydrogel adhesives with subpar mechanical properties and limited practical applications.[5] To address this, potential solutions include introducing protected groups of catechol or adopting novel synthetic strategies, such as dopamine-triggered monomer polymerization, as alternatives to traditional construction methods. Additionally, the dark color of PDA-based adhesives may pose challenges, particularly in applications involving transparent electronics or devices. The emergence of natural polyphenols as promising alternatives indicates a bright future for mussel-inspired transparent adhesives. For SLIPs in solid–liquid adhesion systems, maintaining a thin layer of lubricant atop the solid substrate is essential for ensuring the durability and long-term functionality of responsive SLIPs. Without this lubricant layer, the repellent droplets resting on the SLIPs would remain in a non-slippery state, rendering them unable to transition to a slippery state.[426] However, when repellent droplets are cloaked by the lubricant, excess lubricant may be drawn from the substrate as the droplets slide away. The high depletion rate of lubricant can lead to a range of adverse outcomes. Foremost, it drastically shortens the service life of the responsive SLIPs. Additionally, the loss lubricant can result in further pollution issues, thereby restricting the applicable scenarios for these products.[511,582,583] Potential methods for mitigating lubricant loss include selecting lubricants with higher viscosity and lower vapor pressure, enhancing the chemical affinity between the lubricant and substrate, and implementing self-regulated lubricant secretion mechanisms.[426,584,585]

Last but not least, bioinspired adhesives face with issues such as short lifespan caused by wear and tear, and limited applicability. Natural adhesive surfaces possess self-repair or self-replacement abilities, as seen in creatures like geckos and octopuses which can regenerate their fiber structures or suction cups if these structures are destroyed. By integrating such self-repair capabilities into biomimetic adhesives, their resilience in diverse environments could be notably enhanced.[586,587] Fortunately, recent advancements in self-healing materials offer promising prospects for the development of biomimetic adhesives with inherent repair capabilities.[588–590] From a practical standpoint, a promising avenue involves imbuing biomimetic adhesives with multifunctionality and autonomy. This entails integrating soft biomimetic smart adhesives with flexible sensors and artificial intelligence, empowering the adhesives to autonomously adapt their behavior based on real-time feedback. Such intelligent bioinspired adhesives hold immense potential to expand their utility across a spectrum of environments, from extreme temperatures in space to the high pressures of the deep sea.[252] As biomimetic artificial adhesives continue to advance, they are poised to emerge as a versatile strategy enabling intelligent interactions among digital devices, the human body, and physical systems.

In summary, bioinspired adhesives are assuming an increasingly pivotal role across various domains including liquid manipulation, soft grippers, wearable devices, healthcare, climbing robots, *etc.* These diverse applications often share common requirements such as reliable adhesion, durability, and minimal environmental impact, sometimes necessitating biodegradability. Addressing these demands requires collaborative efforts across multiple disciplines including biology, chemistry, physics, electronics, materials science, *etc.* By leveraging interdisciplinary cooperation, we can enhance the performance and reduce the

production costs of bio-inspired adhesives for diverse applications. We are confident that this collaborative approach holds great potential, and the advancements in bioinspired adhesives will catalyze the development of innovative, intelligent adhesion devices.

Author contributions

M. L. conceived, designed, and executed this project. M. L. and A. M. wrote the main content of the paper, they contribute equally to this work. Q. G. assisted in the writing and revision of the manuscript. E.S. revised the content of perspective and provided useful suggestions. All authors discussed the results and commented on the manuscript.

Data availability

No primary research results, software or code have been included and no new data were generated or analysed as part of this review.

Conflicts of interest

The authors declare no competing interests.

Acknowledgements

This work was supported by the EPSRC Program Manufacture Using Advanced Powder Processes (MAPP)EP/P006566. Ming Li acknowledges financial assistance from Imperial College London and grants him the ''President Scholarship'' (01790264). Q. G. appreciates the support from the China Scholarship Council (grant 202006440011).

References

1 D. Nepal, S. Kang, K. M. Adstedt, K. Kanhaiya, M. R. Bockstaller, L. C. Brinson, M. J. Buehler, P. V. Coveney, K. Dayal and J. A. El-Awady, *Nat. Mater.*, 2023, **22**, 18–35.
2 H. Jin, L. Tian, W. Bing, J. Zhao and L. Ren, *Prog. Mater. Sci.*, 2022, **124**, 100889.
3 Z. H. Guo, H. L. Wang, J. Shao, Y. Shao, L. Jia, L. Li, X. Pu and Z. L. Wang, *Sci. Adv.*, 2022, **8**, eabo5201.
4 M. Li, C. Li, B. R. Blackman and E. Saiz, *Matter*, 2021, **4**, 3400–3414.
5 C. Zhang, B. Wu, Y. Zhou, F. Zhou, W. Liu and Z. Wang, *Chem. Soc. Rev.*, 2020, **49**, 3605–3637.
6 Y. Chen, J. Meng, Z. Gu, X. Wan, L. Jiang and S. Wang, *Adv. Funct. Mater.*, 2020, **30**, 1905287.
7 Y. Zhao, Y. Wu, L. Wang, M. Zhang, X. Chen, M. Liu, J. Fan, J. Liu, F. Zhou and Z. Wang, *Nat. Commun.*, 2017, **8**, 2218.
8 S. Baik, D. W. Kim, Y. Park, T.-J. Lee, S. Ho Bhang and C. Pang, *Nature*, 2017, **546**, 396–400.
9 A. Than, C. Liu, H. Chang, P. K. Duong, C. M. G. Cheung, C. Xu, X. Wang and P. Chen, *Nat. Commun.*, 2018, **9**, 4433.
10 Y. Wang, X. Yang, Y. Chen, D. K. Wainwright, C. P. Kenaley, Z. Gong, Z. Liu, H. Liu, J. Guan and T. Wang, *Sci. Rob.*, 2017, **2**, eaan8072.
11 W. Duan, Z. Yu, W. Cui, Z. Zhang, W. Zhang and Y. Tian, *Adv. Colloid Interface Sci.*, 2023, **313**, 102862.
12 J. Li, X. Han, W. Li, L. Yang, X. Li and L. Wang, *Prog. Mater. Sci.*, 2023, **133**, 101064.
13 J. Li, A. Celiz, J. Yang, Q. Yang, I. Wamala, W. Whyte, B. Seo, N. Vasilyev, J. Vlassak and Z. Suo, *Science*, 2017, **357**, 378–381.
14 K. Autumn, Y. A. Liang, S. T. Hsieh, W. Zesch, W. P. Chan, T. W. Kenny, R. Fearing and R. J. Full, *Nature*, 2000, **405**, 681–685.
15 E. Arzt, S. Gorb and R. Spolenak, *Proc. Natl. Acad. Sci. U. S. A.*, 2003, **100**, 10603–10606.
16 K. Autumn, M. Sitti, Y. A. Liang, A. M. Peattie, W. R. Hansen, S. Sponberg, T. W. Kenny, R. Fearing, J. N. Israelachvili and R. J. Full, *Proc. Natl. Acad. Sci. U. S. A.*, 2002, **99**, 12252–12256.
17 J. Iturri, L. Xue, M. Kappl, L. García-Fernández, W. J. P. Barnes, H. J. Butt and A. del Campo, *Adv. Funct. Mater.*, 2015, **25**, 1499–1505.
18 I. Scholz, W. J. P. Barnes, J. M. Smith and W. Baumgartner, *J. Exp. Biol.*, 2009, **212**, 155–162.
19 F. Tramacere, N. M. Pugno, M. J. Kuba and B. Mazzolai, *Interface Focus*, 2015, **5**, 20140050.
20 F. Tramacere, E. Appel, B. Mazzolai and S. N. Gorb, *Beilstein J. Nanotechnol.*, 2014, **5**, 561–565.
21 F. Tramacere, L. Beccai, M. Kuba, A. Gozzi, A. Bifone and B. Mazzolai, *PLoS One*, 2013, **8**, e65074.
22 P. Ditsche, J. Michels, A. Kovalev, J. Koop and S. Gorb, *J. R. Soc., Interface*, 2014, **11**, 20130989.
23 V. L. Popov, Q. Li, I. A. Lyashenko and R. Pohrt, *Friction*, 2021, **9**, 1688–1706.
24 J. C. Mergel, J. Scheibert and R. A. Sauer, *J. Mech. Phys. Solids*, 2021, **146**, 104194.
25 Z. Han, Z. Mu, W. Yin, W. Li, S. Niu, J. Zhang and L. Ren, *Adv. Colloid Interface Sci.*, 2016, **234**, 27–50.
26 Y. Song, Z. Wang, Y. Li and Z. Dai, *Friction*, 2022, **10**, 44–53.
27 J. Xie, M. Li, Q. Dai, W. Huang and X. Wang, *Int. J. Adhes. Adhes.*, 2018, **82**, 72–78.
28 L. Zhang, H. Chen, Y. Guo, Y. Wang, Y. Jiang, D. Zhang, L. Ma, J. Luo and L. Jiang, *Adv. Sci.*, 2020, **7**, 2001125.
29 M. Wu, X. Zheng, R. Liu, N. Hou, W. H. Afridi, R. H. Afridi, X. Guo, J. Wu, C. Wang and G. Xie, *Adv. Sci.*, 2022, **9**, 2104382.
30 J. H. Waite and M. L. Tanzer, *Science*, 1981, **212**, 1038–1040.
31 H. Lee, S. M. Dellatore, W. M. Miller and P. B. Messersmith, *Science*, 2007, **318**, 426–430.
32 Q. Guo, J. Chen, J. Wang, H. Zeng and J. Yu, *Nanoscale*, 2020, **12**, 1307–1324.
33 B. K. Ahn, *J. Am. Chem. Soc.*, 2017, **139**, 10166–10171.
34 J. Chen and H. Zeng, *Langmuir*, 2022, **38**, 12999–13008.
35 Y. Kan, E. W. Danner, J. N. Israelachvili, Y. Chen and J. H. Waite, *PLoS One*, 2014, **9**, e108869.
36 B. K. Ahn, S. Das, R. Linstadt, Y. Kaufman, N. R. Martinez-Rodriguez, R. Mirshafian, E. Kesselman, Y. Talmon,

B. H. Lipshutz and J. N. Israelachvili, *Nat. Commun.*, 2015, **6**, 8663.
37 X. Zhao, X. Chen, H. Yuk, S. Lin, X. Liu and G. Parada, *Chem. Rev.*, 2021, **121**, 4309–4372.
38 J. Yu, W. Wei, E. Danner, R. K. Ashley, J. N. Israelachvili and J. H. Waite, *Nat. Chem. Biol.*, 2011, **7**, 588–590.
39 S. Nam and D. Mooney, *Chem. Rev.*, 2021, **121**, 11336–11384.
40 W. Wang, Y. Liu and Z. Xie, *J. Bionic Eng.*, 2021, 1–34.
41 F. Liu, X. Liu, F. Chen and Q. Fu, *Prog. Polym. Sci.*, 2021, **123**, 101472.
42 H. Fan and J. P. Gong, *Adv. Mater.*, 2021, **33**, 2102983.
43 X. Liu, H. Yu, L. Wang, Z. Huang, F. Haq, L. Teng, M. Jin and B. Ding, *Adv. Mater. Interfaces*, 2022, **9**, 2101038.
44 W. Zhang, R. Wang, Z. Sun, X. Zhu, Q. Zhao, T. Zhang, A. Cholewinski, F. K. Yang, B. Zhao and R. Pinnaratip, *Chem. Soc. Rev.*, 2020, **49**, 433–464.
45 F. Meng, Q. Liu, X. Wang, D. Tan, L. Xue and W. J. P. Barnes, *Philos. Trans. R. Soc., A*, 2019, **377**, 20190131.
46 M. Liu, S. Wang and L. Jiang, *Nat. Rev. Mater.*, 2017, **2**, 1–17.
47 A. K. Geim, S. Dubonos, I. Grigorieva, K. Novoselov, A. Zhukov and S. Y. Shapoval, *Nat. Mater.*, 2003, **2**, 461–463.
48 G. Carbone and E. Pierro, *Small*, 2012, **8**, 1449–1454.
49 Y. W. Lee, S. Chun, D. Son, X. Hu, M. Schneider and M. Sitti, *Adv. Mater.*, 2022, **34**, 2109325.
50 Y.-C. Chen and H. Yang, *ACS Nano*, 2017, **11**, 5332–5338.
51 S. Baik, J. Kim, H. J. Lee, T. H. Lee and C. Pang, *Adv. Sci.*, 2018, **5**, 1800100.
52 S. Chun, D. W. Kim, S. Baik, H. J. Lee, J. H. Lee, S. H. Bhang and C. Pang, *Adv. Funct. Mater.*, 2018, **28**, 1805224.
53 H. Chen, L. Zhang, D. Zhang, P. Zhang and Z. Han, *ACS Appl. Mater. Interfaces*, 2015, **7**, 13987–13995.
54 B. Yang, N. Ayyadurai, H. Yun, Y. S. Choi, B. H. Hwang, J. Huang, Q. Lu, H. Zeng and H. J. Cha, *Angew. Chem.*, 2014, **126**, 13578–13582.
55 S. Kim, J. Huang, Y. Lee, S. Dutta, H. Y. Yoo, Y. M. Jung, Y. Jho, H. Zeng and D. S. Hwang, *Proc. Natl. Acad. Sci. U. S. A.*, 2016, **113**, E847–E853.
56 W. Wei, L. Petrone, Y. Tan, H. Cai, J. N. Israelachvili, A. Miserez and J. H. Waite, *Adv. Funct. Mater.*, 2016, **26**, 3496–3507.
57 Y. Ma, S. Ma, Y. Wu, X. Pei, S. N. Gorb, Z. Wang, W. Liu and F. Zhou, *Adv. Mater.*, 2018, **30**, 1801595.
58 Y. Zhao, S. Song, X. Ren, J. Zhang, Q. Lin and Y. Zhao, *Chem. Rev.*, 2022, **122**, 5604–5640.
59 J. Li and D. J. Mooney, *Nat. Rev. Mater.*, 2016, **1**, 1–17.
60 O. Chaudhuri, L. Gu, D. Klumpers, M. Darnell, S. A. Bencherif, J. C. Weaver, N. Huebsch, H.-P. Lee, E. Lippens and G. N. Duda, *Nat. Mater.*, 2016, **15**, 326–334.
61 B. Hu, C. Owh, P. L. Chee, W. R. Leow, X. Liu, Y.-L. Wu, P. Guo, X. J. Loh and X. Chen, *Chem. Soc. Rev.*, 2018, **47**, 6917–6929.
62 C. Yang and Z. Suo, *Nat. Rev. Mater.*, 2018, **3**, 125–142.
63 H. Yuk, B. Lu and X. Zhao, *Chem. Soc. Rev.*, 2019, **48**, 1642–1667.
64 M. Li, Q. Guan, C. Li and E. Saiz, *Device*, 2023, **1**, 100007.
65 T. Kim, J. Park, J. Sohn, D. Cho and S. Jeon, *ACS Nano*, 2016, **10**, 4770–4778.
66 S. Wang, H. Luo, C. Linghu and J. Song, *Adv. Funct. Mater.*, 2021, **31**, 2009217.
67 W. Ruotolo, D. Brouwer and M. R. Cutkosky, *Sci. Rob.*, 2021, **6**, eabi9773.
68 H. Zhang, Y. Liu, H. Lai, Z. Cheng, Z. Fan, X. Yu, J. Wang, Z. Xie and H. Tan, *Chem. Eng. J.*, 2021, **417**, 128072.
69 X. Wang, B. Yang, D. Tan, Q. Li, B. Song, Z.-S. Wu, A. del Campo, M. Kappl, Z. Wang and S. N. Gorb, *Mater. Today*, 2020, **35**, 42–49.
70 Z. Yu, B. Yang, S. X. Yang and Z. Dai, *Int. J. Robot. Autom.*, 2017, **32**, 425–431.
71 S. Song, D.-M. Drotlef, C. Majidi and M. Sitti, *Proc. Natl. Acad. Sci. U. S. A.*, 2017, **114**, E4344–E4353.
72 S. Xia, Y. Chen, J. Tian, J. Shi, C. Geng, H. Zou, M. Liang and Z. Li, *Adv. Funct. Mater.*, 2021, **31**, 2101143.
73 Z. Gu, S. Li, F. Zhang and S. Wang, *Adv. Sci.*, 2016, **3**, 1500327.
74 F. London, *Trans. Faraday Soc.*, 1937, **33**, 8b–26.
75 J. N. Israelachvili, *Intermolecular and surface forces*, Academic press, 2011.
76 S. Hu and Z. Xia, *Small*, 2012, **8**, 2464–2468.
77 K. L. Mittal and R. Jaiswal, *Particle adhesion and removal*, John Wiley & Sons, 2015.
78 R. G. Horn and D. T. Smith, *Science*, 1992, **256**, 362–364.
79 R. G. Horn, D. Smith and A. Grabbe, *Nature*, 1993, **366**, 442–443.
80 D. Ruffatto III, A. Parness and M. Spenko, *J. R. Soc., Interface*, 2014, **11**, 20131089.
81 J. R. Regalbuto, *Synth. Solid Catal.*, 2009, 33–58.
82 G. E. Pake, *J. Chem. Phys.*, 1948, **16**, 327–336.
83 L. Rayleigh, *Nature*, 1891, **43**, 437–439.
84 M. Li, C. Li, B. R. Blackman and S. Eduardo, *Int. Mater. Rev.*, 2022, **67**, 658–681.
85 C. Li, M. Li, Z. Ni, Q. Guan, B. R. Blackman and E. Saiz, *J. R. Soc., Interface*, 2021, **18**, 20210162.
86 M. Li, S. Zhou, Q. Guan, W. Li, C. Li, F. Bouville, H. Bai and E. Saiz, *ACS Appl. Mater. Interfaces*, 2022, **14**, 46077–46085.
87 L. F. Da Silva, A. Öchsner and R. D. Adams, *Handbook of adhesion technology*, Springer Science & Business Media, 2011.
88 A. Faghihnejad, K. E. Feldman, J. Yu, M. V. Tirrell, J. N. Israelachvili, C. J. Hawker, E. J. Kramer and H. Zeng, *Adv. Funct. Mater.*, 2014, **24**, 2322–2333.
89 H. Brown, *Annu. Rev. Mater. Sci.*, 1991, **21**, 463–489.
90 R. A. Bowling and K. L. Mittal, in *Particles on surfaces 1: Detection, adhesion, and removal*, ed. K. L. Mittal, Springer, Boston, MA, 1988, vol. 2, p. 129.
91 M. C. Michalski, S. Desobry and J. Hardy, *Crit. Rev. Food Sci. Nutr.*, 1997, **37**, 591–619.
92 S. Gorb, *Attachment devices of insect cuticle*, Springer Science & Business Media, 2001.
93 S. Gorb and V. Popov, *Philos. Trans. R. Soc., A*, 2002, **360**, 211–225.
94 K. Wang, W. Wang, H. Zhang and J. Fang, *Vacuum*, 2012, **86**, 1783–1788.
95 T. Maie, H. L. Schoenfuss and R. W. Blob, *J. Exp. Biol.*, 2012, **215**, 3925–3936.

96 L. F. M. da Silva, A. Öchsner and R. D. Adams, *Handbook of adhesion technology*, Springer, 2011.
97 J. Chen, Q. Peng, J. Liu and H. Zeng, *Langmuir*, 2023, **39**, 17600–17610.
98 T. Young, *Philos. Trans. R. Soc. London*, 1805, 65–87.
99 H. Chen, P. Zhang, L. Zhang, H. Liu, Y. Jiang, D. Zhang, Z. Han and L. Jiang, *Nature*, 2016, **532**, 85–89.
100 W. Barthlott, T. Schimmel, S. Wiersch, K. Koch, M. Brede, M. Barczewski, S. Walheim, A. Weis, A. Kaltenmaier and A. Leder, *Adv. Mater.*, 2010, **22**, 2325–2328.
101 C. Furmidge, *J. Colloid Sci.*, 1962, **17**, 309–324.
102 L. Feng, Y. Zhang, J. Xi, Y. Zhu, N. Wang, F. Xia and L. Jiang, *Langmuir*, 2008, **24**, 4114–4119.
103 L. Feng, S. Li, Y. Li, H. Li, L. Zhang, J. Zhai, Y. Song, B. Liu, L. Jiang and D. Zhu, *Adv. Mater.*, 2002, **14**, 1857–1860.
104 L. Gao and T. J. McCarthy, *Langmuir*, 2006, **22**, 2966–2967.
105 A. Lafuma and D. Quéré, *Nat. Mater.*, 2003, **2**, 457–460.
106 F. Xia and L. Jiang, *Adv. Mater.*, 2008, **20**, 2842–2858.
107 J. Li, Z. Jing, F. Zha, Y. Yang, Q. Wang and Z. Lei, *ACS Appl. Mater. Interfaces*, 2014, **6**, 8868–8877.
108 E. Bormashenko, *Colloids Surf., A*, 2009, **345**, 163–165.
109 Z. Cheng, M. Du, H. Lai, N. Zhang and K. Sun, *Nanoscale*, 2013, **5**, 2776–2783.
110 J. Yong, Q. Yang, F. Chen, D. Zhang, G. Du, H. Bian, J. Si, F. Yun and X. Hou, *Appl. Surf. Sci.*, 2014, **288**, 579–583.
111 S. Wang and L. Jiang, *Adv. Mater.*, 2007, **19**, 3423–3424.
112 S.-M. Lee and T. H. Kwon, *J. Micromech. Microeng.*, 2007, **17**, 687.
113 S. Tian, L. Li, W. Sun, X. Xia, D. Han, J. Li and C. Gu, *Sci. Rep.*, 2012, **2**, 511.
114 H. Y. Erbil and C. E. Cansoy, *Langmuir*, 2009, **25**, 14135–14145.
115 K. Li, X. Zeng, H. Li, X. Lai, C. Ye and H. Xie, *Appl. Surf. Sci.*, 2013, **279**, 458–463.
116 H. S. Grewal, I.-J. Cho, J.-E. Oh and E.-S. Yoon, *Nanoscale*, 2014, **6**, 15321–15332.
117 R. Hensel, A. Finn, R. Helbig, S. Killge, H.-G. Braun and C. Werner, *Langmuir*, 2014, **30**, 15162–15170.
118 E. Søgaard, N. K. Andersen, K. Smistrup, S. T. Larsen, L. Sun and R. Taboryski, *Langmuir*, 2014, **30**, 12960–12968.
119 N. A. Patankar, *Langmuir*, 2004, **20**, 7097–7102.
120 D. Bartolo, F. Bouamrirene, E. Verneuil, A. Buguin, P. Silberzan and S. Moulinet, *Europhys. Lett.*, 2006, **74**, 299.
121 Y. C. Jung and B. Bhushan, *Langmuir*, 2009, **25**, 9208–9218.
122 T. Koishi, K. Yasuoka, S. Fujikawa, T. Ebisuzaki and X. C. Zeng, *Proc. Natl. Acad. Sci. U. S. A.*, 2009, **106**, 8435–8440.
123 E. Bormashenko, R. Pogreb, G. Whyman and M. Erlich, *Langmuir*, 2007, **23**, 6501–6503.
124 M. Lundgren, N. L. Allan and T. Cosgrove, *Langmuir*, 2007, **23**, 1187–1194.
125 P. Tsai, R. G. Lammertink, M. Wessling and D. Lohse, *Phys. Rev. Lett.*, 2010, **104**, 116102.
126 E. Bormashenko, R. Pogreb, G. Whyman, Y. Bormashenko and M. Erlich, *Appl. Phys. Lett.*, 2007, **90**, 201917.
127 R. J. Vrancken, H. Kusumaatmaja, K. Hermans, A. M. Prenen, O. Pierre-Louis, C. W. Bastiaansen and D. J. Broer, *Langmuir*, 2010, **26**, 3335–3341.
128 E. Bormashenko, Y. Bormashenko, T. Stein, G. Whyman, R. Pogreb and Z. Barkay, *Langmuir*, 2007, **23**, 4378–4382.
129 C. Ran, G. Ding, W. Liu, Y. Deng and W. Hou, *Langmuir*, 2008, **24**, 9952–9955.
130 S. Wang, K. Liu, X. Yao and L. Jiang, *Chem. Rev.*, 2015, **115**, 8230–8293.
131 L. Barbieri, E. Wagner and P. Hoffmann, *Langmuir*, 2007, **23**, 1723–1734.
132 A. Marmur, *Langmuir*, 2004, **20**, 3517–3519.
133 A. Marmur, *Langmuir*, 2003, **19**, 8343–8348.
134 M. Jin, X. Feng, L. Feng, T. Sun, J. Zhai, T. Li and L. Jiang, *Adv. Mater.*, 2005, **17**, 1977–1981.
135 K. Kendall, *J. Phys. D: Appl. Phys.*, 1971, **4**, 1186.
136 K. Autumn, S.-T. Hsieh, D. M. Dudek, J. Chen, C. Chitaphan and R. J. Full, *J. Exp. Biol.*, 2006, **209**, 260–272.
137 T. Endlein, A. Ji, D. Samuel, N. Yao, Z. Wang, W. J. P. Barnes, W. Federle, M. Kappl and Z. Dai, *J. R. Soc., Interface*, 2013, **10**, 20120838.
138 K. L. Johnson, K. Kendall and A. Roberts, *Philos. Trans. R. Soc., A*, 1971, **324**, 301–313.
139 H. Gao, X. Wang, H. Yao, S. Gorb and E. Arzt, *Mech. Mater.*, 2005, **37**, 275–285.
140 H.-H. Park, M. Seong, K. Sun, H. Ko, S. M. Kim and H. E. Jeong, *ACS Macro Lett.*, 2017, **6**, 1325–1330.
141 H.-J. Butt and M. Kappl, *Adv. Colloid Interface Sci.*, 2009, **146**, 48–60.
142 P.-G. Gennes, F. Brochard-Wyart and D. Quéré, *Capillarity and wetting phenomena: drops, bubbles, pearls, waves*, Springer, 2004.
143 G. Noble and M. Jaeckle, *J. Morphol.*, 1928, **45**, 259–292.
144 D. M. Slater, M. J. Vogel, A. M. Macner and P. H. Steen, *J. Adhes. Sci. Technol.*, 2014, **28**, 273–289.
145 A. Narayanan, A. Dhinojwala and A. Joy, *Chem. Soc. Rev.*, 2021, **50**, 13321–13345.
146 D. M. Green and D. L. Barber, *Can. J. Zool.*, 1988, **66**, 1610–1619.
147 S. N. Gorb and M. Varenberg, *J. Adhes. Sci. Technol.*, 2007, **21**, 1175–1183.
148 M. Ferrari, F. Ravera, S. Rao and L. Liggieri, *Appl. Phys. Lett.*, 2006, **89**, 053104.
149 L. Gao and T. J. McCarthy, *J. Am. Chem. Soc.*, 2006, **128**, 9052–9053.
150 R. J. Good, *J. Adhes. Sci. Technol.*, 1992, **6**, 1269–1302.
151 X. Liu, J. Zhou, Z. Xue, J. Gao, J. Meng, S. Wang and L. Jiang, *Adv. Mater.*, 2012, **24**, 3401–3405.
152 L. Lin, M. Liu, L. Chen, P. Chen, J. Ma, D. Han and L. Jiang, *Adv. Mater.*, 2010, **22**, 4826–4830.
153 Y. Yan, Z. Guo, X. Zhang, L. He, Y. Li, K. Liu, J. Cai, D. Tian and L. Jiang, *Adv. Funct. Mater.*, 2018, **28**, 1800775.
154 Y. Chen, J. Meng, Z. Zhu, F. Zhang, L. Wang, Z. Gu and S. Wang, *Langmuir*, 2018, **34**, 6063–6069.
155 X. Y. Dong, M. Pan and H. Zeng, *Langmuir*, 2024, **40**(10), 5444–5454.
156 M. Li, W. Li, Q. Guan, X. Dai, J. Lv, Z. Xia, W.-J. Ong, E. Saiz and X. Hou, *ACS Nano*, 2021, **15**, 19194–19201.
157 Y. Chen, Z. Zhu, M. Steinhart and S. N. Gorb, *Iscience*, 2022, **25**, 103864.

158 D. Gan, W. Xing, L. Jiang, J. Fang, C. Zhao, F. Ren, L. Fang, K. Wang and X. Lu, *Nat. Commun.*, 2019, **10**, 1487.
159 P. Karami, C. S. Wyss, A. Khoushabi, A. Schmocker, M. Broome, C. Moser, P.-E. Bourban and D. P. Pioletti, *ACS Appl. Mater. Interfaces*, 2018, **10**, 38692–38699.
160 L. C. Bradley, N. D. Bade, L. M. Mariani, K. T. Turner, D. Lee and K. J. Stebe, *ACS Appl. Mater. Interfaces*, 2017, **9**, 27409–27413.
161 R. Rahimi, *Adv. Healthcare Mater.*, 2018, **7**, 1800231.
162 Q. Zhang, X. Liu, L. Duan and G. Gao, *Chem. Eng. J.*, 2019, **365**, 10–19.
163 D. Arunbabu, H. Shahsavan, W. Zhang and B. Zhao, *J. Phys. Chem. B*, 2013, **117**, 441–449.
164 A. Cholewinski, F. K. Yang and B. Zhao, *Langmuir*, 2017, **33**, 8353–8361.
165 Y. Hong, F. Zhou, Y. Hua, X. Zhang, C. Ni, D. Pan, Y. Zhang, D. Jiang, L. Yang and Q. Lin, *Nat. Commun.*, 2019, **10**, 2060.
166 F. J. Chaves, L. Da Silva, M. De Moura, D. Dillard and V. Esteves, *J. Adhesion*, 2014, **90**, 955–992.
167 Y. Qiao, D. R. Merkel, E. K. Nickerson, Y. Shin, R. J. Seffens, A. Ortiz and K. L. Simmons, *Composites, Part A*, 2022, **160**, 107025.
168 Y. Wang, X. Yang, G. Nian and Z. Suo, *J. Mech. Phys. Solids*, 2020, **143**, 103988.
169 J. Yang, R. Bai, B. Chen and Z. Suo, *Adv. Funct. Mater.*, 2020, **30**, 1901693.
170 S. Blacklow, J. Li, B. Freedman, M. Zeidi, C. Chen and D. Mooney, *Sci. Adv.*, 2019, **5**, eaaw3963.
171 T. Zhang, H. Yuk, S. Lin, G. A. Parada and X. Zhao, *Acta Mech. Sin.*, 2017, **33**, 543–554.
172 K. R. Shull, *Mater. Sci. Eng., R*, 2002, **36**, 1–45.
173 G. Sudre, L. Olanier, Y. Tran, D. Hourdet and C. Creton, *Soft Matter*, 2012, **8**, 8184–8193.
174 K. J. Tong and D. M. Ebenstein, *JOM*, 2015, **67**, 713–719.
175 R. E. Webber and K. R. Shull, *Macromolecules*, 2004, **37**, 6153–6160.
176 Y. Sekiguchi, M. Katano and C. Sato, *J. Adhesion*, 2017, **93**, 235–255.
177 A. ASTM, ASTM International, West Conshohocken, PA, 2007.
178 H. Yuk, T. Zhang, S. Lin, G. A. Parada and X. Zhao, *Nat. Mater.*, 2016, **15**, 190–196.
179 C. Creton and M. Ciccotti, *Rep. Prog. Phys.*, 2016, **79**, 046601.
180 H. Yuk, T. Zhang, G. A. Parada, X. Liu and X. Zhao, *Nat. Commun.*, 2016, **7**, 12028.
181 M. Li, W. Li, Q. Guan, J. Lv, Z. Wang, L. Ding, C. Li, E. Saiz and X. Hou, *Device*, 2023, **1**, 100006.
182 S. Rose, A. Prevoteau, P. Elzière, D. Hourdet, A. Marcellan and L. Leibler, *Nature*, 2014, **505**, 382–385.
183 J. Liu, S. Lin, X. Liu, Z. Qin, Y. Yang, J. Zang and X. Zhao, *Nat. Commun.*, 2020, **11**, 1071.
184 H. Yuk, S. Lin, C. Ma, M. Takaffoli, N. X. Fang and X. Zhao, *Nat. Commun.*, 2017, **8**, 14230.
185 D. Wirthl, R. Pichler, M. Drack, G. Kettlguber, R. Moser, R. Gerstmayr, F. Hartmann, E. Bradt, R. Kaltseis and C. M. Siket, *Sci. Adv.*, 2017, **3**, e1700053.
186 J. Yang, R. Bai and Z. Suo, *Adv. Mater.*, 2018, **30**, 1800671.
187 P. Rao, T. L. Sun, L. Chen, R. Takahashi, G. Shinohara, H. Guo, D. R. King, T. Kurokawa and J. P. Gong, *Adv. Mater.*, 2018, **30**, 1801884.
188 W. Li, Q. Guan, M. Li, E. Saiz and X. Hou, *Prog. Polym. Sci.*, 2023, **140**, 101665.
189 S. Yang, J. Ju, Y. Qiu, Y. He, X. Wang, S. Dou, K. Liu and L. Jiang, *Small*, 2014, **10**, 294–299.
190 K. Autumn, P. H. Niewiarowski and J. B. Puthoff, *Annu. Rev. Ecol., Evol. Syst.*, 2014, **45**, 445–470.
191 M. J. Moon and J. G. Park, *Anim. Cells Syst.*, 2009, **13**, 161–167.
192 J. Billen, M. S. Al-Khalifa and R. R. Silva, *Saudi J. Biol. Sci.*, 2017, **24**, 830–836.
193 W. M. Kier and A. M. Smith, *Integr. Comp. Biol.*, 2002, **42**, 1146–1153.
194 K. E. Cohen, B. E. Flammang, C. H. Crawford and L. P. Hernandez, *R. Soc. Open Sci.*, 2020, **7**, 190990.
195 D. K. Wainwright, T. Kleinteich, A. Kleinteich, S. N. Gorb and A. P. Summers, *Biol. Lett.*, 2013, **9**, 20130234.
196 D. M. Drotlef, E. Appel, H. Peisker, K. Dening, A. Del Campo, S. N. Gorb and W. J. P. Barnes, *Interface Focus*, 2015, **5**, 20140036.
197 M. Varenberg, N. M. Pugno and S. N. Gorb, *Soft Matter*, 2010, **6**, 3269–3272.
198 P. Ditsche-Kuru, J. Koop and S. Gorb, *J. Exp. Biol.*, 2010, **213**, 1950–1959.
199 D. Das and T. C. Nag, *Zoology*, 2006, **109**, 300–309.
200 M. Johal and Y. Rawal, *Curr. Sci.*, 2003, **85**, 1273–1275.
201 B. P. Lee, P. B. Messersmith, J. N. Israelachvili and J. H. Waite, *Annu. Rev. Mater. Res.*, 2011, **41**, 99–132.
202 C. Lee, S. E. Choi, J. W. Kim and S. Y. Lee, *Small*, 2020, **16**, 1904282.
203 R. J. Stewart, C. S. Wang, I. T. Song and J. P. Jones, *Adv. Colloid Interface Sci.*, 2017, **239**, 88–96.
204 S. Deng, W. Shang, S. Feng, S. Zhu, Y. Xing, D. Li, Y. Hou and Y. Zheng, *Sci. Rep.*, 2017, **7**, 45687.
205 Y. Shao, J. Zhao, Y. Fan, Z. Wan, L. Lu, Z. Zhang, W. Ming and L. Ren, *Chem. Eng. J.*, 2020, **382**, 122989.
206 Y. Zheng, C. Zhang, J. Wang, Y. Liu, C. Shen and J. Yang, *J. Colloid Interface Sci.*, 2019, **557**, 737–745.
207 R. D. Mukhopadhyay, B. Vedhanarayanan and A. Ajayaghosh, *Angew. Chem., Int. Ed.*, 2017, **129**, 16234–16238.
208 B. Bhushan and E. K. Her, *Langmuir*, 2010, **26**, 8207–8217.
209 R. Qu, W. Zhang, X. Li, Y. Liu, Y. Wei, L. Feng and L. Jiang, *ACS Appl. Mater. Interfaces*, 2020, **12**, 6309–6318.
210 Y. Yang, X. Li, X. Zheng, Z. Chen, Q. Zhou and Y. Chen, *Adv. Mater.*, 2018, **30**, 1704912.
211 D. Zheng, Y. Jiang, W. Yu, X. Jiang, X. Zhao, C.-H. Choi and G. Sun, *Langmuir*, 2017, **33**, 13640–13648.
212 K. Zhou, D. Li, P. Xue, P. Wang, Y. Zhao and M. Jin, *Colloids Surf., A*, 2020, **590**, 124517.
213 M. Amabili, A. Giacomello, S. Meloni and C. M. Casciola, *Adv. Mater. Interfaces*, 2015, **2**, 1500248.
214 M. J. Mayser, H. F. Bohn, M. Reker and W. Barthlott, *Beilstein J. Nanotechnol.*, 2014, **5**, 812–821.

215 Y. Xiang, S. Huang, T.-Y. Huang, A. Dong, D. Cao, H. Li, Y. Xue, P. Lv and H. Duan, *Proc. Natl. Acad. Sci. U. S. A.*, 2020, **117**, 2282–2287.
216 W. Federle, *Comp. Biochem. Physiol., Part A: Mol. Integr. Physiol.*, 2006, **143**(4), S86–S87.
217 X. Li, D. Tao, H. Lu, P. Bai, Z. Liu, L. Ma, Y. Meng and Y. Tian, *Surf. Topogr.: Metrol. Prop.*, 2019, **7**, 023001.
218 M. Culler, K. A. Ledford and J. H. Nadler, *MRS Online Proc. Libr.*, 2014, **1648**, mrsf13-1648-hh10-02.
219 M. Beckert, B. E. Flammang and J. H. Nadler, *J. Exp. Biol.*, 2015, **218**, 3551–3558.
220 R. Britz and G. D. Johnson, *J. Morphol.*, 2012, **273**, 1353–1366.
221 E. Pennisi, *Science*, 2012, 277.
222 P. Ditsche, D. K. Wainwright and A. P. Summers, *J. Exp. Biol.*, 2014, **217**, 2548–2554.
223 H. H. Abd-Elhafeez and D. M. Mokhtar, *J. Adv. Microsc. Res.*, 2014, **9**, 275–284.
224 T. Geerinckx, J. De Poorter and D. Adriaens, *J. Morphol.*, 2007, **268**, 805–814.
225 C. Gerstner, *Can. J. Zool.*, 2007, **85**, 133–140.
226 T. Geerinckx, A. Herrel and D. Adriaens, *J. Exp. Zool., Part A*, 2011, **315**, 121–131.
227 Y.-C. Chuang, H.-K. Chang, G.-L. Liu and P.-Y. Chen, *J. Mech. Behav. Biomed. Mater.*, 2017, **73**, 76–85.
228 B. N. Persson, *J. Phys.: Condens. Matter*, 2007, **19**, 376110.
229 W. J. P. Barnes, *MRS Bull.*, 2007, **32**, 479–485.
230 G. Hanna, W. Jon and W. J. Barnes, *J. Exp. Biol.*, 1991, **155**, 103–125.
231 S. B. Emerson and D. Diehl, *Biol. J. Linn. Soc.*, 1980, **13**, 199–216.
232 V. V. Ernst, *Tissue Cell*, 1973, **5**, 83–96.
233 U. Welsch, V. Storch and W. Fuchs, *Cell Tissue Res.*, 1974, **148**, 407–416.
234 D. M. Green, *Can. J. Zool.*, 1979, **57**, 2033–2046.
235 G. Walker, A. Yulf and J. Ratcliffe, *J. Zool.*, 1985, **205**, 297–307.
236 P. Ditsche-Kuru and J. H. Koop, *Aquatic Insects*, 2009, **31**, 495–506.
237 P. Ditsche-Kuru, W. Barthlott and J. H. Koop, *Zoology*, 2012, **115**, 379–388.
238 R. J. Stewart, C. S. Wang and H. Shao, *Adv. Colloid Interface Sci.*, 2011, **167**, 85–93.
239 R. J. Stewart, T. C. Ransom and V. Hlady, *J. Polym. Sci., Part B: Polym. Phys.*, 2011, **49**, 757–771.
240 T. Steinbrecher, G. Beuchle, B. Melzer, T. Speck, O. Kraft and R. Schwaiger, *Int. J. Plant Sci.*, 2011, **172**, 1120–1129.
241 C. Yonge, *J. Mar. Biol. Assoc. U. K.*, 1962, **42**, 113–125.
242 A. Tamarin and P. Keller, *J. Ultrastruct. Res.*, 1972, **40**, 401–416.
243 A. Tamarin, P. Lewis and J. Askey, *J. Morphol.*, 1974, **142**, 321–327.
244 N. Farsad and E. D. Sone, *J. Struct. Biol.*, 2012, **177**, 613–620.
245 J. Waite and M. Tanzer, *Biochem. Biophys. Res. Commun.*, 1980, **96**, 1554–1561.
246 J. Waite and M. Tanzer, *Anal. Biochem.*, 1981, **111**, 131–136.
247 S. Seo, D. W. Lee, J. S. Ahn, K. Cunha, E. Filippidi, S. W. Ju, E. Shin, B. S. Kim, Z. A. Levine and R. D. Lins, *Adv. Mater.*, 2017, **29**, 1703026.
248 M. J. Sever, J. T. Weisser, J. Monahan, S. Srinivasan and J. J. Wilker, *Angew. Chem., Int. Ed.*, 2004, **43**, 448–450.
249 H. Lee, N. F. Scherer and P. B. Messersmith, *Proc. Natl. Acad. Sci. U. S. A.*, 2006, **103**, 12999–13003.
250 G. P. Maier, M. V. Rapp, J. H. Waite, J. N. Israelachvili and A. Butler, *Science*, 2015, **349**, 628–632.
251 T. Priemel, E. Degtyar, M. N. Dean and M. J. Harrington, *Nat. Commun.*, 2017, **8**, 14539.
252 H. Jiang, E. W. Hawkes, C. Fuller, M. A. Estrada, S. A. Suresh, N. Abcouwer, A. K. Han, S. Wang, C. J. Ploch and A. Parness, *Sci. Rob.*, 2017, **2**, eaan4545.
253 X. Liu, H. Gu, M. Wang, X. Du, B. Gao, A. Elbaz, L. Sun, J. Liao, P. Xiao and Z. Gu, *Adv. Mater.*, 2018, **30**, 1800103.
254 Z. Dong, M. F. Schumann, M. J. Hokkanen, B. Chang, A. Welle, Q. Zhou, R. H. Ras, Z. Xu, M. Wegener and P. A. Levkin, *Adv. Mater.*, 2018, **30**, 1803890.
255 D. H. Kim, S. Kim, S. R. Park, N. X. Fang and Y. T. Cho, *ACS Appl. Mater. Interfaces*, 2021, **13**, 33618–33626.
256 J. Sun, P. Zhu, X. Yan, C. Zhang, Y. Jin, X. Chen and Z. Wang, *Appl. Phys. Rev.*, 2021, **8**, 031403.
257 C. Li, N. Li, X. Zhang, Z. Dong, H. Chen and L. Jiang, *Angew. Chem., Int. Ed.*, 2016, **55**, 14988–14992.
258 V. Liimatainen, D. M. Drotlef, D. Son and M. Sitti, *Adv. Mater.*, 2020, **32**, 2000497.
259 H. Lee, B. P. Lee and P. B. Messersmith, *Nature*, 2007, **448**, 338–341.
260 M. Shin, S.-G. Park, B.-C. Oh, K. Kim, S. Jo, M. S. Lee, S. S. Oh, S.-H. Hong, E.-C. Shin and K.-S. Kim, *Nat. Mater.*, 2017, **16**, 147–152.
261 S. Baik, H. J. Lee, D. W. Kim, J. W. Kim, Y. Lee and C. Pang, *Adv. Mater.*, 2019, **31**, 1803309.
262 J. Saiz-Poseu, J. Mancebo-Aracil, F. Nador, F. Busqué and D. Ruiz-Molina, *Angew. Chem., Int. Ed.*, 2019, **58**, 696–714.
263 J. Li, X. Zhou, J. Li, L. Che, J. Yao, G. McHale, M. K. Chaudhury and Z. Wang, *Sci. Adv.*, 2017, **3**, eaao3530.
264 T. L. Liu and C.-J. C. Kim, *Science*, 2014, **346**, 1096–1100.
265 A. Tuteja, W. Choi, M. Ma, J. M. Mabry, S. A. Mazzella, G. C. Rutledge, G. H. McKinley and R. E. Cohen, *Science*, 2007, **318**, 1618–1622.
266 R. Hensel, A. Finn, R. Helbig, H.-G. Braun, C. Neinhuis, W.-J. Fischer and C. Werner, *Adv. Mater.*, 2013, **26**, 2029–2033.
267 Y. Wu, S. Zhou, B. You and L. Wu, *ACS Nano*, 2017, **11**, 8265–8272.
268 N. Vogel, R. A. Belisle, B. Hatton, T.-S. Wong and J. Aizenberg, *Nat. Commun.*, 2013, **4**, 2176.
269 Y. Wang, M. Zhang, Y. Lai and L. Chi, *Nano Today*, 2018, **22**, 36–61.
270 Y. Chen, J. Meng, Z. Zhu, F. Zhang, L. Wang, Z. Gu, L. Jiang and S. Wang, *Adv. Funct. Mater.*, 2018, **28**, 1800240.
271 W. Wang, S. You, X. Gong, D. Qi, B. K. Chandran, L. Bi, F. Cui and X. Chen, *Adv. Mater.*, 2015, **28**, 270–275.
272 P. Zhu, T. Kong, X. Tang and L. Wang, *Nat. Commun.*, 2017, **8**, 15823.

273 X. Han, X. Tang, R. Chen, W. Li, P. Zhu and L. Wang, *Chem. Eng. J.*, 2021, **420**, 129599.
274 P. Zhu, T. Kong, C. Zhou, L. Lei and L. Wang, *Small Methods*, 2018, **2**, 1800017.
275 W. Li, M. Yu, J. Sun, K. Mochizuki, S. Chen, H. Zheng, J. Li, S. Yao, H. Wu and B. S. Ong, *Proc. Natl. Acad. Sci. U. S. A.*, 2019, **116**, 23909–23914.
276 H. Hu, H. Tian, J. Shao, Y. Wang, X. Li, Y. Tian, Y. Ding and B. Lu, *Adv. Mater. Interfaces*, 2017, **4**, 1700016.
277 X. Li, X. Li, L. Li, T. Sun, Y. Meng and Y. Tian, *Smart Mater. Struct.*, 2021, **30**, 115003.
278 M. Li, Q. Xu, X. Wu, W. Li, W. Lan, L. Heng, J. Street and Z. Xia, *ACS Appl. Mater. Interfaces*, 2018, **10**, 26787–26794.
279 H. Yi, M. Seong, K. Sun, I. Hwang, K. Lee, C. Cha, T. I. Kim and H. E. Jeong, *Adv. Funct. Mater.*, 2018, **28**, 1706498.
280 H. Yi, S. H. Lee, M. Seong, M. K. Kwak and H. E. Jeong, *J. Mater. Chem. B*, 2018, **6**, 8064–8070.
281 L. Qu, L. Dai, M. Stone, Z. Xia and Z. L. Wang, *Science*, 2008, **322**, 238–242.
282 W. Cheng, X. Zeng, H. Chen, Z. Li, W. Zeng, L. Mei and Y. Zhao, *ACS Nano*, 2019, **13**, 8537–8565.
283 J. Saiz-Poseu, J. Mancebo-Aracil, F. Nador, F. Busque and D. Ruiz-Molina, *Angew. Chem., Int. Ed.*, 2019, **58**(3), 696–714.
284 L. Q. Xu, K.-G. Neoh and E.-T. Kang, *Prog. Polym. Sci.*, 2018, **87**, 165–196.
285 C. Cui and W. Liu, *Prog. Polym. Sci.*, 2021, **116**, 101388.
286 Z. Wang, H.-C. Yang, F. He, S. Peng, Y. Li, L. Shao and S. B. Darling, *Matter*, 2019, **1**, 115–155.
287 Z. Dong, L. Feng, Y. Hao, M. Chen, M. Gao, Y. Chao, H. Zhao, W. Zhu, J. Liu and C. Liang, *J. Am. Chem. Soc.*, 2018, **140**, 2165–2178.
288 F. Ponzio, J. Barthès, J. Bour, M. Michel, P. Bertani, J. Hemmerlé, M. d'Ischia and V. Ball, *Chem. Mater.*, 2016, **28**, 4697–4705.
289 T.-P. Chen, T. Liu, T.-L. Su and J. Liang, *Langmuir*, 2017, **33**, 5863–5871.
290 C. Xie, X. Wang, H. He, Y. Ding and X. Lu, *Adv. Funct. Mater.*, 2020, **30**, 1909954.
291 H. A. Lee, Y. Ma, F. Zhou, S. Hong and H. Lee, *Acc. Chem. Res.*, 2019, **52**, 704–713.
292 H. A. Lee, E. Park and H. Lee, *Adv. Mater.*, 2020, **32**, 1907505.
293 C. Musial, A. Kuban-Jankowska and M. Gorska-Ponikowska, *Int. J. Mol. Sci.*, 2020, **21**, 1744.
294 H. Liang, B. Zhou, D. Wu, J. Li and B. Li, *Adv. Colloid Interface Sci.*, 2019, **272**, 102019.
295 Z. Jia, M. Wen, Y. Cheng and Y. Zheng, *Adv. Funct. Mater.*, 2021, **31**, 2008821.
296 X. Zhang, Z. Li, P. Yang, G. Duan, X. Liu, Z. Gu and Y. Li, *Mater. Horiz.*, 2021, **8**, 145–167.
297 J. Guo, B. L. Tardy, A. J. Christofferson, Y. Dai, J. J. Richardson, W. Zhu, M. Hu, Y. Ju, J. Cui and R. R. Dagastine, *Nat. Nanotechnol.*, 2016, **11**, 1105–1111.
298 H. Ejima, J. J. Richardson, K. Liang, J. P. Best, M. P. van Koeverden, G. K. Such, J. Cui and F. Caruso, *Science*, 2013, **341**, 154–157.
299 T. S. Sileika, D. G. Barrett, R. Zhang, K. H. A. Lau and P. B. Messersmith, *Angew. Chem., Int. Ed.*, 2013, **52**, 10766.
300 R. A. Olson, A. B. Korpusik and B. S. Sumerlin, *Chem. Sci.*, 2020, **11**, 5142–5156.
301 H. Q. Song, Y. Fan, Y. Hu, G. Cheng and F. J. Xu, *Adv. Funct. Mater.*, 2021, **31**, 2005978.
302 Y. Lee, K. Sugihara, M. G. Gillilland III, S. Jon, N. Kamada and J. J. Moon, *Nat. Mater.*, 2020, **19**, 118–126.
303 L. T. Nguyen, C.-C. Hsu, H. Ye and Z. Cui, *Biomed. Mater.*, 2020, **15**, 055005.
304 S. Huang, H. Liu, K. Liao, Q. Hu, R. Guo and K. Deng, *ACS Appl. Mater. Interfaces*, 2020, **12**, 28952–28964.
305 C. Zhou, H.-Y. Ao, X. Han, W.-W. Jiang, Z.-F. Yang, L. Ma, X.-Y. Deng and Y.-Z. Wan, *Carbohydr. Polym.*, 2021, **258**, 117683.
306 S. Zhang, J. Hou, Q. Yuan, P. Xin, H. Cheng, Z. Gu and J. Wu, *Chem. Eng. J.*, 2020, **392**, 123775.
307 S. Talebian, M. Mehrali, N. Taebnia, C. P. Pennisi, F. B. Kadumudi, J. Foroughi, M. Hasany, M. Nikkhah, M. Akbari and G. Orive, *Adv. Sci.*, 2019, **6**, 1801664.
308 M. A. Mohamed, A. Fallahi, A. M. El-Sokkary, S. Salehi, M. A. Akl, A. Jafari, A. Tamayol, H. Fenniri, A. Khademhosseini and S. T. Andreadis, *Prog. Polym. Sci.*, 2019, **98**, 101147.
309 C. Hu, L. Long, J. Cao, S. Zhang and Y. Wang, *Chem. Eng. J.*, 2021, **411**, 128564.
310 D. Zhou, S. Li, M. Pei, H. Yang, S. Gu, Y. Tao, D. Ye, Y. Zhou, W. Xu and P. Xiao, *ACS Appl. Mater. Interfaces*, 2020, **12**, 18225–18234.
311 J. Liu, H. Yong, Y. Liu and R. Bai, *Int. J. Biol. Macromol.*, 2020, **156**, 1539–1555.
312 M. Curcio, F. Puoci, F. Iemma, O. I. Parisi, G. Cirillo, U. G. Spizzirri and N. Picci, *J. Agric. Food Chem.*, 2009, **57**, 5933–5938.
313 D. Arizmendi-Cotero, R. M. Gómez-Espinosa, O. D. García, V. Gómez-Vidales and A. Dominguez-Lopez, *Carbohydr. Polym.*, 2016, **136**, 350–357.
314 D. D. Nguyen, L.-J. Luo, S. J. Lue and J.-Y. Lai, *Carbohydr. Polym.*, 2020, **231**, 115770.
315 Y. Jing, Y. Diao and X. Yu, *React. Funct. Polym.*, 2019, **135**, 16–22.
316 H.-H. Park, S.-C. Ko, G.-W. Oh, Y.-M. Jang, Y.-M. Kim, W. S. Park, I.-W. Choi and W.-K. Jung, *Carbohydr. Polym.*, 2018, **198**, 197–205.
317 A. Del Campo, C. Greiner, I. Alvarez and E. Arzt, *Adv. Mater.*, 2007, **19**, 1973–1977.
318 L. Xue, A. Kovalev, F. Thöle, G. T. Rengarajan, M. Steinhart and S. N. Gorb, *Langmuir*, 2012, **28**, 10781–10788.
319 S. Gorb, M. Varenberg, A. Peressadko and J. Tuma, *J. R. Soc., Interface*, 2007, **4**, 271–275.
320 C. Greiner, A. Del Campo and E. Arzt, *Langmuir*, 2007, **23**, 3495–3502.
321 H. Gao, B. Ji, I. L. Jäger, E. Arzt and P. Fratzl, *Proc. Natl. Acad. Sci. U. S. A.*, 2003, **100**, 5597–5600.
322 H. Gao and H. Yao, *Proc. Natl. Acad. Sci. U. S. A.*, 2004, **101**, 7851–7856.
323 M. Micciché, E. Arzt and E. Kroner, *ACS Appl. Mater. Interfaces*, 2014, **6**, 7076–7083.

324 B. Aksak, C.-Y. Hui and M. Sitti, *J. R. Soc., Interface*, 2011, **8**, 1166–1175.
325 V. Barreau, R. Hensel, N. K. Guimard, A. Ghatak, R. M. McMeeking and E. Arzt, *Adv. Funct. Mater.*, 2016, **26**, 4687–4694.
326 M. Zhou, Y. Tian, H. Zeng, N. Pesika and J. Israelachvili, *Adv. Mater. Interfaces*, 2015, **2**, 1400466.
327 A. Parness, D. Soto, N. Esparza, N. Gravish, M. Wilkinson, K. Autumn and M. Cutkosky, *J. R. Soc., Interface*, 2009, **6**, 1223–1232.
328 D. M. Drotlef, L. Stepien, M. Kappl, W. J. P. Barnes, H. J. Butt and A. Del Campo, *Adv. Funct. Mater.*, 2013, **23**, 1137–1146.
329 E. Arzt, H. Quan, R. M. McMeeking and R. Hensel, *Prog. Mater. Sci.*, 2021, **120**, 100823.
330 C. B. Dayan, S. Chun, N. Krishna-Subbaiah, D. M. Drotlef, M. B. Akolpoglu and M. Sitti, *Adv. Mater.*, 2021, **33**, 2103826.
331 R. Spolenak, S. Gorb, H. Gao and E. Arzt, *Proc. R. Soc. A*, 2005, **461**, 305–319.
332 A. M. Smith, *J. Exp. Biol.*, 1996, **199**, 949–958.
333 L. Xue, A. Kovalev, A. Eichler-Volf, M. Steinhart and S. N. Gorb, *Nat. Commun.*, 2015, **6**, 6621.
334 S. Armon, E. Efrati, R. Kupferman and E. Sharon, *Science*, 2011, **333**, 1726–1730.
335 A. Rafsanjani, V. Brulé, T. L. Western and D. Pasini, *Sci. Rep.*, 2015, **5**, 8064.
336 H. Hu, H. Tian, X. Li, J. Shao, Y. Ding, H. Liu and N. An, *ACS Appl. Mater. Interfaces*, 2014, **6**, 14167–14173.
337 D. Tan, X. Wang, Q. Liu, K. Shi, B. Yang, S. Liu, Z. S. Wu and L. Xue, *Small*, 2019, **15**, 1904248.
338 H. Yi, M. Kang, M. K. Kwak and H. E. Jeong, *ACS Appl. Mater. Interfaces*, 2016, **8**, 22671–22678.
339 Z. Rong, Y. Zhou, B. Chen, J. Robertson, W. Federle, S. Hofmann and U. Steiner, *Adv. Mater.*, 2014, **26**, 1456–1461.
340 C. T. Bauer, E. Kroner, N. A. Fleck and E. Arzt, *Bioinspiration Biomimetics*, 2015, **10**, 066002.
341 P. Glass, H. Chung, N. R. Washburn and M. Sitti, *Langmuir*, 2010, **26**, 17357–17362.
342 S. H. Lee, H. W. Song, H. J. Park and M. K. Kwak, *Macromol. Rapid Commun.*, 2022, **43**, 2200012.
343 D. Tao, X. Gao, H. Lu, Z. Liu, Y. Li, H. Tong, N. Pesika, Y. Meng and Y. Tian, *Adv. Funct. Mater.*, 2017, **27**, 1606576.
344 H. Hu, H. Tian, J. Shao, X. Li, Y. Wang, Y. Wang, Y. Tian and B. Lu, *ACS Appl. Mater. Interfaces*, 2017, **9**, 7752–7760.
345 Y. Zhang, S. Ma, B. Li, B. Yu, H. Lee, M. Cai, S. N. Gorb, F. Zhou and W. Liu, *Chem. Mater.*, 2021, **33**, 2785–2795.
346 K. Jin, Y. Tian, J. S. Erickson, J. Puthoff, K. Autumn and N. S. Pesika, *Langmuir*, 2012, **28**, 5737–5742.
347 S. Kim and M. Sitti, *Appl. Phys. Lett.*, 2006, **89**, 261911.
348 J. A. Sandoval, S. Jadhav, H. Quan, D. D. Deheyn and M. T. Tolley, *Bioinspiration Biomimetics*, 2019, **14**, 066016.
349 M. Varenberg and S. Gorb, *J. R. Soc., Interface*, 2008, **5**, 383–385.
350 S. H. Lee, H. W. Song, B. S. Kang and M. K. Kwak, *ACS Appl. Mater. Interfaces*, 2019, **11**, 47571–47576.
351 D. W. Kim, S. Baik, H. Min, S. Chun, H. J. Lee, K. H. Kim, J. Y. Lee and C. Pang, *Adv. Funct. Mater.*, 2019, **29**, 1807614.
352 G. Meloni, O. Tricinci, A. Degl'Innocenti and B. Mazzolai, *Sci. Rep.*, 2020, **10**, 15480.
353 Y. Wang, V. Kang, W. Federle, E. Arzt and R. Hensel, *Adv. Mater. Interfaces*, 2020, **7**, 2001269.
354 Y. Wang, V. Kang, E. Arzt, W. Federle and R. Hensel, *ACS Appl. Mater. Interfaces*, 2019, **11**, 26483–26490.
355 B. He, Z. Wang, M. Li, K. Wang, R. Shen and S. Hu, *IEEE/ASME Trans. Mechatron.*, 2013, **19**, 312–320.
356 H. Ko, Z. Zhang, Y. L. Chueh, J. C. Ho, J. Lee, R. S. Fearing and A. Javey, *Adv. Funct. Mater.*, 2009, **19**, 3098–3102.
357 H. Fan, J. Wang, Z. Tao, J. Huang, P. Rao, T. Kurokawa and J. P. Gong, *Nat. Commun.*, 2019, **10**, 5127.
358 H. Fan, J. Wang and J. P. Gong, *Adv. Funct. Mater.*, 2021, **31**, 2009334.
359 G. Ju, M. Cheng, F. Guo, Q. Zhang and F. Shi, *Angew. Chem., Int. Ed.*, 2018, **57**, 8963–8967.
360 K. Chen, Q. Lin, L. Wang, Z. Zhuang, Y. Zhang, D. Huang and H. Wang, *ACS Appl. Mater. Interfaces*, 2021, **13**, 9748–9761.
361 F. J. Cedano-Serrano, U. Sidoli, A. Synytska, Y. Tran, D. Hourdet and C. Creton, *Macromolecules*, 2019, **52**, 3852–3862.
362 H. Qiao, P. Qi, X. Zhang, L. Wang, Y. Tan, Z. Luan, Y. Xia, Y. Li and K. Sui, *ACS Appl. Mater. Interfaces*, 2019, **11**, 7755–7763.
363 X. Su, Y. Luo, Z. Tian, Z. Yuan, Y. Han, R. Dong, L. Xu, Y. Feng, X. Liu and J. Huang, *Mater. Horiz.*, 2020, **7**, 2651–2661.
364 A. Nishiguchi, Y. Kurihara and T. Taguchi, *Acta Biomater.*, 2019, **99**, 387–396.
365 L. Xu, S. Gao, Q. Guo, C. Wang, Y. Qiao and D. Qiu, *Adv. Mater.*, 2020, **32**, 2004579.
366 J. Chen, D. Wang, L. H. Wang, W. Liu, A. Chiu, K. Shariati, Q. Liu, X. Wang, Z. Zhong and J. Webb, *Adv. Mater.*, 2020, **32**, 2001628.
367 C. Cui, T. Wu, X. Chen, Y. Liu, Y. Li, Z. Xu, C. Fan and W. Liu, *Adv. Funct. Mater.*, 2020, **30**, 2005689.
368 X. Liu, Q. Zhang, L. Duan and G. Gao, *Adv. Funct. Mater.*, 2019, **29**, 1900450.
369 X. Liu, Q. Zhang and G. Gao, *Chem. Eng. J.*, 2020, **394**, 124898.
370 Y. Bu, L. Zhang, G. Sun, F. Sun, J. Liu, F. Yang, P. Tang and D. Wu, *Adv. Mater.*, 2019, **31**, 1901580.
371 H. Yuk, C. E. Varela, C. S. Nabzdyk, X. Mao, R. F. Padera, E. T. Roche and X. Zhao, *Nature*, 2019, **575**, 169–174.
372 J. Liu and O. A. Scherman, *Adv. Funct. Mater.*, 2018, **28**, 1800848.
373 X. Fan, W. Zhou, Y. Chen, L. Yan, Y. Fang and H. Liu, *ACS Appl. Mater. Interfaces*, 2020, **12**, 32031–32040.
374 X. Fan, Y. Fang, W. Zhou, L. Yan, Y. Xu, H. Zhu and H. Liu, *Mater. Horiz.*, 2021, **8**, 997–1007.
375 Y. Xu, P. A. Patsis, S. Hauser, D. Voigt, R. Rothe, M. Günther, M. Cui, X. Yang, R. Wieduwild and K. Eckert, *Adv. Sci.*, 2019, **6**, 1802077.
376 H. S. Nanda, A. H. Shah, G. Wicaksono, O. Pokholenko, F. Gao, I. Djordjevic and T. W. Steele, *Biomacromolecules*, 2018, **19**, 1425–1434.
377 Q. Li, P. Zhang, C. Yang, H. Duan and W. Hong, *Extreme Mech. Lett.*, 2021, **43**, 101193.

378 Z. Yu and P. Wu, *Adv. Mater.*, 2021, **33**, 2008479.
379 J. N. Lee, S. Y. Lee and W. H. Park, *ACS Appl. Mater. Interfaces*, 2021, **13**, 18324–18337.
380 J. Luo, Y. Xing, C. Sun, L. Fan, H. Shi, Q. Zhang, Y. Li, C. Hou and H. Wang, *Chem. Eng. J.*, 2022, **427**, 130886.
381 S. H. Kim, Y. J. Lee, J. R. Chao, D. Y. Kim, M. T. Sultan, H. J. Lee, J. M. Lee, J. S. Lee, O. J. Lee and H. Hong, *NPG Asia Mater.*, 2020, **12**, 46.
382 B. Li, J. J. Whalen, M. S. Humayun and M. E. Thompson, *Adv. Funct. Mater.*, 2020, **30**, 1907478.
383 M. M. Hasani-Sadrabadi, P. Sarrion, S. Pouraghaei, Y. Chau, S. Ansari, S. Li, T. Aghaloo and A. Moshaverinia, *Sci. Transl. Med.*, 2020, **12**, eaay6853.
384 X. Zhang, J. Chen, J. He, Y. Bai and H. Zeng, *J. Colloid Interface Sci.*, 2021, **585**, 420–432.
385 C. Wang, X. Gao, F. Zhang, W. Hu, Z. Gao, Y. Zhang, M. Ding and Q. Liang, *Small*, 2022, **18**, 2200336.
386 Y. Hou, Y. Li, Y. Li, D. Li, T. Guo, X. Deng, H. Zhang, C. Xie and X. Lu, *ACS Nano*, 2023, **17**, 2745–2760.
387 Y. Yang, Y. Ma, J. Wang, L. You, R. Zhang, Q. Meng, S. Zhong, W. He and X. Cui, *Carbohydr. Polym.*, 2023, **316**, 121083.
388 L. Wang, Z. Zhao, J. Dong, D. Li, W. Dong, H. Li, Y. Zhou, Q. Liu and B. Deng, *ACS Appl. Mater. Interfaces*, 2023, **15**, 16515–16525.
389 I. Apsite, S. Salehi and L. Ionov, *Chem. Rev.*, 2021, **122**, 1349–1415.
390 J. Zhang, B. He, Y. Hu, P. Alam, H. Zhang, J. W. Lam and B. Z. Tang, *Adv. Mater.*, 2021, **33**, 2008071.
391 L. Tang, L. Wang, X. Yang, Y. Feng, Y. Li and W. Feng, *Prog. Mater. Sci.*, 2021, **115**, 100702.
392 E. Kizilkan, J. Strueben, A. Staubitz and S. N. Gorb, *Sci. Rob.*, 2017, **2**, eaak9454.
393 S. Li, H. Tian, J. Shao, H. Liu, D. Wang and W. Zhang, *ACS Appl. Mater. Interfaces*, 2020, **12**, 39745–39755.
394 Q. Li, L. Li, K. Shi, B. Yang, X. Wang, Z. Shi, D. Tan, F. Meng, Q. Liu and S. Hu, *Adv. Sci.*, 2020, **7**, 2001650.
395 Z. Shi, D. Tan, Z. Wang, K. Xiao, B. Zhu, F. Meng, Q. Liu, X. Wang and L. Xue, *ACS Appl. Mater. Interfaces*, 2022, **14**, 31448–31454.
396 C. Li, J. Yang, W. He, M. Xiong, X. Niu, X. Li and D. G. Yu, *Adv. Mater. Interfaces*, 2023, **10**, 2202160.
397 H. Wang, Z. Zhang, Z. Wang, Y. Liang, Z. Cui, J. Zhao, X. Li and L. Ren, *ACS Appl. Mater. Interfaces*, 2019, **11**, 28478–28486.
398 A. Grigoryev, I. Tokarev, K. G. Kornev, I. Luzinov and S. Minko, *J. Am. Chem. Soc.*, 2012, **134**, 12916–12919.
399 Z. Yang, J. K. Park and S. Kim, *Small*, 2018, **14**, 1702839.
400 X. Bai, Q. Yang, H. Li, J. Huo, J. Liang, X. Hou and F. Chen, *Langmuir*, 2022, **38**, 4645–4656.
401 J. K. Park, Z. Yang and S. Kim, *ACS Appl. Mater. Interfaces*, 2017, **9**, 33333–33340.
402 Y. Pan, W. Kong, B. Bhushan and X. Zhao, *Beilstein J. Nanotechnol.*, 2019, **10**, 866–873.
403 H. Kang, Y. Liu, H. Lai, X. Yu, Z. Cheng and L. Jiang, *ACS Nano*, 2018, **12**, 1074–1082.
404 P. Vialar, P. Merzeau, E. Barthel, S. Giasson and C. Drummond, *Langmuir*, 2019, **35**, 15723–15728.
405 P. Vialar, P. Merzeau, S. Giasson and C. Drummond, *Langmuir*, 2019, **35**, 15605–15613.
406 O. Guselnikova, R. Elashnikov, P. Postnikov, V. Svorcik and O. Lyutakov, *ACS Appl. Mater. Interfaces*, 2018, **10**, 37461–37469.
407 L. Bauman, Q. Wen, D. Sameoto, C. H. Yap and B. Zhao, *Colloids Surf., A*, 2021, **610**, 125901.
408 P. Guo, Z. Wang, L. Heng, Y. Zhang, X. Wang and L. Jiang, *Adv. Funct. Mater.*, 2019, **29**, 1808717.
409 X. Liu, H. Gu, H. Ding, X. Du, M. Wei, Q. Chen and Z. Gu, *Adv. Sci.*, 2020, **7**, 2000878.
410 M. Coux, C. Clanet and D. Quéré, *Appl. Phys. Lett.*, 2017, **110**, 251605.
411 Z. Lao, D. Pan, H. Yuan, J. Ni, S. Ji, W. Zhu, Y. Hu, J. Li, D. Wu and J. Chu, *ACS Nano*, 2018, **12**, 10142–10150.
412 H. Wang, Z. Zhang, J. Zheng, J. Zhao, Y. Liang, X. Li and L. Ren, *Chem. Eng. J.*, 2021, **417**, 127944.
413 T. Lv, Z. Cheng, D. Zhang, E. Zhang, Q. Zhao, Y. Liu and L. Jiang, *ACS Nano*, 2016, **10**, 9379–9386.
414 Y. Lin, Z. Hu, C. Gao, Z. Guo, C. Li and Y. Zheng, *Adv. Mater. Interfaces*, 2018, **5**, 1800962.
415 L. Ma, J. Wang, J. He, Y. Yao, X. Zhu, L. Peng, J. Yang, X. Liu and M. Qu, *ACS Appl. Mater. Interfaces*, 2021, **13**, 31285–31297.
416 R. Qu, Y. Liu, W. Zhang, X. Li, L. Feng and L. Jiang, *Chem. Sci.*, 2019, **10**, 4089–4096.
417 W. Jo, J. Choi, H. S. Kang, M. Kim, S. Baik, B. J. Lee, C. Pang and H.-T. Kim, *ACS Appl. Mater. Interfaces*, 2019, **12**, 5058–5064.
418 Y. Shao, H. Dou, P. Tao, R. Jiang, Y. Fan, Y. Jiang, J. Zhao, Z. Zhang, T. Yue and S. N. Gorb, *ACS Appl. Mater. Interfaces*, 2022, **14**, 17995–18003.
419 Y. Shao, W. Du, Y. Fan, J. Zhao, Z. Zhang and L. Ren, *Chem. Eng. J.*, 2022, **427**, 131718.
420 S. Chen, M. Zhu, Y. Zhang, S. Dong and X. Wang, *Langmuir*, 2021, **37**, 2312–2321.
421 S. Jiang, Y. Hu, H. Wu, Y. Zhang, Y. Zhang, Y. Wang, Y. Zhang, W. Zhu, J. Li and D. Wu, *Adv. Mater.*, 2019, **31**, 1807507.
422 Y. Lin, Z. Hu, M. Zhang, T. Xu, S. Feng, L. Jiang and Y. Zheng, *Adv. Funct. Mater.*, 2018, **28**, 1800163.
423 S. Ben, T. Zhou, H. Ma, J. Yao, Y. Ning, D. Tian, K. Liu and L. Jiang, *Adv. Sci.*, 2019, **6**, 1900834.
424 M. Liu, C. Li, Z. Peng, Y. Yao and S. Chen, *Chem. Eng. J.*, 2022, **430**, 132749.
425 J. Yong, F. Chen, Q. Yang, U. Farooq and X. Hou, *J. Mater. Chem. A*, 2015, **3**, 10703–10709.
426 X. Lou, Y. Huang, X. Yang, H. Zhu, L. Heng and F. Xia, *Adv. Funct. Mater.*, 2020, **30**, 1901130.
427 A. Shome, A. Das, A. Borbora, M. Dhar and U. Manna, *Chem. Soc. Rev.*, 2022, **51**, 5452–5497.
428 D. Tian, N. Zhang, X. Zheng, G. Hou, Y. Tian, Y. Du, L. Jiang and S. X. Dou, *ACS Nano*, 2016, **10**, 6220–6226.
429 W. Wang, J. V. Timonen, A. Carlson, D.-M. Drotlef, C. T. Zhang, S. Kolle, A. Grinthal, T.-S. Wong, B. Hatton and S. H. Kang, *Nature*, 2018, **559**, 77–82.

430 B. L. Wang, L. Heng and L. Jiang, *ACS Appl. Mater. Interfaces*, 2018, **10**, 7442–7450.
431 X. Yao, Y. Hu, A. Grinthal, T.-S. Wong, L. Mahadevan and J. Aizenberg, *Nat. Mater.*, 2013, **12**, 529–534.
432 Y. Huang, B. B. Stogin, N. Sun, J. Wang, S. Yang and T. S. Wong, *Adv. Mater.*, 2017, **29**, 1604641.
433 H. Verheijen and M. Prins, *Langmuir*, 1999, **15**, 6616–6620.
434 T. Guo, P. Che, L. Heng, L. Fan and L. Jiang, *Adv. Mater.*, 2016, **28**, 6999–7007.
435 P. Che, L. Heng and L. Jiang, *Adv. Funct. Mater.*, 2017, **27**, 1606199.
436 Z. Wang, L. Heng and L. Jiang, *J. Mater. Chem. A*, 2018, **6**, 3414–3421.
437 J. Wang, Y. Huang, K. You, X. Yang, Y. Song, H. Zhu, F. Xia and L. Jiang, *ACS Appl. Mater. Interfaces*, 2019, **11**, 7591–7599.
438 X. Yao, J. Ju, S. Yang, J. Wang and L. Jiang, *Adv. Mater.*, 2014, **26**, 1895–1900.
439 K. Manabe, T. Matsubayashi, M. Tenjimbayashi, T. Moriya, Y. Tsuge, K.-H. Kyung and S. Shiratori, *ACS Nano*, 2016, **10**, 9387–9396.
440 G. H. Zhu, C. Zhang, C. Wang and N. S. Zacharia, *Adv. Mater. Interfaces*, 2016, **3**, 1600515.
441 Z. Wang, Q. Xu, L. Wang, L. Heng and L. Jiang, *J. Mater. Chem. A*, 2019, **7**, 18510–18518.
442 C. Liu, H. Ding, Z. Wu, B. Gao, F. Fu, L. Shang, Z. Gu and Y. Zhao, *Adv. Funct. Mater.*, 2016, **26**, 7937–7942.
443 P. Zhang, H. Liu, J. Meng, G. Yang, X. Liu, S. Wang and L. Jiang, *Adv. Mater.*, 2014, **26**, 3131–3135.
444 Y. Wang, B. Qian, C. Lai, X. Wang, K. Ma, Y. Guo, X. Zhu, B. Fei and J. H. Xin, *ACS Appl. Mater. Interfaces*, 2017, **9**, 24428–24432.
445 D. Li, J. Huang, G. Han and Z. Guo, *J. Mater. Chem. A*, 2018, **6**, 22741–22748.
446 M. Cao, X. Jin, Y. Peng, C. Yu, K. Li, K. Liu and L. Jiang, *Adv. Mater.*, 2017, **29**, 1606869.
447 I. Oh, C. Keplinger, J. Cui, J. Chen, G. M. Whitesides, J. Aizenberg and Y. Hu, *Adv. Funct. Mater.*, 2018, **28**, 1802632.
448 J. Wang, L. Sun, M. Zou, W. Gao, C. Liu, L. Shang, Z. Gu and Y. Zhao, *Sci. Adv.*, 2017, **3**, e1700004.
449 Z. Wang, Y. Liu, P. Guo, L. Heng and L. Jiang, *Adv. Funct. Mater.*, 2018, **28**, 1801310.
450 K. Han, L. Heng, Y. Zhang, Y. Liu and L. Jiang, *Adv. Sci.*, 2019, **6**, 1801231.
451 P. Irajizad, S. Ray, N. Farokhnia, M. Hasnain, S. Baldelli and H. Ghasemi, *Adv. Mater. Interfaces*, 2017, **4**, 1700009.
452 F. Wang, M. Liu, C. Liu, Q. Zhao, T. Wang, Z. Wang and X. Du, *Sci. Adv.*, 2022, **8**, eabp9369.
453 Z.-Z. Jiao, H. Zhou, X.-C. Han, D.-D. Han and Y.-L. Zhang, *J. Colloid Interface Sci.*, 2023, **629**, 582–592.
454 Q. Rao, J. Zhang, X. Zhan, F. Chen and Q. Zhang, *J. Mater. Chem. A*, 2020, **8**, 2481–2489.
455 K. Shao, S. Jiang, Y. Hu, Y. Zhang, C. Li, Y. Zhang, J. Li, D. Wu and J. Chu, *Adv. Funct. Mater.*, 2022, **32**, 2205831.
456 R. Wang, F. Jin, Y. Li, J. Gong, H. Lai, Y. Liu and Z. Cheng, *Adv. Funct. Mater.*, 2023, **33**, 2305766.
457 C. Wei, O. Gendelman and Y. Jiang, *Langmuir*, 2024, **40**(5), 2764–2772.
458 K. Han, Z. Wang, X. Han, X. Wang, P. Guo, P. Che, L. Heng and L. Jiang, *Adv. Funct. Mater.*, 2022, **32**, 2207738.
459 A. B. Croll, N. Hosseini and M. D. Bartlett, *Adv. Mater. Technol.*, 2019, **4**, 1900193.
460 J. Zhao, X. Li, Y. Tan, X. Liu, T. Lu and M. Shi, *Adv. Mater.*, 2022, **34**, 2107748.
461 Y. Ahn, Y. Jang, N. Selvapalam, G. Yun and K. Kim, *Angew. Chem., Int. Ed.*, 2013, **52**, 3140–3144.
462 D.-M. Drotlef, P. Blümler and A. Del Campo, *Adv. Mater.*, 2014, **26**, 775–779.
463 J. Krahn, E. Bovero and C. Menon, *ACS Appl. Mater. Interfaces*, 2015, **7**, 2214–2222.
464 H. Tian, H. Liu, J. Shao, S. Li, X. Li and X. Chen, *Soft Matter*, 2020, **16**, 5599–5608.
465 X. Wang, D. Tan, S. Hu, Q. Li, B. Yang, Z. Shi, R. Das, X. Xu, Z.-S. Wu and L. Xue, *ACS Appl. Mater. Interfaces*, 2019, **11**, 46337–46343.
466 Y. Mi, Y. Niu, H. Ni, Y. Zhang, L. Wang, Y. Liu, M. A. Ramos, T. S. Hu and Q. Xu, *Chem. Eng. J.*, 2022, **431**, 134081.
467 A. Eklund, O. Ikkala and H. Zhang, *Adv. Funct. Mater.*, 2023, 2214091.
468 H. Xu, S. Zhao, A. Yuan, Y. Zhao, X. Wu, Z. Wei, J. Lei and L. Jiang, *Small*, 2023, **19**, 2300626.
469 Y. Zheng, M. Wu, M. Duan, S. Chen, X. Wang and D. Zhou, *Chem. Eng. J.*, 2024, 150459.
470 J. D. Eisenhaure, T. Xie, S. Varghese and S. Kim, *ACS Appl. Mater. Interfaces*, 2013, **5**, 7714–7717.
471 H. Shahsavan, S. M. Salili, A. Jákli and B. Zhao, *Adv. Mater.*, 2017, **29**, 1604021.
472 Y. Jin, Z. Lei, P. Taynton, S. Huang and W. Zhang, *Matter*, 2019, **1**, 1456–1493.
473 H. H. Moon, I. Cha, H. A. Hegazy, K. S. Kim and C. Song, *Bull. Korean Chem. Soc.*, 2023, **44**, 750–767.
474 P. Chakma and D. Konkolewicz, *Angew. Chem., Int. Ed.*, 2019, **58**, 9682–9695.
475 X.-L. Zhao, P.-X. Tian, Y.-D. Li and J.-B. Zeng, *Green Chem.*, 2022, **24**, 4363–4387.
476 C. Hao, T. Liu, S. Zhang, L. Brown, R. Li, J. Xin, T. Zhong, L. Jiang and J. Zhang, *ChemSusChem*, 2019, **12**, 1049–1058.
477 M. A. Rahman, C. Bowland, S. Ge, S. R. Acharya, S. Kim, V. R. Cooper, X. C. Chen, S. Irle, A. P. Sokolov and A. Savara, *Sci. Adv.*, 2021, **7**, eabk2451.
478 Y. Oh, J. Park, J.-J. Park, S. Jeong and H. Kim, *Chem. Mater.*, 2020, **32**, 6384–6391.
479 W. Denissen, J. M. Winne and F. E. Du Prez, *Chem. Sci.*, 2016, **7**, 30–38.
480 H. Xiang, J. Yin, G. Lin, X. Liu, M. Rong and M. Zhang, *Chem. Eng. J.*, 2019, **358**, 878–890.
481 A. Trejo-Machin, L. Puchot and P. Verge, *Polym. Chem.*, 2020, **11**, 7026–7034.
482 K. Cheng, A. Chortos, J. A. Lewis and D. R. Clarke, *ACS Appl. Mater. Interfaces*, 2022, **14**, 4552–4561.
483 M. Wu, Y. Liu, P. Du, X. Wang and B. Yang, *Int. J. Adhes. Adhes.*, 2020, **100**, 102597.
484 S. Wang, Z. Liu, L. Zhang, Y. Guo, J. Song, J. Lou, Q. Guan, C. He and Z. You, *Mater. Chem. Front.*, 2019, **3**, 1833–1839.

485 H. Dai, Z. Dong and L. Jiang, *Sci. Adv.*, 2020, **6**, eabb5528.
486 S. Kim, M. Spenko, S. Trujillo, B. Heyneman, V. Mattoli and M. R. Cutkosky, *Proc. 2007 IEEE Int. Conf. on Robotics and Automation*, IEEE, Rome, Italy, 2007, pp. 1268–1273.
487 S. Song, D. M. Drotlef, D. Son, A. Koivikko and M. Sitti, *Adv. Sci.*, 2021, **8**, 2100641.
488 D. M. Drotlef, M. Amjadi, M. Yunusa and M. Sitti, *Adv. Mater.*, 2017, **29**, 1701353.
489 M. Zhu, Y. Wang, M. Lou, J. Yu, Z. Li and B. Ding, *Nano Energy*, 2021, **81**, 105669.
490 Y. Huang, B. B. Stogin, N. Sun, J. Wang, S. Yang and T.-S. Wong, *Adv. Mater.*, 2017, **29**, 1604641.
491 W. Chen, J. Wainer, S. W. Ryoo, X. Qi, R. Chang, J. Li, S. H. Lee, S. Min, A. Wentworth and J. E. Collins, *Sci. Adv.*, 2022, **8**, eabk1792.
492 Y. Wang, L. Shang, G. Chen, L. Sun, X. Zhang and Y. Zhao, *Sci. Adv.*, 2020, **6**, eaax8258.
493 J. Li, Y. Hou, Y. Liu, C. Hao, M. Li, M. K. Chaudhury, S. Yao and Z. Wang, *Nat. Phys.*, 2016, **12**, 606–612.
494 Y. Yu, F. Fu, L. Shang, Y. Cheng, Z. Gu and Y. Zhao, *Adv. Mater.*, 2017, **29**, 1605765.
495 H. Bai, X. Tian, Y. Zheng, J. Ju, Y. Zhao and L. Jiang, *Adv. Mater.*, 2010, **48**, 5521–5525.
496 X. Yan, Y. Qin, F. Chen, G. Zhao, S. Sett, M. J. Hoque, K. F. Rabbi, X. Zhang, Z. Wang and L. Li, *ACS Nano*, 2020, **14**, 12796–12809.
497 J. Diez, R. Gratton, L. Thomas and B. Marino, *Phys. Fluids*, 1994, **6**, 24–33.
498 Y. Zuo, L. Zheng, C. Zhao and H. Liu, *Small*, 2020, **16**, 1903849.
499 Y. Wang, K. Ma and J. H. Xin, *Adv. Funct. Mater.*, 2018, **28**, 1705128.
500 H. Ren, H. Jin, J. Shu, J. Xie, E. Wang, D.-A. Ge, S.-Y. Tang, X. Li, W. Li and S. Zhang, *Mater. Horiz.*, 2021, **8**, 3063–3071.
501 K. Yin, L. Wang, Q. Deng, Q. Huang, J. Jiang, G. Li and J. He, *Nano-Micro Lett.*, 2022, **14**, 97.
502 J. Wang, W. Gao, H. Zhang, M. Zou, Y. Chen and Y. Zhao, *Sci. Adv.*, 2018, **4**, eaat7392.
503 Y. Cho, T. S. Shim and S. Yang, *Adv. Mater.*, 2015, **28**, 1433–1439.
504 H. Yue, Q. Zeng, J. Huang, Z. Guo and W. Liu, *Adv. Colloid Interface Sci.*, 2022, **300**, 102583.
505 Y. Zhang, N. Meng, A. A. Babar, X. Wang, J. Yu and B. Ding, *Nano Lett.*, 2021, **21**, 7806–7814.
506 Y. Zheng, H. Bai, Z. Huang, X. Tian, F.-Q. Nie, Y. Zhao, J. Zhai and L. Jiang, *Nature*, 2010, **463**, 640–643.
507 A. R. Parker and C. R. Lawrence, *Nature*, 2001, **414**, 33–34.
508 K. Li, J. Ju, Z. Xue, J. Ma, L. Feng, S. Gao and L. Jiang, *Nat. Commun.*, 2013, **4**, 2276.
509 M. He, P. Wang, B. Xu, L. Jiang and H. Liu, *Adv. Funct. Mater.*, 2018, **28**, 1800187.
510 X. Dai, N. Sun, S. Nielsen, B. Stogin, J. Wang, S. Yang and T. Wong, *Sci. Adv.*, 2018, **4**(3), eaaq0919.
511 K.-C. Park, P. Kim, A. Grinthal, N. He, D. Fox, J. C. Weaver and J. Aizenberg, *Nature*, 2016, **531**, 78–82.
512 Z. Zhang, C. Qin, H. Feng, Y. Xiang, B. Yu, X. Pei, Y. Ma and F. Zhou, *Nat. Commun.*, 2022, **13**, 6964.
513 M. P. Murphy, C. Kute, Y. Mengüç and M. Sitti, *Int. J. Robot. Res.*, 2011, **30**, 118–133.
514 J. Krahn, Y. Liu, A. Sadeghi and C. Menon, *Smart Mater. Struct.*, 2011, **20**, 115021.
515 S. Kim, M. Spenko, S. Trujillo, B. Heyneman, D. Santos and M. R. Cutkosky, *IEEE Trans. Rob.*, 2008, **24**, 65–74.
516 X. Li, P. Bai, X. Li, L. Li, Y. Li, H. Lu, L. Ma, Y. Meng and Y. Tian, *Friction*, 2022, **10**, 1192–1207.
517 Y. Tang, Q. Zhang, G. Lin and J. Yin, *Soft Robot.*, 2018, **5**, 592–600.
518 M. Henrey, A. Ahmed, P. Boscariol, L. Shannon and C. Menon, *J. Bionic Eng.*, 2014, **11**, 1–17.
519 Y. Li, A. Ahmed, D. Sameoto and C. Menon, *Robotica*, 2012, **30**, 79–89.
520 E. W. Hawkes, J. Ulmen, N. Esparza and M. R. Cutkosky, Scaling walls: Applying dry adhesives to the real world, in *2011 IEEE/RSJ International Conference on Intelligent Robots and Systems*, IEEE, 2011, pp. 5100–5106.
521 H. Ko, H. Yi and H. E. Jeong, *Int. J. Precis. Eng. Manuf. Green Technol.*, 2017, **4**, 273–280.
522 Y. Zhang, D. Yang, P. Yan, P. Zhou, J. Zou and G. Gu, *IEEE Trans. Rob.*, 2021, **38**, 1806–1819.
523 P. Van Nguyen, *IEEE Rob. Autom. Lett.*, 2021, **6**, 4273–4280.
524 Z. Xie, A. G. Domel, N. An, C. Green, Z. Gong, T. Wang, E. M. Knubben, J. C. Weaver, K. Bertoldi and L. Wen, *Soft Robot.*, 2020, **7**, 639–648.
525 B. Mazzolai, A. Mondini, F. Tramacere, G. Riccomi, A. Sadeghi, G. Giordano, E. Del Dottore, M. Scaccia, M. Zampato and S. Carminati, *Adv. Intell. Syst.*, 2019, **1**, 1900041.
526 H. Hu, D. Wang, H. Tian, Q. Huang, C. Wang, X. Chen, Y. Gao, X. Li, X. Chen and Z. Zheng, *Adv. Funct. Mater.*, 2022, **32**, 2109076.
527 X. Wang, X. Sun, D. Gan, M. Soubrier, H.-Y. Chiang, L. Yan, Y. Li, J. Li, S. Yu and Y. Xia, *Matter*, 2022, **5**, 1204–1223.
528 Z. Wu, H. Wang, Q. Ding, K. Tao, W. Shi, C. Liu, J. Chen and J. Wu, *Adv. Funct. Mater.*, 2023, **33**, 2300046.
529 K. Zhai, H. Wang, Q. Ding, Z. Wu, M. Ding, K. Tao, B. R. Yang, X. Xie, C. Li and J. Wu, *Adv. Sci.*, 2023, **10**, 2205632.
530 S. Baik, J. Lee, E. J. Jeon, B.-Y. Park, D. W. Kim, J. H. Song, H. J. Lee, S. Y. Han, S.-W. Cho and C. Pang, *Sci. Adv.*, 2021, **7**, eabf5695.
531 J. Moon, G. Yi, C. Oh, M. Lee, Y. Lee and M. Kim, *Physiol. Meas.*, 2002, **23**, 247.
532 W. G. Bae, D. Kim, M. K. Kwak, L. Ha, S. M. Kang and K. Y. Suh, *Adv. Healthcare Mater.*, 2013, **2**, 109–113.
533 J. Kang, J. B.-H. Tok and Z. Bao, *Nat. Electron.*, 2019, **2**, 144–150.
534 S. Zhang, Y. Chen, H. Liu, Z. Wang, H. Ling, C. Wang, J. Ni, B. Çelebi-Saltik, X. Wang and X. Meng, *Adv. Mater.*, 2020, **32**, 1904752.
535 X. Le, W. Lu, J. Zhang and T. Chen, *Adv. Sci.*, 2019, **6**, 1801584.
536 Z. Lei and P. Wu, *Nat. Commun.*, 2019, **10**, 1–9.
537 B. Lu, H. Yuk, S. Lin, N. Jian, K. Qu, J. Xu and X. Zhao, *Nat. Commun.*, 2019, **10**, 1–10.

538 Y. Wang, C. Zhu, R. Pfattner, H. Yan, L. Jin, S. Chen, F. Molina-Lopez, F. Lissel, J. Liu and N. I. Rabiah, *Sci. Adv.*, 2017, **3**, e1602076.
539 Y. Liu, A. F. McGuire, H.-Y. Lou, T. L. Li, J. B.-H. Tok, B. Cui and Z. Bao, *Proc. Natl. Acad. Sci. U. S. A.*, 2018, **115**, 11718–11723.
540 Y. Hou and X. Hou, *Science*, 2021, **373**, 628–629.
541 L. Han, K. Liu, M. Wang, K. Wang, L. Fang, H. Chen, J. Zhou and X. Lu, *Adv. Funct. Mater.*, 2018, **28**, 1704195.
542 Z. Wu, H. Wang, Q. Ding, K. Tao, W. Shi, C. Liu, J. Chen and J. Wu, *Adv. Funct. Mater.*, 2023, 2300046.
543 K. Zhai, H. Wang, Q. Ding, Z. Wu, M. Ding, K. Tao, B. R. Yang, X. Xie, C. Li and J. Wu, *Adv. Sci.*, 2022, 2205632.
544 L. Shi, T. Zhu, G. Gao, X. Zhang, W. Wei, W. Liu and S. Ding, *Nat. Commun.*, 2018, **9**, 1–7.
545 C. Keplinger, J.-Y. Sun, C. C. Foo, P. Rothemund, G. M. Whitesides and Z. Suo, *Science*, 2013, **341**, 984–987.
546 H. R. Lee, C. C. Kim and J. Y. Sun, *Adv. Mater.*, 2018, **30**, 1704403.
547 W. Zhang, B. Wu, S. Sun and P. Wu, *Nat. Commun.*, 2021, **12**, 1–12.
548 Y. Cai, J. Shen, C.-W. Yang, Y. Wan, H.-L. Tang, A. A. Aljarb, C. Chen, J.-H. Fu, X. Wei and K.-W. Huang, *Sci. Adv.*, 2020, **6**, eabb5367.
549 Q. Ding, H. Wang, Z. Zhou, Z. Wu, K. Tao, X. Gui, C. Liu, W. Shi and J. Wu, *SmartMat*, 2023, **4**, e1147.
550 Q. Ding, Z. Zhou, H. Wang, Z. Wu, K. Tao, B. R. Yang, X. Xie, J. Fu and J. Wu, *SmartMat*, 2023, **4**, e1141.
551 F. Rol, M. N. Belgacem, A. Gandini and J. Bras, *Prog. Polym. Sci.*, 2019, **88**, 241–264.
552 A. Zhang, K. Jung, A. Li, J. Liu and C. Boyer, *Prog. Polym. Sci.*, 2019, **99**, 101164.
553 G. Bovone, O. Y. Dudaryeva, B. Marco-Dufort and M. W. Tibbitt, *ACS Biomater. Sci. Eng.*, 2021, **7**, 4048–4076.
554 M. Su, L. Ruan, X. Dong, S. Tian, W. Lang, M. Wu, Y. Chen, Q. Lv and L. Lei, *Int. J. Biol. Macromol.*, 2023, **227**, 472–492.
555 G. C. Gurtner, S. Werner, Y. Barrandon and M. T. Longaker, *Nature*, 2008, **453**, 314–321.
556 N. Annabi, A. Tamayol, S. R. Shin, A. M. Ghaemmaghami, N. A. Peppas and A. Khademhosseini, *Nano Today*, 2014, **9**, 574–589.
557 R. Januchowski and O. W. Jordan Ferguson III, *Osteopath. Fam. Physician*, 2014, **6**, 25–29.
558 A. Duarte, J. Coelho, J. Bordado, M. Cidade and M. Gil, *Prog. Polym. Sci.*, 2012, **37**, 1031–1050.
559 J. C. Dumville, P. Coulthard, H. V. Worthington, P. Riley, N. Patel, J. Darcey, M. Esposito, M. van der Elst and O. J. van Waes, *Cochrane Database of Syst. Rev.*, 2014, **2014**, CD004287.
560 V. Muthukumar, S. Venugopal and S. Subramaniam, *Int. Surgery J.*, 2017, **4**, 1235–1243.
561 Y. Liang, J. He and B. Guo, *ACS Nano*, 2021, **15**, 12687–12722.
562 M. Kharaziha, A. Baidya and N. Annabi, *Adv. Mater.*, 2021, **33**, 2100176.
563 T. Deng, D. Gao, X. Song, Z. Zhou, L. Zhou, M. Tao, Z. Jiang, L. Yang, L. Luo and A. Zhou, *Nat. Commun.*, 2023, **14**, 396.
564 Z. Zhu, J. Wang, X. Pei, J. Chen, X. Wei, Y. Liu, P. Xia, Q. Wan, Z. Gu and Y. He, *Sci. Adv.*, 2023, **9**, eadh2213.
565 J. Shin, J. S. Lee, C. Lee, H. J. Park, K. Yang, Y. Jin, J. H. Ryu, K. S. Hong, S. H. Moon and H. M. Chung, *Adv. Funct. Mater.*, 2015, **25**, 3814–3824.
566 Y. Liang, X. Zhao, T. Hu, B. Chen, Z. Yin, P. X. Ma and B. Guo, *Small*, 2019, **15**, 1900046.
567 M. Li, Y. Liang, J. He, H. Zhang and B. Guo, *Chem. Mater.*, 2020, **32**, 9937–9953.
568 J. H. Ryu, H. J. Kim, K. Kim, G. Yoon, Y. Wang, G. S. Choi, H. Lee and J. S. Park, *Adv. Funct. Mater.*, 2019, **29**, 1900495.
569 Q. Chen, Z. Xiao, C. Wang, G. Chen, Y. Zhang, X. Zhang, X. Han, J. Wang, X. Ye and M. R. Prausnitz, *ACS Nano*, 2022, **16**, 18223–18231.
570 C. Gao, L. Wang, Y. Lin, J. Li, Y. Liu, X. Li, S. Feng and Y. Zheng, *Adv. Funct. Mater.*, 2018, **28**, 1803072.
571 B. Aksak, M. P. Murphy and M. Sitti, Gecko inspired micro-fibrillar adhesives for wall climbing robots on micro/nanoscale rough surfaces, in *2008 IEEE international conference on robotics and automation*, IEEE, 2008, pp. 3058–3063.
572 M. P. Murphy and M. Sitti, *IEEE/ASME Trans. Mech.*, 2007, **12**, 330–338.
573 D. Santos, B. Heyneman, S. Kim, N. Esparza and M. R. Cutkosky, Gecko-inspired climbing behaviors on vertical and overhanging surfaces, in *2008 IEEE International Conference on Robotics and Automation*, IEEE, 2008, pp. 1125–1131.
574 M. Zhou, Y. Tian, D. Sameoto, X. Zhang, Y. Meng and S. Wen, *ACS Appl. Mater. Interfaces*, 2013, **5**, 10137–10144.
575 P. Glick, S. A. Suresh, D. Ruffatto, M. Cutkosky, M. T. Tolley and A. Parness, *IEEE Rob. Autom. Lett.*, 2018, **3**, 903–910.
576 Z. Xie, F. Yuan, Z. Liu, Z. Sun, E. M. Knubben and L. Wen, *IEEE/ASME Trans. Mech.*, 2020, **25**, 1841–1850.
577 A. Shit, S. B. Heo, I. In and S. Y. Park, *ACS Appl. Mater. Interfaces*, 2020, **12**, 34105–34114.
578 B. Xue, H. Sheng, Y. Li, L. Li, W. Di, Z. Xu, L. Ma, X. Wang, H. Jiang and M. Qin, *Natl. Sci. Rev.*, 2022, **9**, nwab147.
579 L. Xie, J. Wang, Q. Lu, W. Hu, D. Yang, C. Qiao, X. Peng, Q. Peng, T. Wang and W. Sun, *Adv. Colloid Interface Sci.*, 2021, **295**, 102491.
580 L. Xiang, J. Zhang, L. Gong and H. Zeng, *Soft Matter*, 2020, **16**, 6697–6719.
581 C. R. Szczepanski, F. Guittard and T. Darmanin, *Adv. Colloid Interface Sci.*, 2017, **241**, 37–61.
582 T.-S. Wong, S. H. Kang, S. K. Tang, E. J. Smythe, B. D. Hatton, A. Grinthal and J. Aizenberg, *Nature*, 2011, **477**, 443–447.
583 C. Semprebon, G. McHale and H. Kusumaatmaja, *Soft Matter*, 2017, **13**, 101–110.
584 J. Cui, D. Daniel, A. Grinthal, K. Lin and J. Aizenberg, *Nat. Mater.*, 2015, **14**, 790–795.
585 R. Togasawa, M. Tenjimbayashi, T. Matsubayashi, T. Moriya, K. Manabe and S. Shiratori, *ACS Appl. Mater. Interfaces*, 2018, **10**, 4198–4205.
586 L. Li, B. Yan, J. Yang, L. Chen and H. Zeng, *Adv. Mater.*, 2015, **27**, 1294–1299.

587 W. Wang, L. Xiang, L. Gong, W. Hu, W. Huang, Y. Chen, A. B. Asha, S. Srinivas, L. Chen and R. Narain, *Chem. Mater.*, 2019, **31**, 2366–2376.
588 M. Li, W. Li, W. Cai, X. Zhang, Z. Wang, J. Street, W.-J. Ong, Z. Xia and Q. Xu, *Mater. Horiz.*, 2019, **6**, 703–710.
589 Y. Zhao, Y. Ohm, J. Liao, Y. Luo, H.-Y. Cheng, P. Won, P. Roberts, M. R. Carneiro, M. F. Islam and J. H. Ahn, *Nat. Electron.*, 2023, **6**, 206–215.
590 Y. Peng, S. Gu, Q. Wu, Z. Xie and J. Wu, *Acc. Mater. Res.*, 2023, **4**, 323–333.